Geophysical and Thermal Investigations of Ice-rich Permafrost at Parsons Lake, Northwest Territories

by

Michael C. Angelopoulos

Department of Geography
McGill University, Montreal, QC
August 2011

A thesis submitted to McGill University in partial fulfillment of the requirements of the degree of Masters of Science

Abstract

Geophysical and thermal investigations of ice-rich permafrost were performed in an area of planned hydrocarbon development at Parsons Lake, Northwest Territories. The site is owned by ConocoPhillips Canada (CPC) and ExxonMobil, and is intended to be a primary target for the Mackenzie Valley Gas Project. As a result, the Program of Energy and Research Development (PERD) funded this thesis to acquire more knowledge regarding the current and future state of permafrost at this site. Information on ground temperatures and material properties are available from boreholes extracted during the 2004 CPC drilling program.

In this study, the application of ground-penetrating radar (GPR) and capacitively-coupled resistivity (CCR) to map ground ice properties was tested. Since ground ice is an important factor affecting the level of disturbance initiated by thermokarst, improving the use of geophysical tools to map its nature and extent is important. By employing techniques to determine the maximum depth of investigation, optimal smoothing factors used during the inversion of raw resistivity data were computed. Once accomplished, it was found that the observed resistivity of massive ice ranged from 25 000 to 40 000 Ω. Conversely, values for massive ice were more widespread and overlapped with other materials like ice-rich peat when incorrect smoothing parameters were selected. The GPR cross-sections were applied to provide more detailed information on structure and contacts between massive ice and gravelly sand deposits. It was found that CCR generates similar outputs for these types of materials.

One-dimensional thermal models were constructed at previously undisturbed borehole locations. Thermal outputs were compared with the observed data, and it was found that the error during the thaw season at boreholes with near-surface mineral soils is less than 1 °C at any depth. When these models were used to project maximum active layer thickness changes for the period 2011-2070, subsidence is projected to begin as early as 2058. At disturbed locations, CCR surveys conducted in winter reveal two anomalies characterized by very low resistivities (< 600 Ω) beneath the gravel pads. One possible explanation is the development of taliks between 2004 and 2010, and thus, future fieldwork at this site is recommended. Overall, this investigation developed a model that can be used by industry to forecast near-surface thermal regime changes under varying scenarios of climate warming.

Résumé

Investigations géophysiques et thermiques du pergélisol riche en glace ont été effectués dans une zone de développement des hydrocarbures prévue à Parsons Lake, Territoires du Nord-Ouest. Le site est la propriété de ConocoPhillips Canada et ExxonMobil, et est destiné à être une cible principale pour le projet gazier Mackenzie Valley. En conséquence, le Programme de l'énergie et le développement de la recherche a financé cette thèse, qui améliore les connaissances locales sur l'état actuel et futur du pergélisol. Informations sur les températures du sol et des propriétés des matériaux sont disponibles à partir de forages.

Dans cette étude, l'application de géoradar et la résistivité électrique pour détecter les propriétés de glace de sol a été testée. Puisque la glace de sol est un facteur important affectant le niveau de perturbation du terrain, améliorer l'utilisation des outils géophysiques pour cartographier sa nature et son étendue est important. En utilisant des techniques pour déterminer la profondeur maximale de l'enquête, les facteurs de lissage optimal utilisé lors de la transformation des mesures brutes en pseudosections 2D ont été calculés. Une fois réalisé, il a été constaté que la résistivité de glace massive est entre 25 000 et 40 000 Ω. Inversement, les valeurs de glace étaient plus répandues et se chevauchent avec d'autres matériaux lorsque les paramètres de lissages incorrects ont été sélectionnés. Le géoradar a été appliqué pour fournir des données détaillées sur la structure de glace et les contacts entre la glace massive et dépôts de sable graveleux. On a constaté que la résistivité génère des valeurs similaires pour les matériaux.

Les modèles thermiques unidimensionnels ont été construits à des lieux de forage qui n'ont pas été affectés par les activités humaines. Les résultats ont été comparés avec les données observées, et il a été constaté que l'erreur pendant la saison du dégel aux forages décrits par les sols minéraux près de la surface est inférieure à 1 ° C à n'importe quelle profondeur. Lorsque ces modèles ont été utilisés pour des projets de couches actives à partir de 2011-2070, l'affaissement commence aussi tôt que 2058. Aux endroits perturbés, des enquêtes de résistivité en hiver révèlent deux anomalies caractérisées par des résistivités très faibles (< 600 Ω) sous la couche de gravier. Une explication possible est le développement de zones dégelées entre 2004-2010, et donc, plus de recherche à ce site est recommandée. Cette enquête a développé un modèle qui peut être utilisé par l'industrie pour prévoir des changements de régime thermique sous différents scénarios de réchauffement climatique.

Acknowledgements

With respect to ground thermal regimes and geophysics, I've been exposed to a long list of algorithms over the past two years. No algorithm, however, can transform Professor Wayne Pollard's enthusiasm for polar science into words. Wayne works tirelessly on his research, grant proposals, but above all, he ensures that his students have the resources necessary to succeed. As a result, I was very fortunate to have splendid equipment, generous funding, and a seemingly endless supply of interesting research questions to answer. Wayne cultivates his students by engaging them in conferences and workshops, as well as by assigning them a lot of responsibility. For example, allowing me to take on the challenge of being field manager this past summer was an awesome experience, and I feel that I've grown as a scientist. Wayne's the type of guy who will take risks and challenge you. I owe him a lot, and I look forward to my new challenge with the Canadian Space Agency this coming year. Thanks, Wayne!

My MSc could not have been possible without the support of Dr. Nicole Couture and Dr. Daniel Riseborough of the Geological Survey of Canada. Nicole is the guru of field logistics, and a lot of the decision-making skills I've learned were inspired by her strategies. Despite the exciting world of permafrost, I think working on the expense reports were the most fulfilling experiences we've shared together. Wouldn't you agree, Nicole? I love the fact that an error of two cents is enough to drive the university into a panic. Aside from her administrative assistance, Nicole provided considerable intellectual guidance, especially for conceptualizing an efficient study design. I am also indebted to Dr. Riseborough for his assistance with the thermal modelling component of my thesis. He is remarkably talented and hard-working, as demonstrated by his willingness to *modify the code* of the modelling program we were using. Had he not done so, it would have been impossible to apply such a robust permafrost dataset for the thermal models. Dan was a pleasure to work with, and I hope this isn't the last project we're involved in as a team.

During my MSc, I've participated in 4 excursions to the Western Canadian Arctic, and as a result, I know a few interesting people. First of all, I'd like to thank Dave Fox for making every day at the office unique. For example, pouring dish soap in my coffee was a very stimulating experience. Secondly, I am grateful to Heather Cray for all her help this past summer, especially for taking charge of inventory on our trip. Heather's thorough at *everything* she does, and is a wonderful example of a student dedicated to success. An honourable mention goes out to Leigh-Ann Williams-Jones, who bolted to the Aortic for the first time in 2011. In just her first excursion, she won the award for the heaviest samples. You better process every single one of them, Leigh-Ann!

I'd also like to high five everyone I've worked with from the Alfred Wegener Institute for Polar and Marine Research, especially Dr. Hugues Lantuit. His *laissez-faire* approach to life, as well as his sense of humour, makes him a great field companion. If you want a laugh or a detailed breakdown of retrogressive thaw slumps, Hugues is your man. Did I mention that he's also a networking genius? I'm pretty sure Hugues is the James Bond of permafrost science. He's got the wit, the connections, the suits, and the women! I mean, who else could lead five European girls into the Arctic? On that note, I've got to give hugs and kisses to Josefine Lenz and Béatrice Barbier of AWI. Jose is probably the only person in the world who repeatedly laughs at my jokes. It's quite possible that she doesn't fully understand them, but who cares? I still win.

Additional scientific input was provided by Dr. Richard Fortier from the University of Laval. The discussions we shared on data quality proved very useful for the interpretation of resistivity data. I look forward to further collaboration in the future! From a geophysical perspective, I owe a coffee or two to Tim Haltigin of the Canadian Space Agency. A former doctoral student of Wayne's, Tim introduced me to capacitively-coupled resistivity and has always been a source of inspirational phrases. *"Do it once, do it well"* is perhaps his best one. I am also grateful to Dr. Margaret Kalacska of McGill University's Geography Department for agreeing to be my committee member and providing feedback on my manuscripts.

For financial and logistics support, I'd like to express my gratitude to the Program of Energy and Research Development (PERD), NSERC, the Polar Continental Shelf Project (PCSP), ArcticNet, the Northern Scientific Training Program (NSTP), Herschel Island Parks, Parks Canada, Aurora Research Institute, as well as Jeff Hunston from the Yukon Government. In particular, I'd like to thank Bob Gowan from Indian and Northern Affairs Canada. He was instrumental in providing McGill University with the first PERD contract in 2002-2003, and as a consequence, I have been one of the beneficiaries of follow-up work. Thanks, Bob!

From a personal standpoint, I'd like to acknowledge my parents, who helped make my education possible. Without them, I wouldn't have had the latitude of exploring more than one undergraduate program, and thus, might never have discovered polar science. Thanks, Mom and

Dad! In addition, I'd like to thank Stephan Tanguay, my former long-time employer from Greenteam Landscaping. Stephan provided me with a flexible schedule, above average salary, and a great working environment for four years. Thanks to him, I was in a good financial position before starting my MSc. Perhaps even more credit should go to my loving girlfriend, Alex, for being so understanding the several weeks of my thesis writing. If it weren't for her brownies, I wouldn't have had the energy to work well into the night. You're the best!

Lastly, I'd like thank our wildlife monitor, Mike Harrison from the Inuvik Hunters and Trappers Committee (IHTC). Unfortunately, Mike suffered a snowmobiling accident this past winter and passed away. Mike will be remembered for his positive attitude, reliability, hard work, and incredible quotes.

"All I need are bullets and coffee" - Mike Harrison

Mike Harrison at Parsons Lake, NWT

Contribution of Authors

This thesis is written as two manuscripts to be submitted for publication in peer-reviewed journals, in accordance to the guidelines established by McGill University's Graduate and Postdoctoral Studies Office. For both papers, the contributions are as follows.

Manuscript I

Michael Angelopoulos

- Performed geophysical surveys
- Processed geophysical data
- Analysed borehole, thermal, and geophysical data
- Prepared manuscript

Wayne Pollard

- Arranged funding and logistics support
- Developed initial research proposal
- Guidance in the conceptualization of the project
- Intellectual input on ground ice and geophysics
- Editorial input into manuscript draft.

Nicole Couture

- Field and logistics support.
- Guidance in the conceptualization and planning of fieldwork.
- Provided valuable feedback throughout the research, and reviewed and commented on an earlier version of the manuscript.

Manuscript II

Michael Angelopoulos

- Performed geophysical surveys
- Processed geophysical data
- Parameterized subsurface thermal properties for the model
- Calculated preliminary ground surface temperatures at Parsons Lake
- Ran preliminary thermal models at McGill University using TempW software to test the quality of the borehole data
- Prepared manuscript

Wayne Pollard

- Arranged funding and logistics support
- Developed initial research proposal

- Guidance in the conceptualization of the project
- Intellectual input on permafrost stability and disturbance
- Editorial input into manuscript draft

Nicole Couture

- Field and logistics support
- Helped to plan and carry out field work.
- Assisted in the parameterization of subsurface thermal properties for the model.
- Editorial input into manuscript draft

Daniel Riseborough

- Calculated final ground surface temperatures at Parsons Lake
- Applied thermal properties of materials prepared by Michael Angelopoulos with ground surface temperatures to run robust models using TONE software at Geological Survey of Canada
- Intellectual input on ground thermal regimes and modelling

TABLE OF CONTENTS

List of Figures

List of Tables

Chapter 1 - Introduction

1.1 Project Overview

Mapping ground ice distribution is an enormous challenge facing land management and resource development related to oil and gas in the Arctic. The melting of ice destabilizes permafrost, leading to extensive thaw subsidence called thermokarst, which could threaten northern infrastructure (ACIA, 2004). Site-specific information about ground ice volumes and structure can be obtained either by invasive techniques like drilling and excavation or by non-invasive low impact geophysical methods. Since coring is one-dimensional and geophysical results are not unambiguous, combining the two approaches is ideal for an accurate assessment of subsurface conditions. Once the permafrost properties of an area have been established, they can be combined with local climate data to model the ground thermal regime. When coupled with regional climate warming investigations, these models can be used to predict the onset and extent of permafrost degradation (e.g. Smith and Riseborough, 2010, Zhang et al., 2008; Osterkamp and Lachenbruch, 1990). Results from geophysical surveys can be used to help parameterize multidimensional thermal models and/or assess the spatial applicability of one-dimensional outputs of permafrost thaw.

Since 2002-2003, investigators led by Dr. Wayne H. Pollard of McGill University's Department of Geography have been studying the nature, occurrence, and origin of massive ice in the Mackenzie Delta and Mackenzie Valley regions of the Western Canadian Arctic (e.g. de Pascale et al., 2008). Much of this research has been supported by the Program of Energy and Research Development (PERD), a federal initiative that funds projects designed to ensure a sustainable energy future for Canada. PERD is the primary funding source for this thesis, which focuses on an ice-rich area of planned hydrocarbon development at Parsons Lake, Northwest Territories (Figure 1.1). This study undertakes geophysical and thermal investigations of permafrost for a range of sites, including low-shrub dominated tundra, peat deposits, pingos, and anthropogenically disturbed areas characterized by the construction of gravel pads (Figure 1.2).

Parsons Lake is owned by ConocoPhillips Canada (CPC) and ExxonMobil, and contains 1.8 trillion cubic feet of natural gas 3 km below the ground. The site is an integral part of the proposed 1200 km Mackenzie Valley pipeline, a system that would transport natural gas from northern wells to an existing pipeline in northwestern Alberta. To enable decision-making about the possible uses and development of Parsons Lake, predictions about future permafrost conditions must be made. During the 2004 CPC winter drilling program, 26 cores ranging from 7.5 to 33.5 m depths were extracted from an area approximately 1 km^2. Ground temperature cables were also installed, and measurements were made in March, April, and September 2004. In a report prepared by the Kiggiak-EBA engineering consulting group, 25 of the 26 boreholes were said to contain massive ground ice. In the document, massive ground ice is defined as a layer at least 2 metres thick that has a volumetric ice content exceeding 60%. The depth to the top of massive ground ice ranged from just below the ground surface (in the case of ice-rich peat) to 16.5 m. The mean depth and standard deviation to the top of massive ground ice were 3.99 m and 3.33 m, respectively. Multiple forms of ground ice were identified, and they included pure homogeneous structures several metres thick, relatively thin layers buffered by icy sediments, as well as ice-rich peat deposits. Furthermore, the textures of materials overlying massive ground ice varied from silty clays to gravelly sands with volumetric moisture contents ranging from low (20-30%) to supersaturated conditions. As a consequence, numerous combinations of ground ice types and near-surface soils exist, each with a potentially different response to climate warming. Considering that the mean annual air temperature in the Parsons Lake area increased at an average rate of 0.72 °C per decade between 1961 and 2005 (Figure 1.3), there is an immediate need to better understand the present and future state of permafrost at this site.

1.2 Study Objectives and Organization of Thesis

Ground-penetrating radar (GPR) and capacitively-coupled resistivity (CCR) were employed for the detection and assessment of ground ice. GPR provides information about the subsurface stratigraphy, based on differences in the permittivity of different soil constituents. Pulses of electromagnetic radiation are transmitted into the ground and part of the signal is reflected back to the surface when an interface between materials is encountered. Conversely, CCR induces an electrical current into the ground and measures the resistivity of the material through which it passes. Although CCR and GPR have been combined in previous permafrost projects (de Pascale et al., 2008; Calvert et al., 2001), this is the first study that optimizes postdata processing in order to distinguish between assorted ground ice properties. Improving the use of geophysical tools to detect permafrost characteristics should enable land use planners to estimate the thermokarst risk of potential Parsons Lake development sites using a faster and cheaper approach. The thermal modelling phase of the project is designed to provide industry with a preliminary assessment of potential terrain stability problems. Since the models are one-dimensional, the geophysical surveys serve to extrapolate the ground thermal regime projections on a larger scale. Conversely, the thermal investigations are valuable for interpreting seasonal changes in resistivity at positions where the surveys and thermal models intersect. Specific objectives of the thesis are:

1. Map the extent of ground ice distribution
2. Combine borehole logs, GPR cross-sections, and optimally processed CCR data to quantify the geophysical outputs of varying ground ice properties
3. Determine the optimal balance between data consistency and smoothing for CCR pseudosections
4. Construct one-dimensional thermal models capable of predicting the observed temperature data from 2004
5. Application of the thermal models:
    a. Generate ground temperature profiles for fieldwork dates
    b. Project maximum active layer thickness changes from 2011-2070 using climate change scenarios available for the Mackenzie Valley
6. Assess the spatial applicability of the modelling results using geophysical data

Chapter 2 provides an overview of permafrost, ground ice, ground thermal regimes, and geophysical mapping. In order to avoid repetition, additional literature specific to the study aims (e.g. data processing) is covered in the manuscripts. The first three objectives are covered in Chapter 3, which focuses on the application of CCR and GPR to map ground ice properties. In this chapter, thermal modelling outputs are introduced in the discussion to assist with geophysical interpretation. The methodology used to construct the models is covered in Chapter 4, which addresses objectives 4-6 by discussing the present and future conditions of permafrost. Key findings and suggestions for future research are summarized in Chapter 5.

Figure 1.1. Parsons Lake is approximately 75 km north of Inuvik (NWT), which is situated in the Western Canadian Arctic. The study area is located on the northeastern side of the Parsons Lake, which corresponds to the proposed north pad development site. In the bottom right figure, the black square outlines the study area of the CPC winter drilling program, and as a consequence, the area of focus for this thesis. The gravel pad shown in the photograph was constructed in the mid 1970's. The air photo was provided by Dr. Nicole J. Couture of the GSC.

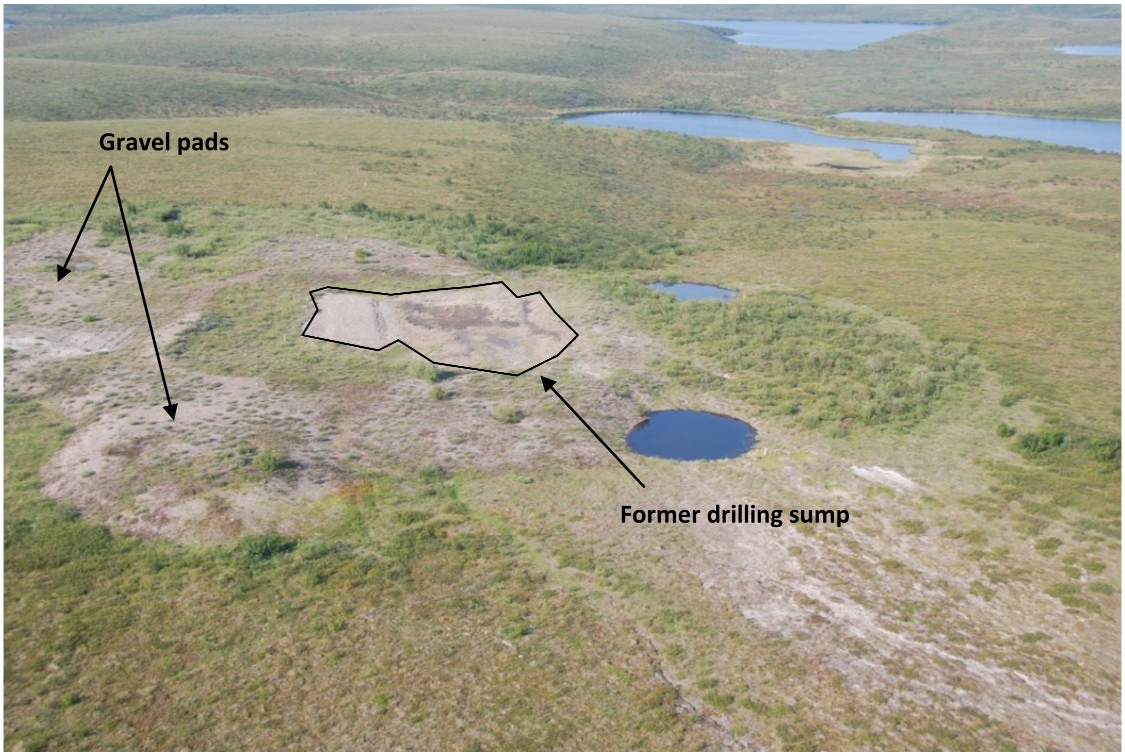

Figure 1.2. Gravel pads and former drilling sumps in the Parsons Lake area

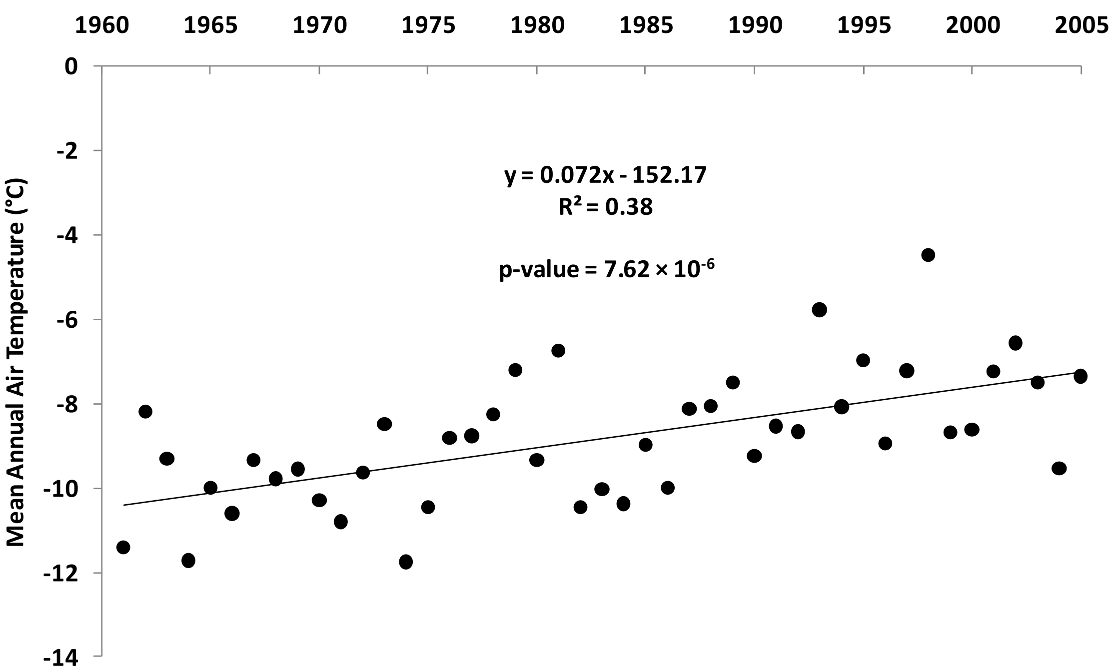

Figure 1.3. The mean annual air temperature at Inuvik increased at an average rate of 0.72 °C per decade between 1961 and 2005. The R^2 s 0.38 and it is significant for a 95% confidence level. Daily mean air temperature data for Inuvik was collected from Environment Canada to produce this graph. Values from 2006-2010 were not included, because they were not available for the same meteorological station with data from 1961-2005.

Chapter 2 - Literature Review

2.1 Permafrost and Ground Ice

Permafrost is defined as the thermal state of ground where temperatures remain at or below 0°C for at least two consecutive years (Muller, 1947). Its distribution is split into continuous and discontinuous zones, the latter characterized by widespread and sporadic areas. Excluding glaciers and ice sheets, perennially frozen ground underlies 23.9% of the northern hemisphere (T. Zhang et al., 2008), including approximately 50% of Canada (Figure 2.1). Since permafrost is a thermal condition, its formation, persistence, and disappearance are mainly dependent on how long-term climate patterns interact with the ground surface and subsurface thermal properties. Furthermore, its temperature, distribution, and thickness respond to natural environmental changes and anthropogenic disturbances that disrupt the thermal regime of the ground. Significant disturbances include changes in air temperature, precipitation, and the removal of insulating surface layers (e.g. vegetation, organic soil horizons). Transient projections of permafrost distribution in Canada (Y. Zhang et al., 2008) show that the area underlain by permafrost could decrease by 16.0-19.7% over the next century. The deepening of summer thaw could melt massive ground ice and cause ground subsidence.

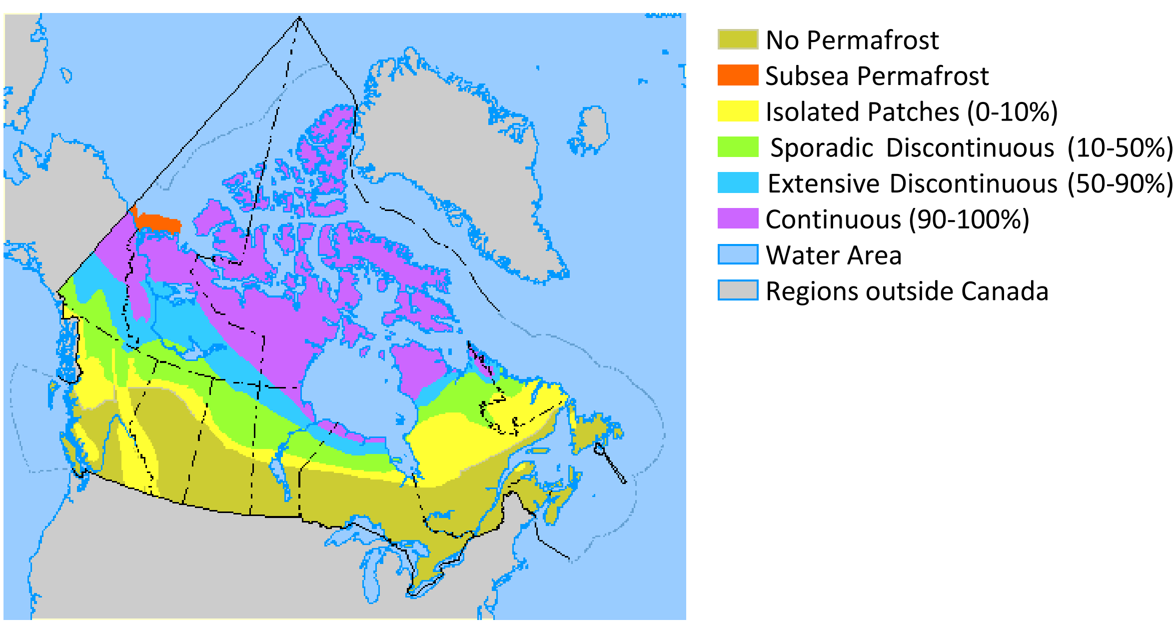

Figure 2.1. The distribution and zonation of permafrost in Canada (Natural Resources Canada, 1993). Note that changes in permafrost conditions between 1993 and 2011 are not shown in this figure.

In general, ground ice can be classified according to its association with enclosing sediments. *Epigenetic* ground ice forms within a pre-existing sediment sequence, whereas *syngenetic* ground ice develops concurrently with sediment deposition (Harry, 1988). More specifically, epigenetic ground ice materializes when water freezes in the sediments. Conversely, syngenetic ground ice forms during the burial of glacier ice, snowbanks, as well as lake and river ice. Specific ground ice types can be classified genetically according to the source of moisture prior to freezing and the mechanism that transfers the water to the freezing plane (Mackay, 1972). The most common forms of ground ice are a function of four of the processes illustrated in Figure 2.2. To begin with, gravity can cause surface water originating from the atmosphere to trickle down thermal contraction cracks and generate *ice veins*. If this process is repeated at the same location for multiple years, vertically foliated wedge-shaped bodies of ice termed *ice wedges* may form (Figure 2.3b). Secondly, subsurface moisture can freeze in situ to generate pore ice. Thirdly, if pressure potentials exist, underground moisture injected into sediments can form *intrusive ice*. This process can produce a pingo, which is defined as a perennial frost mound consisting of a core of massive ice or icy sediments covered with soil and vegetation. There are both open-system (Muller, 1959; Hugues, 1969) and closed-system pingos (Mackay, 1973; Mackay, 1979; Mackay, 1985). Closed system pingos form underneath former water bodies. Porewater contained in the underlying talik (unfrozen zone enclosed by permafrost) migrates towards aggrading permafrost to create a dome-like or a conical structure (Figure 2.3c). In open-systems, groundwater moves downslope through taliks to the site of pingo development. Fourthly, if both pressure and thermal potentials exist, moisture is capable of migrating upwards towards the freezing plane to construct a segregated ice pattern comprised of *ice lenses* and *ice layers*. These structures develop when cryotic suction draws subsurface water to the zero degree isotherm. The thickness of an ice lens (Figure 2.3d-e) depends on the balance between the moisture migration rate and latent heat removal from the freezing front (Smith, 1985). Since this is the most widespread ground ice type observed at Parsons Lake, more details on intrasedimental ice formation are given in section 2.2.

The volume of ground ice in permafrost is a geological expression of one or more of the main ice forming processes. It varies from a few percent (Bockheim and Tarnocai, 1998) to nearly 100% in the case of *massive ground ice* (Figure 2.3a), the latter of which is defined as having a moisture content exceeding 250% by dry weight (mass of moisture divided by the mass of dry soil). By and large, massive ground ice units can be up to 10-30 m thick and cover 1 km^2 (e.g. Mackay and Black, 1973). Ground ice contents tend to be higher in the near-surface (Pollard and French, 1980), and occasionally, they can volumetrically comprise up to 70% of the upper portion of permafrost (French et al., 1986; Couture and Pollard, 1998). The volume of ice that surpasses the total pore volume the host sediments would have under unfrozen conditions is termed *excess ice*. Materials containing excess ice are considered *thaw sensitive* (van Everdingen, 1979), because the melting of ground ice would result in runoff of supernatant water and thermokarst subsidence of the ground surface. On the contrary, *thaw stable* materials do not contain excess ice and are not susceptible to thermokarst. Thermokarst is generally initiated in one of two ways. Either, the active layer increases in thickness or part of it is removed. Either way, the top of the underlying permafrost becomes subject to melting. A number of the natural and anthropogenic surface changes that can lead to the development of thermokarst are illustrated in Figure 2.4.

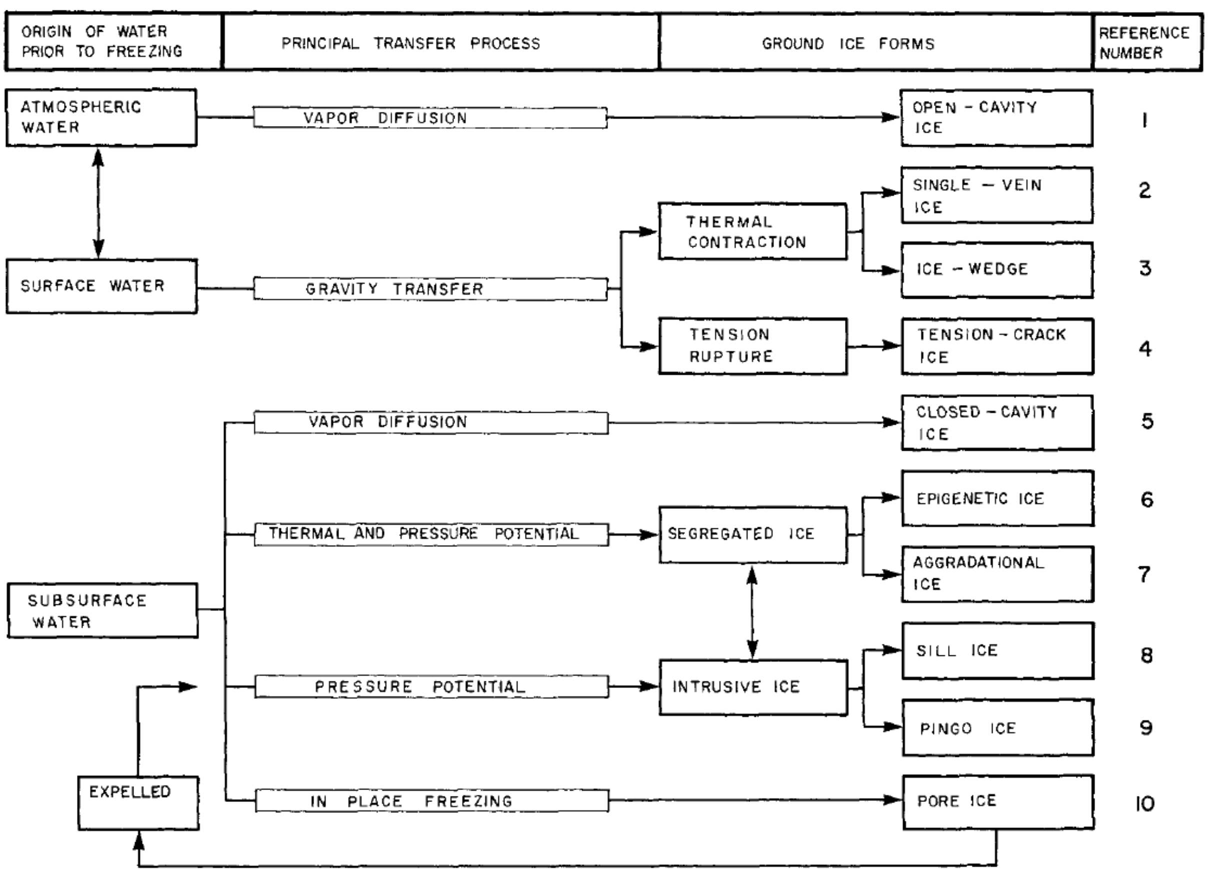

Figure 2.2. A genetic classification of ground ice (Mackay, 1972)

Figure 2.3. Various forms of ground ice, including a massive ice body at an exposed retrogressive thaw slump on Herschel Island, YT (a), an ice wedge on Herschel Island, YT (b), a pingo approximately 40 km NW of Parsons Lake (c), and Parsons Lake boreholes showing thin ice lenses (d) and thick massive ice lenses (e). The sources of the photos are Dr. Nicole J. Couture of the Geological Survey of Canada (a), Dr. Wayne H. Pollard of McGill University's Geography Department (b), Michael C. Angelopoulos (c), and the Kiggiak-EBA geotechnical assessment report (d & e).

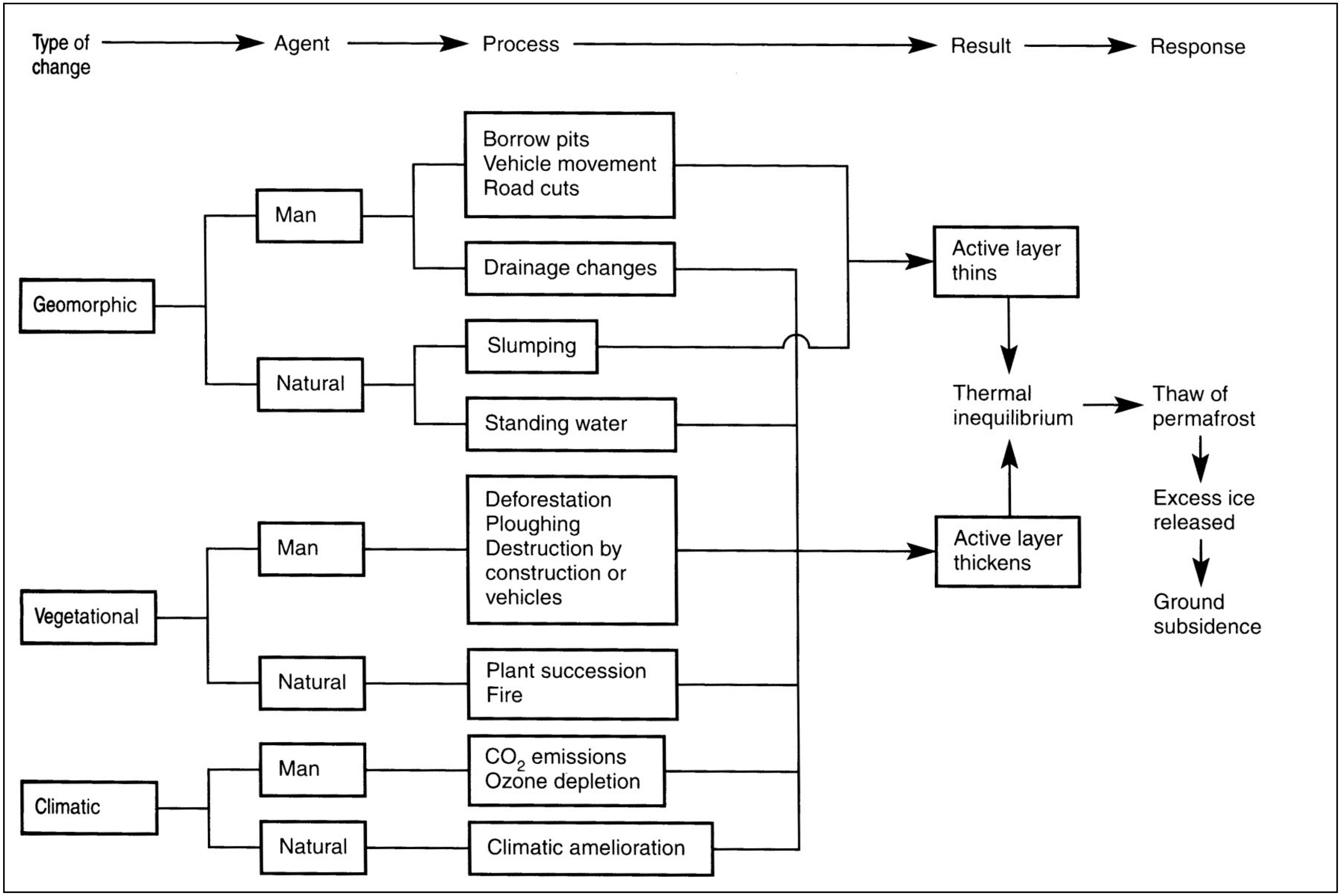

Figure 2.4. Diagram illustrating how geomorphic, biogeographical, and climatic changes may lead to permafrost degradation (French, 1996).

2.2 Intrasedimental Ice Formation

2.2.1 Theoretical Modelling of Massive Icy Beds

Theoretical modelling of massive icy beds presented in Konrad (1990) describes the formation of an idealized ice lens over time. To initiate the freezing process in the model, the temperature is dropped to a value, T_c, below 0 °C at time zero. The rate at which the freezing front descends into the ground depends on T_c and the geothermal gradient, which is a function of heat generated deep within the Earth and the thermal conductive properties of the subsurface. Assuming steady state conditions, the final position of the zero-degree isotherm (ZDI) can be determined by equation 2.1, where T_z is the temperature at a particular depth (0 °C in this case), T_s is the surface temperature, Q_G is the heat flow by conduction, and k is the thermal conductivity (Williams and Smith, 1989).

$$ZDI = \frac{T_z - T_s}{Q_G/k} \qquad [2.1]$$

Even if one assumes a homogeneous Earth, the displacement of the freezing front is not constant. This is because the distance between T_c and the ZDI increases with time, so the temperature gradient weakens as the freezing front descends. As the freezing front penetrates the ground, porewater may freeze *in situ* and/or segregation ice lenses may form through soil moisture migration (Smith, 1985). The rate of soil moisture migration through cryosuction, is proportional to the temperature gradient in unfrozen soil as shown in equation 2.2

$$\Delta T_{unfrozen\ soil} = \frac{0\ °C - T_{water\ level}}{z_{ZDI} - z_{water\ level}} \qquad [2.2]$$

Assuming the overburden pressure is negligible and the groundwater is pure, the latter freezes when it reaches the ZDI, and as a consequence, latent heat is released. The continued growth of a specific lens depends upon the balance between the rate at which latent heat can be removed (i.e. temperature and thermal conductivity above the freezing front) and the rate at which water is supplied to the system (Smith, 1985).

For this model, the overburden pressure is not constant, but is coupled to increasing mass (i.e. pressure) above the freezing front during the development of an ice lens. As a result, the freezing point is reduced with increasing overburden pressure. Konrad shows that the growth of an ice lens slows with time as the temperature gradient lessens. The downside of Konrad's model, however, is that it is designed such that the soil moisture migration rate is always in dynamic equilibrium with the rate at which latent heat is removed during ice formation. As a consequence, sediment and ice units (ice segregation pattern) cannot be produced. As the rate of freezing weakens, thicker ice lenses can develop if all other factors remain the same (Williams and Smith, 1989). Since fine-grained materials like silts and clays are characterized by low hydraulic conductivities and high matric potentials in relation to coarse-grained sediments like sands and gravels, they are more predisposed to intrasedimental ice formation.

2.2.2 Thermally-Induced Regelation

Thermally-induced regelation (Perfect and Groenevelt, 1990) is a useful complement to Konrad's work. In Perfect's model, temperature gradients drive particle migration (Figure 2.5). Unlike moisture flows, particles move from a cold to warm direction. In the thermo-active zone (i.e. area that experiences annual temperature variations), warm summer temperatures induce the transport of soil particles towards the base of the active layer. In winter, the thermal gradients are reversed and movement occurs towards the depth of zero annual amplitude (refer to section 2.3). Since the temperature at which upward migration takes place is warmer than the temperature of downward migration on average, the particles in the thermo-active zone should experience a net upward displacement. Below the depth of zero annual amplitude, particles may migrate downwards due to the geothermal gradient. The results of Perfect's model suggest that the net upward flux of particles in the thermo-active zone is slightly larger than the downward flux of particles in the thermo-inactive zone. The directional differences in particle fluxes between the thermo-active and thermo-inactive zones is important, because it supports observations that ice-rich conditions often occur near the permafrost table (e.g. Mackay and Dallimore, 1992; Pollard and French, 1980). As described in the previous section, ice lenses should theoretically get thicker with depth due to a decelerating frost front. Once an ice-segregation pattern is developed, thermally-induced regelation could purify the ice in the thermo-active zone. Understanding that the processes involved with intrasedimental ice formation can fluctuate over space and time is important, because it can help explain anomalies in geophysical datasets.

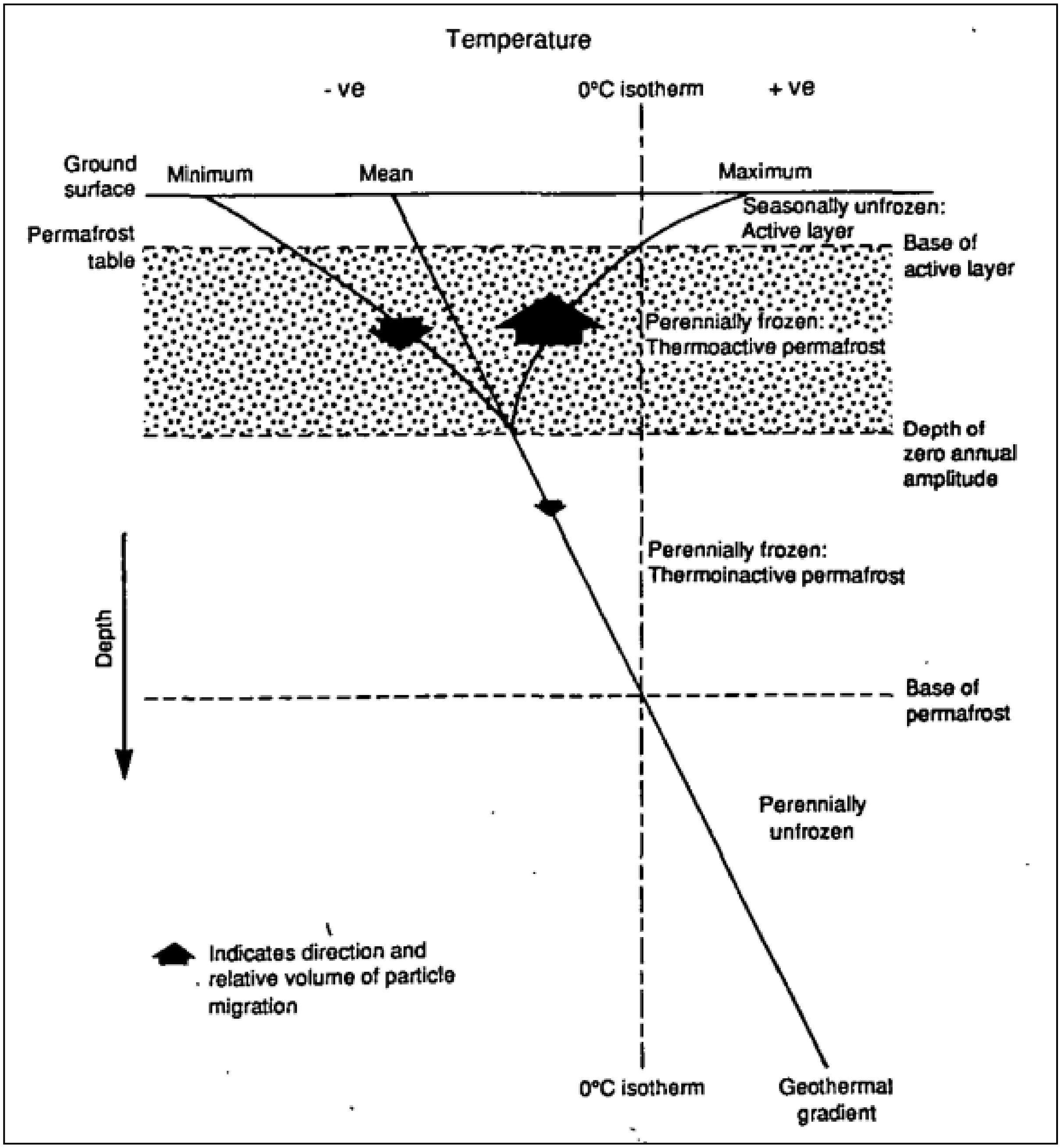

Figure 2.5. Conceptual diagram illustrating thermally-induced regelation (Perfect and Groenevlet, 1990)

2.3 Ground Thermal Regimes

Ground thermal regimes are usually explained using heat conduction theory. If the Earth is reduced to a homogeneous medium in which energy propagates in the vertical direction only, then the amount of heat that flows by conduction (Q_G) is computed by equation 2.3, where k is the thermal conductivity and dT/dz is the temperature gradient with depth (Williams and Smith, 1989).

$$Q_G = -k\frac{dT}{dz} \qquad [2.3]$$

The ground's thermal conditions reflect the interaction between heat flowing from the Earth's interior and the surface energy regime. As demonstrated by Williams and Smith (1989), the geothermal gradient is a function of the *thermal conductivity*, a measure of the quantity of heat that flows through the unit area of a substance per unit time. If a high thermal conductivity is coupled with a low geothermal heat flux and a cold mean annual surface temperature, thick permafrost can develop.

Ground surface temperatures (GST) are highly variable over space and time, and are a function of air temperatures and the buffering capacity of snow cover, vegetation, as well as organic layers. Snow cover acts a barrier to heat loss from the ground to the atmosphere in winter, and as demonstrated by Nicholson and Granberg (1973), can be the main variable responsible for spatial changes in mean annual ground surface temperatures (MAGST). The magnitude of snow's insulative effect is a function of its depth and thermal conductivity, the latter of which is determined by its density. Goodrich (1982b) shows that the effect of snow density on the thermal conductivity is exponential, and Smith (1975) demonstrates that differences is snow depth between 0-50 cm induce greater variations in the MAGST compared to snow depths ranging from 50-110 cm. Since snow tends to accumulate in forested areas, similar warming of the MAGST occurs. The consequences of evapotranspiration in summer, however, result in relatively cool GSTs during this time of year. On the other hand, if vegetation is scarce, not present, or removed, the *active layer*, the zone which seasonally thaws and freezes every year, increases in thickness. As noted by Mackay (1977), the thaw depth increased for several years following a forest fire in Inuvik, NWT. Assuming snow cover is uniform, peat soils tend to result in lower MAGSTs compared to adjacent areas without peat (e.g. Brown, 1973) due to seasonal variations in thermal properties. During the summer, peat soils are dry, and as a result, their thermal conductivities are very low. Once the effect of evaporation is reduced in the fall, moisture contents increase, and because of their high porosities, large volumes of ice can exist in the near-surface by the onset of winter. As liquid water freezes to ice, its conductivity increases by a factor of 4 (Williams and Smith, 1989), and thus, peat soils cool rapidly.

Once the geothermal gradient and the annual GST patterns are known, the ground thermal regime can be predicted using material properties. Assuming a homogeneous Earth, the rate at which temperature fluctuations on the surface influence a particular depth is a function of the *thermal diffusivity*, a ratio between the thermal conductivity and the *volumetric heat capacity (C)*. The maximum depth affected by seasonal temperature changes at the surface is termed the *depth of zero annual amplitude*. The volumetric heat capacity is defined as the amount of energy required to raise 1 m^3 of a substance by 1 °C without producing a phase change. For composite materials, the thermal conductivity of the soil matrix is computed using a geometric mean (Johansen, 1975), whereas a linearly weighted average is suitable for the volumetric heat capacity. For ice-rich permafrost, the thermal diffusivity is heavily affected by latent heat fluxes. Since unfrozen water can exist at temperatures well below 0 °C, the actual change in heat storage from an initial temperature to a final temperature is given by equation 2.4 (Lunardini, 1981), where the first integral refers to the sensible heat capacity of the soil and the second integral refers to the amount of latent heat absorbed or released.

$$\Delta H = \int_{T_i}^{T_f} C dT + \int_{T_i}^{T_f} \rho_w L_f d(UWC) \tag{2.4}$$

The range of temperatures over which latent heat plays a role is greater for fine-grained soils. For a synthesis of UWC versus temperature functions, the reader is referred to Andersland and Ladanyi (2004). When latent heat is accounted for, a material is described as having an *apparent heat capacity*, and thus, an *apparent thermal diffusivity*. These processes are accounted for in many of the thermal models reviewed by Riseborough et al. (2008), and only the frozen and unfrozen volumetric heat capacities must be specified. A diagram illustrating the principle components of the ground thermal regime is shown in Figure 2.6, and a schematic of thermal inputs required for typical modelling applications is shown in Figure 2.7. For a comprehensive summary on the thermal properties of soils, the reader is referred to Farouki (1981).

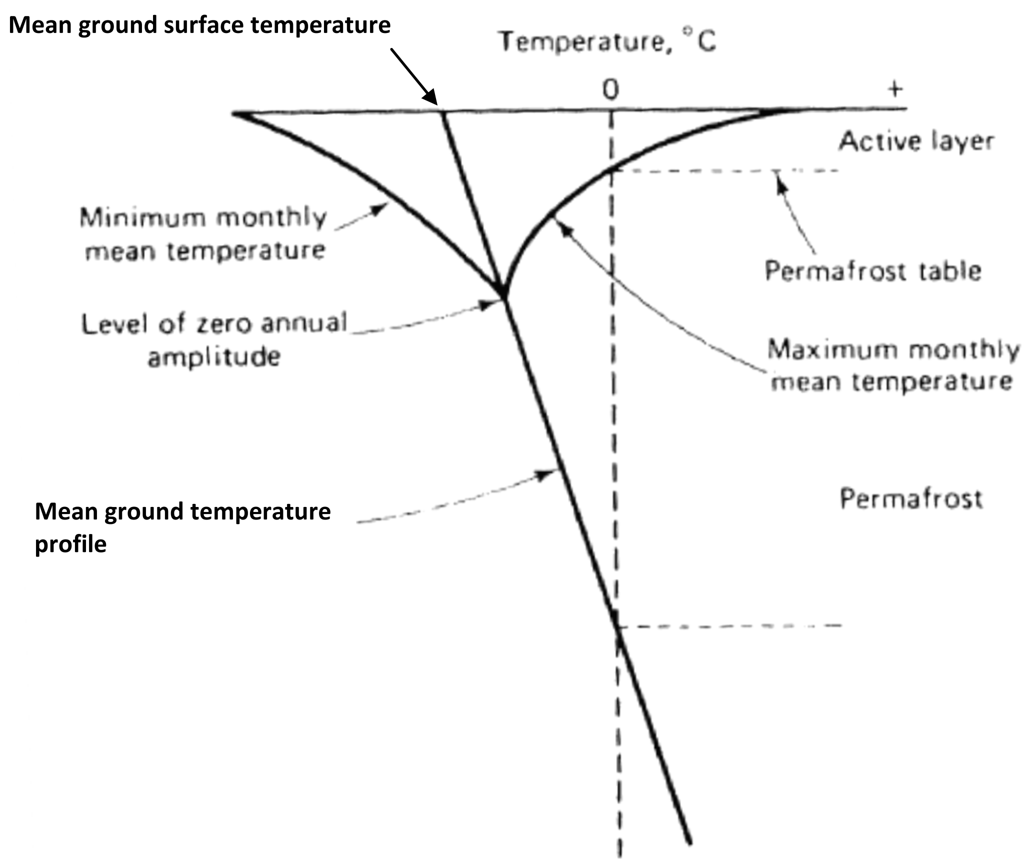

Figure 2.6. An example of a ground temperature profile (Andersland and Anderson, 1978)

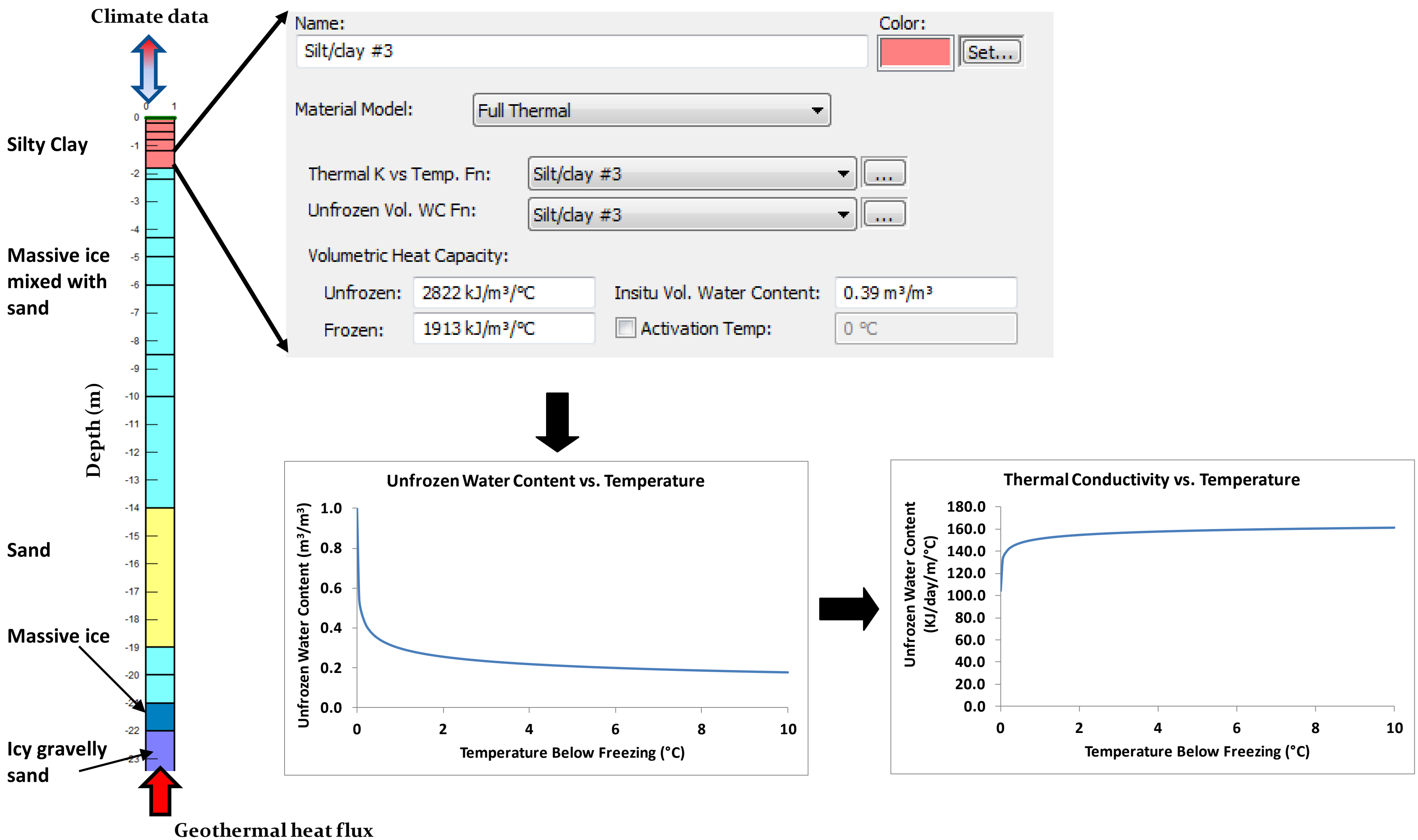

Figure 2.7. This diagram shows a typical example of how a thermal model is parameterized (borehole P8, Parsons Lake). The nature of the material and its moisture content form the basis of an unfrozen water content versus temperature function. Subsequently, the unfrozen water content function is used to compute a thermal conductivity versus temperature function. Since the software (e.g. TONE, TEMPW) used for this diagram accounts for latent heat, only the frozen and unfrozen volumetric heat capacities must be specified. The upper and lower boundary conditions pertain to climate data and geothermal heat fluxes, respectively.

2.4 Geophysical Mapping of Permafrost

Subsurface information on ground ice and sediment patterns forms an important starting point for most construction activities. The labour and cost associated with excavation is a major drawback compared to geophysical surveys, and although exposed stratigraphic sections provide valuable 2D data, their presence are not guaranteed. Furthermore, in cases where they do exist, they might not meet the desired depth or lateral extent of investigation. Lightweight geophysical equipment can function with minimal effort to quickly produce 2D or 3D subsurface images. Despite the operational advantages of geophysics, the interpretation of geophysical results is not always explicit. Therefore, it is necessary to combine both traditional and surface-based geophysical methods to generate an accurate assessment of subsurface conditions.

2.4.1 Electrical Resistivity Tomography

Direct current resistivity (DCR) and capacitively-coupled resistivity (CCR) are used to identify subsurface composition by calculating the resistivity of the materials through which an induced electrical signal passes. Unlike DCR, CCR applications (e.g. Timofeev et al., 1994; Calvert et al., 2001; Hauck and Kneisel, 2006; de Pascale et al., 2008), require no galvanic contact with the ground. This technique overcomes problems associated with impenetrable surfaces for electrodes, which are reported in Muller (1947), as well as Scott and Mackay (1976).

One or multiple receivers are used to detect an electric field and measure the potential difference (voltage) of the materials through which a current has passed. The differential vector form of Ohm's Law, which relates current density (J), the strength of the electrical field (E), and apparent resistivity (R), is shown in equation 2.5.

$$R = \frac{E}{J} \qquad [2.5]$$

Equation 2.5 calculates the apparent resistivity of the total volume of underlying materials affected by current flow. When a current is transmitted (Figure 2.8a), it propagates radially in all directions except above the surface due to the extremely resistive properties of air. In view of that, the apparent resistivity is characteristic of an average resistivity for a subsurface volume. In vertical electrical sounding, the array is monotonically expanded about a central point to generate apparent resistivities for deeper underground sections. Although this method is useful for identifying vertical resistivity changes with depth, it assumes a simple, horizontally stratified subsurface. Lateral electrical profiling like CCR (Figure 2.8b), however, moves the entire array across the surface while maintaining constant electrode geometry. In order to incorporate vertical changes in resistivity, the transect is surveyed multiple times with different electrode spacings. When vertical and lateral changes in resistivity are combined, a 2D image of apparent resistivity termed a *pseudosection* is generated. Assuming no signal attenuation, the depth of a pseudosection is equal to roughly 1/3 the dipole spacing (Hauck and Kneisel, 2006). In an attempt to convert apparent resistivities into true resistivities, an inversion model is required. Inversion programs model apparent resistivities for each cell of the pseudosection and compare the outputs with the observed values. If the misfit is greater than a user-defined tolerance, the model parameters are adjusted and apparent resistivities are re-calculated (Loke and Barker, 1996).

Electrical resistivity is controlled by water and ice volumes, geochemistry, temperature, grain size, as well as the porosity and degree of saturation of soil (McNeill, 1980). The effects of these variables are not always independent, because they each contribute to the amount of unfrozen water present. Unfrozen water content is a key variable responsible for resistivity changes (Hauck, 2002), and as demonstrated by Hauck et al. (2003), a large increase in resistivity occurs at the freezing point when most of the available moisture turns to ice. In interstitial ice, the unfrozen water films are continuous in pores and interconnected passages, and as a consequence, conduits exist for current flow (Fortier et al., 1994). In stratified cryostructure, however, the unfrozen water films are discontinuous, and as a consequence, the current flow through ice is impeded, which increases resistivity values. The effects of ice structure are linked to the spacing between ice lenses, the thickness of the ice lenses, and temperature. The effects of unfrozen water on resistivity are clearly demonstrated in Figure 2.9.

As ice content increases, there should be an exponential increase in resistivity independent of soil type and temperature (Hoekstra et al., 1975). Direct current resistivity has proven successful at mapping ice cores in rock glaciers (Vonder Mühll et al., 2002; Hauck et al., 2004; Kneisel, 2004; Hauck and Kneisel, 2006), pingos (Yoshikawa et al., 2006), and moraines (Hauck et al., 2003). The range of resistivities expected in permafrost environments compared to common geological materials is summarized in Sharma (1997).

2.4.2 Ground-Penetrating Radar

Ground penetrating radar (GPR) relies on differences in dielectric permittivity between materials to determine underlying stratigraphy. The transmitter induces an electromagnetic wave into the subsurface, and when the wave encounters a boundary between two materials of contrasting permittivity, a reflection is generated and captured by the receiver (Figure 2.10a). Figure 2.10b illustrates the GPR system used for this project and Figure 2.11 provides a photograph of an interface with a strong dielectric contrast. Given that wave propagation through a medium is a direct function of the medium's permittivity value (ε), it is possible to use the signal's return time (t) to translate the GPR cross-section's time axis into depth beneath the surface (d) through equation 2.6, where c is the speed of light in a vacuum.

$$d = \frac{t \cdot c}{2\sqrt{\varepsilon}} \qquad [2.6]$$

Equation 2.6 assumes a uniform substrate and coincident locations for the transmitter and the receiver. The application of this equation assumes a prior knowledge of the medium's permittivity. Should such information not be available, four alternative techniques are outlined in Table 2.1. In addition, the usefulness of each technique for this thesis is explained.

In order to acquire local environmental context, GPR surveys should be integrated with a device capable of providing information on topography. If a global positioning system (GPS) is not available, Furgale et al. (2010) illustrate the use of a stereocamera to perform visual odometry and enhance GPR data. VO is a technique that uses two images acquired by a stereocamera to estimate the system's relative motion. Once a target is identified on both images and interpreted to be identical, one may use the known camera separation to triangulate for the range between the cameras and the target. Furthermore, stereocameras can provide colour/texture information about the terrain. By correcting for topography, a more realistic interpretation of GPR cross-sections is possible. For example, accurate eccentricities for hyperbolic events and linkages between discrete subsurface targets and the surface can be drawn.

1. As documented in Table 2.1, depth estimates for discrete targets and stratigraphic units can be improved with diffraction pattern analyses. Since hyperbolic shapes are distorted

when topography is not accounted for, failing to account for relief changes could lead to inaccurate velocity estimates.

2. In Figure 2.12, a diffraction pattern is caused by a surface depression. In this example, surface depressions are associated with elongated troughs characteristic of ice-wedge polygonal networks. Hence, the hyperbola just below the permafrost table is interpreted as an ice wedge. In the absence of topographic corrections, the link between the surface and the subsurface cannot be made. Hence, the cross-section is less interpretable.

The maximum depth of signal penetration and resolution are partially dependent on the frequency of the wave induced into the ground. Typically, signal attenuation is directly proportional to signal frequency, which will thus be anti-proportional to the depth of propagation. The vertical resolution is approximately one-quarter of the wavelength, and thus, a higher frequency GPR signal will provide greater subsurface detail. The extent of signal attenuation is caused by spreading, scattering, and absorption by conductive materials. Spreading losses result in a 1/r (r = distance from point source of EM radiation) dependence for GPR signal strength, but absorption by conductive materials is the main factor resulting in exponential signal attenuation with depth. Hence, signal penetration is limited by increasing levels of salinity (e.g. al Hagrey and Muller, 2000), unfrozen soil moisture, and decreasing grain size (e.g. Moorman et al., 2003).

Surveys provide considerable information on near-surface structure; however, in the absence of borehole or natural exposure data to constrain materials and velocities, GPR is useful for identifying areas where future drilling activities might of interest. GPR is capable of mapping ground ice due to the vast differences in dielectric properties displayed by ice, water, and certain sediments. Dielectric constants for common materials are shown in Table 2.2, and the reader is referred to Keller (1987), Olhoeft (1981), and Parkhomenko (1967) for more information. The strength of a reflection (reflection coefficient, R) is determined by the dielectric constants (ε_1 and ε_2) at the interface between the two materials as shown in equation 2.7.

$$R = \frac{\sqrt{\varepsilon_1} - \sqrt{\varepsilon_2}}{\sqrt{\varepsilon_1} + \sqrt{\varepsilon_2}} \qquad [2.7]$$

In ice-rich sediments, it is possible to distinguish frozen from unfrozen sediments due to the increase in dielectric permittivity as water freezes to form ice (Scott et al., 1990; Arcone et al., 1998; Arcone and Delaney, 2003). Individual ice lenses within permafrost, however, are occasionally thinner than the system's resolution. For this situation, the GPR signal tends to show increasing scatter with increasing ice lens volumes (e.g. Hinkel et al., 2001). Conversely, massive ice lends itself well to mapping by GPR. Since nearly pure ice has a low dielectric permittivity (ε ~ 3.2), both the top and bottom of massive ice should be detectable, because of strong dielectric contrasts at the ice-sediment interfaces, while the body of the ice, if homogeneous, will not show many reflection events (e.g. Moorman et al., 2003; Stevens et al., 2008). Studies delineating high and low ice content in soils or granular areas have been demonstrated by Arcone and Delaney (1998), Horvath (2003), and Yu et al. (2003).

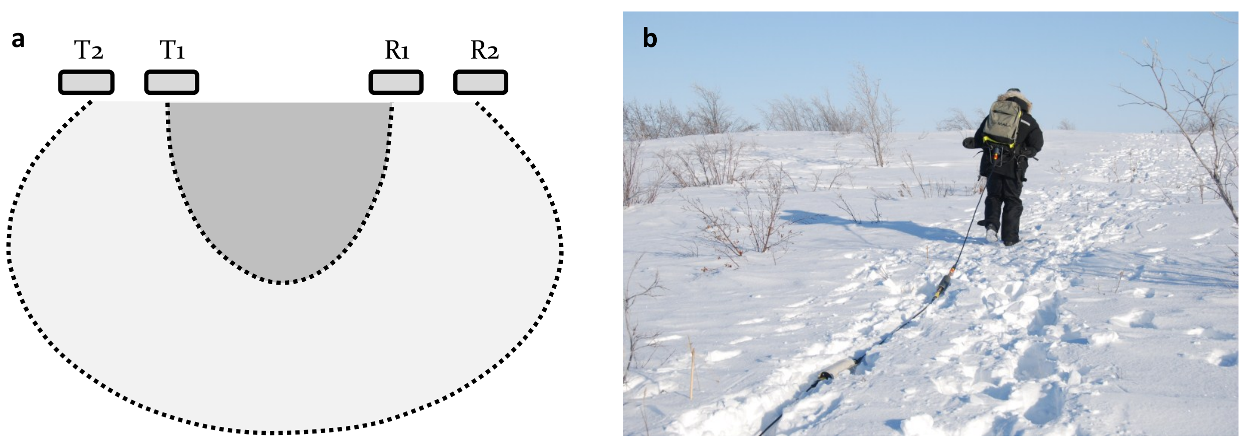

Figure 2.8. The CCR surveying technique is displayed in (a). Here, T and R symbolize the transmitter and receiver, respectively. The numerical subscripts refer to two different T-R spacings. For a shorter separation, the instrument is sensitive to a smaller volume of subsurface materials. In (b), the TR1 Geometrics Ohmmapper CCR system is illustrated.

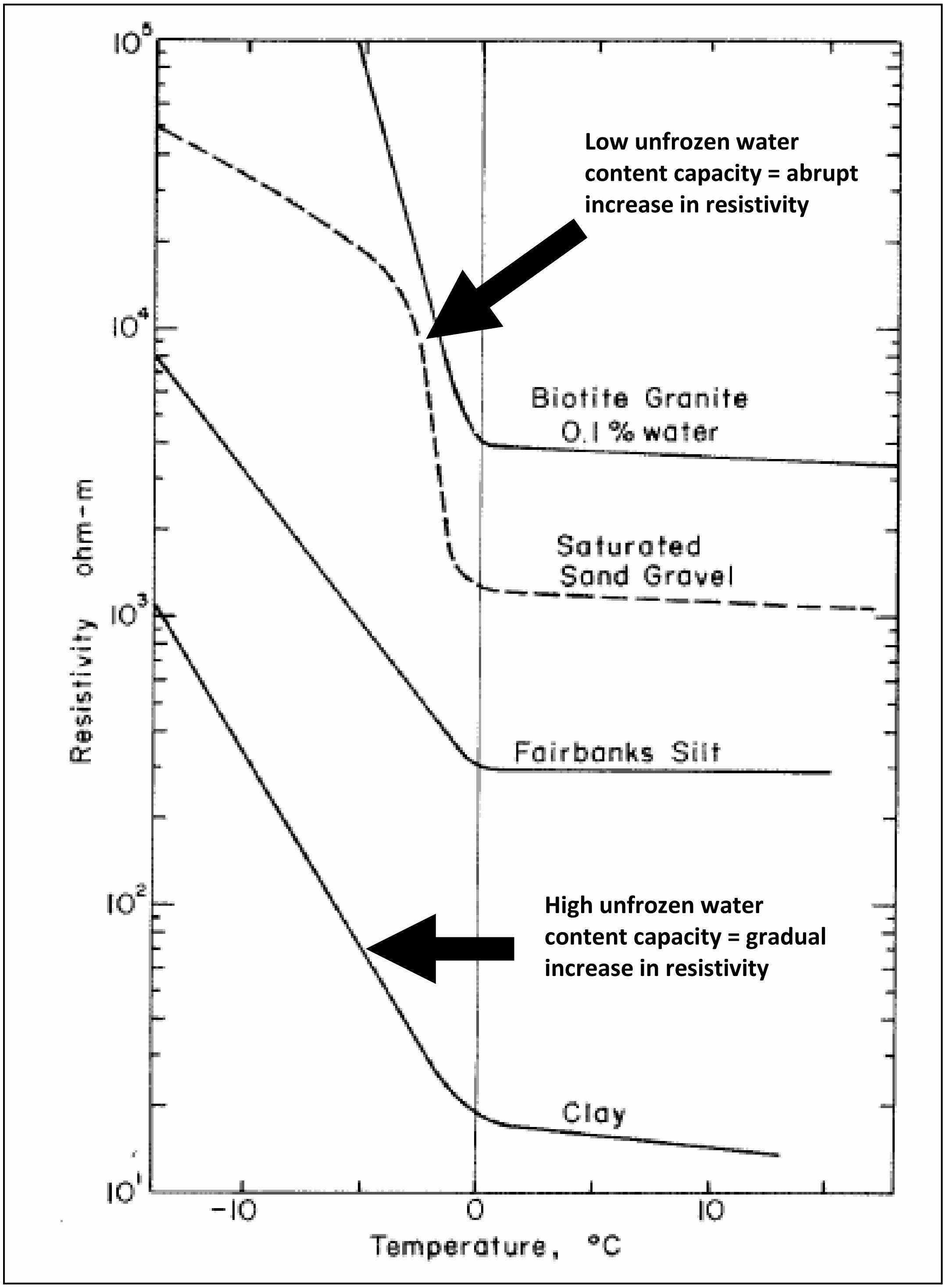

Figure 2.9. The graph illustrates the dependence of electrical resistivity on temperature (modified from Hoekstra and McNeill, 1973).

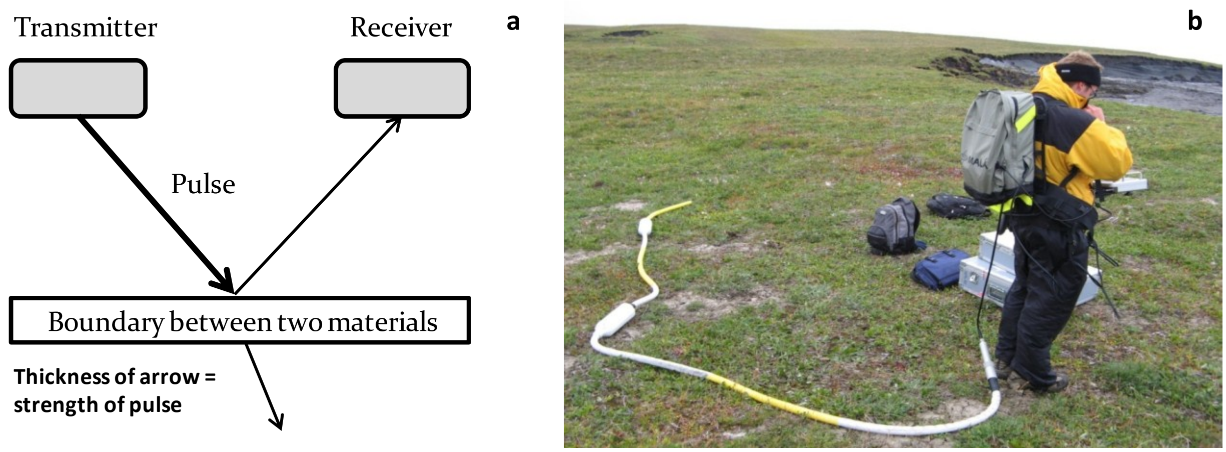

Figure 2.10. A simplified image of GPR operation is shown (a), whereas the 50 MHz MALA Geoscience RAMAC rough terrain concept antenna used in this study is illustrated in (b)

Table 2.1. Methods to Calculate Dielectric Permittivity or Velocity in the Absence of Real Data

Technique	Applicable For This Project?	Description
Common Midpoint (CMP) Surveying	No: Flexible transmitter-receiver separations are not possible with our instrument	A reflector is identified on a GPR cross-section for a transmitter-receiver spacing defined by s. Subsequently, s is increased monotonically and changes in the pulse's two-way travel time to the reflector are observed. By plotting two-way travel time as a function of transmitter-receiver separation, velocity can be estimated by calculating the square root of the slope's reciprocal. Refer to Annan (2005).
Trenching	Yes: Cores exist for geophysical interpretation	Bore or trench to a known reflector and use the measured depth to calibrate for ε (e.g. Hinkel et al., 2001)
Diffraction Pattern Analysis	Profile-dependent: Hyperbolic events are not guaranteed to appear on GPR cross-sections.	GPR systems transmit energy in all directions. Scattering from discrete targets results in hyperbolic reflection events in GPR cross-sections. Hyperbolic fitting, available in standard interpretation software can provide depth and average velocity to target. Refer to Annan (2005).
Surface Reflection	No: Operational sophistication is not cost-effective	The GPR is held at a fixed height above the surface. The amplitude of the reflected event from the surface is related to the permittivity of the near surface. In some cases reflections from underlying interfaces may also provide the permittivity of lower layers.

Table 2.2. Dielectric constants and velocities for common materials (Annan, 2005)

Material	K	velocity (m/µs)
Air	1	300
Distilled water	80	33
Fresh Water	80	33
Sea Water	80	10
Dry Sand	3-5	150
Saturated Sand	20-30	60
Limestone	4-8	120
Shales	5-15	90
Silts	5-30	70
Clays	5-40	80
Granite	4-6	130
Dry Salt	5-6	130
Ice	3-4	160

Figure 2.11. High dielectric contrast between ice-poor sediment and massive ice on Herschel Island, YT. The photo was taken by Michael C. Angelopoulos.

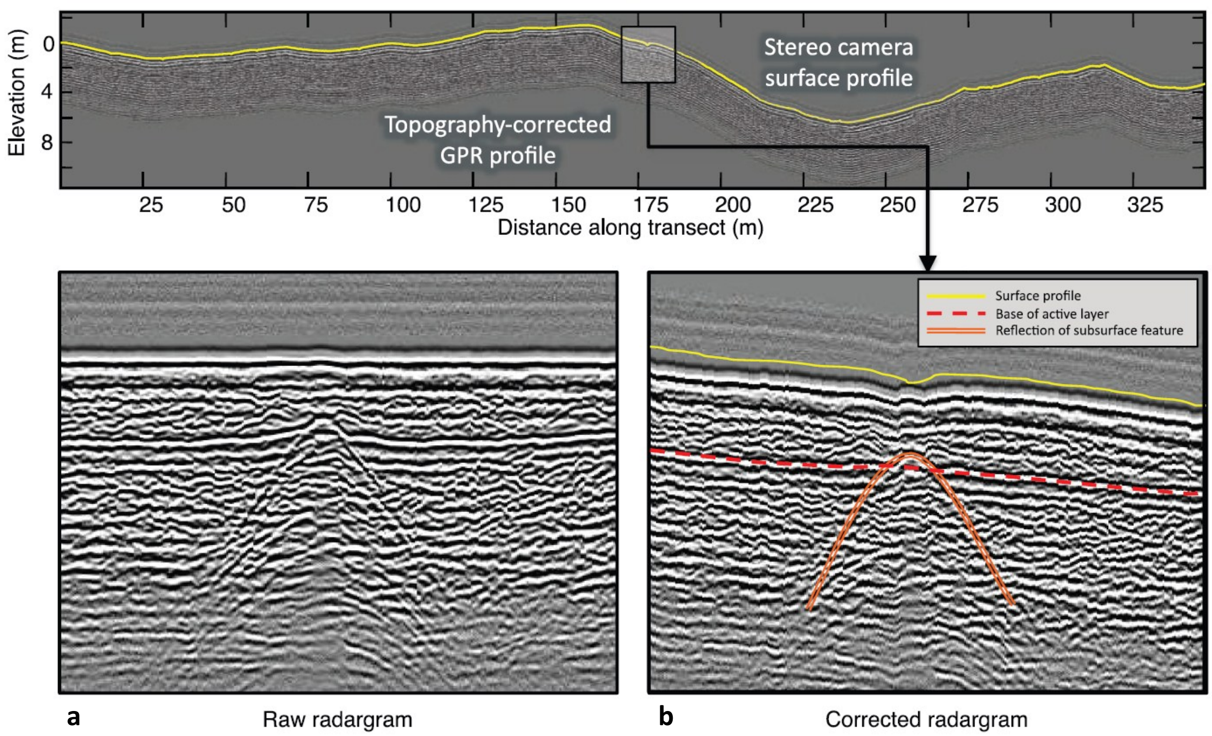

Figure 2.12. These images from Furgale et al. (2010) demonstrate the use of a stereocamera to topographically correct GPR along a transect on Devon Island in the Canadian High Arctic. The uncorrected radargram is shown in (a) and the corrected radargram is shown in (b). In (b), the subsurface feature characterized by a hyperbola is interpreted to be an ice wedge. This interpretation is supported by a surface depression indicative of a trough directly above it.

Preface to Chapter 3

Chapter 3 is the first of two manuscripts to be submitted to peer-reviewed journals for publication. It has been written in accordance to the guidelines set by McGill University's Graduate and Postdoctoral Studies Office.

In chapter 3, the application of capacitively-coupled resistivity (CCR) and ground-penetrating radar (GPR) for the detection and assessment of ground ice is presented. As discussed in the Study Objectives, this is the first paper that attempts to optimize the post-processing of CCR data to effectively map ground ice properties. GPR is employed to provide more detailed information on cryostructure, and thus, explain anomalies observed in the CCR surveys.

Improving the confidence of geophysical tools to map ground ice is a prerequisite for Chapter 4. In this chapter, the spatial applicability of one-dimensional maximum active layer thickness projections is discussed using geophysical results.

Chapter 3 - The application of CCR and GPR to identify diverse forms of ground ice at Parsons Lake, Northwest Territories

Michael C. Angelopoulos[1], Wayne H. Pollard[1], and Nicole J. Couture[2]

[1] Department of Geography, McGill University, Montreal, QC
[2] Geological Survey of Canada, Ottawa, ON

ABSTRACT

Capacitively-coupled resistivity (CCR) and ground-penetrating radar (GPR) surveys were performed in an area of ice-rich permafrost at Parsons Lake, a potential hydrocarbon development site. Since ground ice is an important factor affecting the level of disturbance initiated by thermokarst, improving the use of non-invasive geophysical tools to map its nature and extent is important. This paper focuses on the application of CCR and GPR to map ground ice by relating the tool's outputs to permafrost properties available from borehole logs and thermal modelling results. By employing depth of investigation (DOI) indices and varying inversion parameters, optimal degrees of data smoothing were calculated, and thus, the CCR's capacity to identify various forms of ground ice was maximized. GPR cross-sections were applied to provide more detailed information on cryostructure and contacts between massive ice and gravelly sand deposits.

3.1 INTRODUCTION

The nature and distribution of ground ice is one of the most problematic geological variables in permafrost areas. Permafrost underlies 23.9% of the northern hemisphere including 50% of Canada (Y. Zhang et al., 2008). The volume of ground ice in permafrost varies from nearly a few percent in dry permafrost to nearly 100% in the case of ice wedges, ice lenses, and massive ice bodies. Occurrences of massive ground ice are widely reported in the Mackenzie Delta areas of the Western Canadian Arctic (e.g. Mackay, 1971; Pollard and Dallimore, 1988; Mackay and Dallimore, 1992; Murton, 2005).

Mapping ground ice distribution is an enormous challenge facing land management and resource development related to oil and gas in the Mackenzie Delta. The melting of ice destabilizes permafrost, leading to extensive thaw subsidence called thermokarst. Human activities related to oil and gas exploration, as well as climate change effects associated with rising temperatures are expected to increase permafrost degradation in the Western Canadian Arctic (Maxwell, 1997).

Traditional methods for identifying ground ice involve the drilling of holes to directly measure ice content. This technique is expensive, destructive, and only provides point samples. Furthermore, lateral interpolation between holes is unreliable in areas of high variability. The success of geophysical tools in permafrost environments depends on the variations in physical properties between unfrozen/frozen materials and ice-rich sediments/ice-poor sediments (Kneisel et al., 2008). Capacitively-coupled resistivity (CCR) is effective for quantifying the electrical properties of near-surface materials and ground-penetrating radar (GPR) is useful for imaging the near-surface structure and stratigraphy of permafrost (e.g. Moorman et al., 2003). Each of these geophysical tools has been used to map various aspects of permafrost, but only a few studies have incorporated two or more systems in a complementary fashion (e.g. de Pascale et al., 2008; Calvert et al., 2001).

Although there have been many investigations of permafrost using direct current resistivity (DCR), there is a lack of quantitative analyses that aim to assess how reliable CCR is for mapping ground ice properties. This study focuses mainly on an ice-rich area of planned hydrocarbon development at Parsons Lake, NWT. At this site, permafrost data is available from multiple boreholes (Kiggiak-EBA, 2004) and thermal models (Manuscript 2). Hence, correlations between geophysical outputs and permafrost properties can be drawn. The primary objective of this paper is to understand how seasonal changes in the near-surface thermal regime and surficial geological conditions affect geophysical outputs, and hence, conclusions about ground ice distribution. Through a series of post-processing experiments, determining the optimal balance between observed data consistency and smoothing was attempted for CCR. This should allow scientists to minimize the variability of mapped electrical properties for a specific ground ice type, but also maximize the differences between different ground ice forms (e.g. massive ground ice versus ice-rich peat). In order to enhance interpretations, GPR surveys were also performed to acquire detailed information on ice structure. Using geophysical tools to detect permafrost properties should enable land use planners to quickly and inexpensively evaluate the thermokarst risk of future Parsons Lake development sites.

3.2 BACKGROUND

In order to avoid repetition, geophysical theory is not discussed in this manuscript. When submitted for publication, this section will include shorter versions of sections 2.4 and 2.5.

3.3 STUDY AREA

Parsons Lake (68°59' N, 133°33' W) is located above the tree line approximately 75 km north of Inuvik (Figure 3.1). Inuvik has a mean annual air temperature of -8.8 °C and a total annual precipitation of 248.6 mm (Environment Canada). Situated in continuous permafrost, the Parsons Lake area is characterized by widespread massive ground ice (Mackay and Dallimore, 1992). Borehole data show that materials overlying massive ground ice bodies are fine-grained with segregated ice, while the underlying sediments tend to be coarse-grained. Of 26 cores at Parsons Lake, 16 display this stratigraphic pattern. The exceptions are boreholes situated in a flat-lying peat deposit, on gravel pads constructed in the 1970's, and those positioned on former drilling sumps. Only two boreholes from undisturbed locations do not contain massive ground ice in the upper 16 m of the subsurface. The borehole labels are consistent with the nomenclature presented in the Kiggiak-EBA geotechnical assessment report.

In undisturbed areas, the two primary surficial geological categories are peat soils and mineral soils. Peat soils tend to have lower mean annual surface temperatures and thinner active layers than mineral soils provided that snow depths are similar between the two sites (Williams and Smith, 1989). Given that peat soils contain less unfrozen water in the near-surface compared to mineral soils during the thawing season, these environments should theoretically result in relatively less signal attenuation for geophysical investigations.

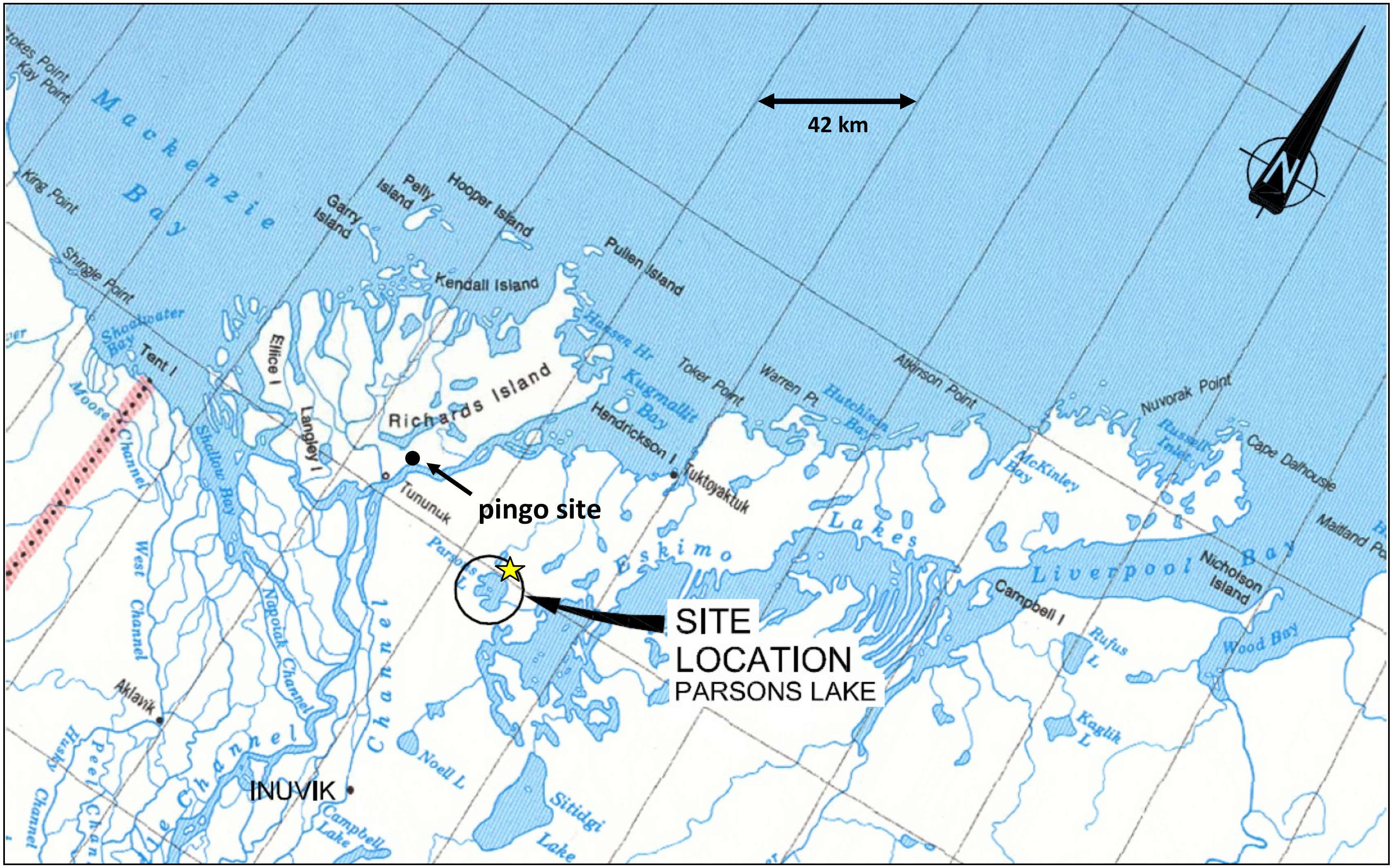

Figure 3.1. The locations of Parsons Lake, the pingo site, and Inuvik in the Western Canadian Arctic (Kiggiak-EBA, 2004). The star, which represents the study site, is located on the northeastern side of Parsons Lake.

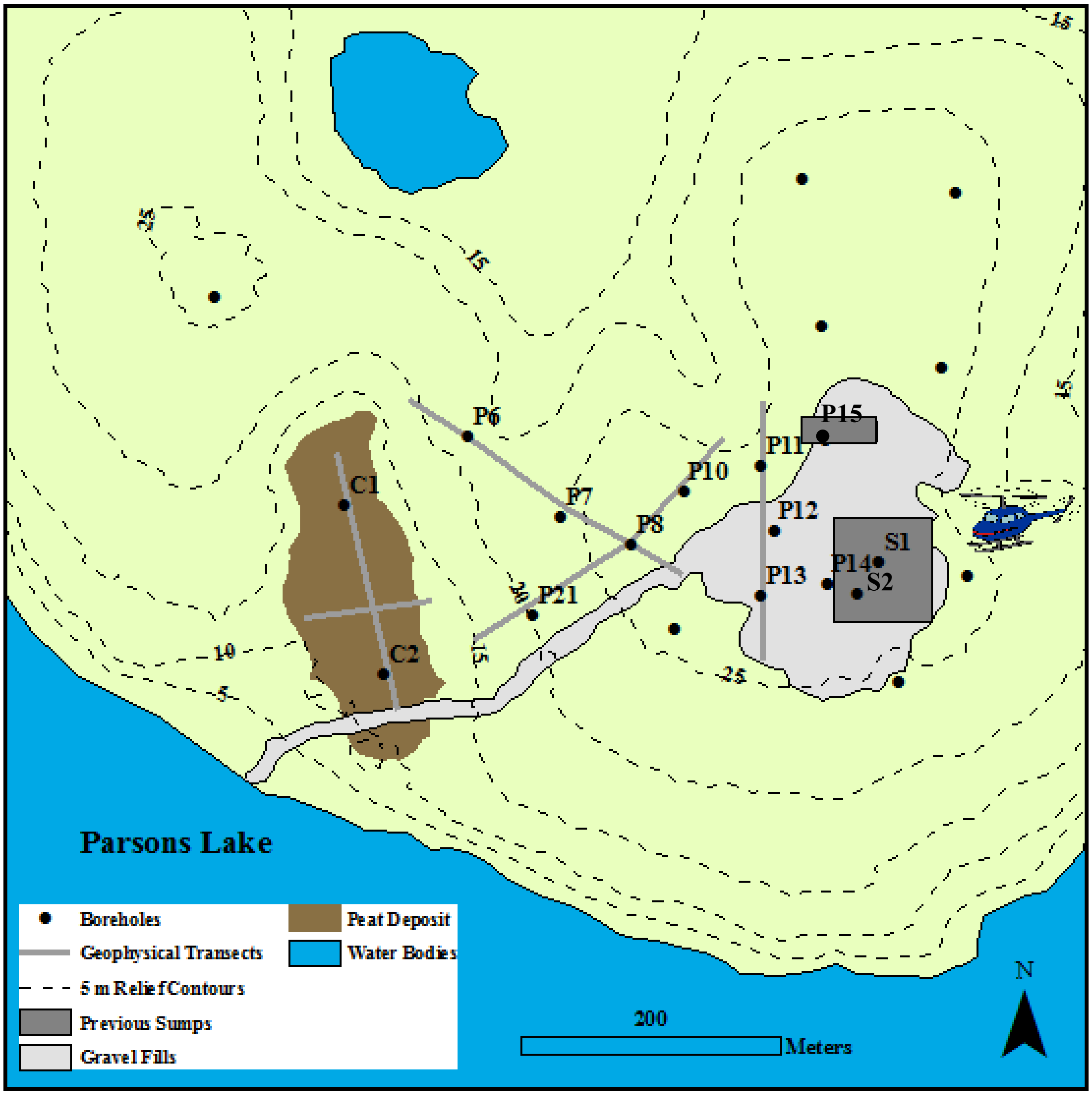

Figure 3.2 (top). Study site map created in ArcGIS. The contour lines and former drilling sumps were generated by digitizing a topographic map from Kiggiak-EBA's geotechnical assessment report (2004). The gravel fill and peat deposit areas were estimated using a georeferenced aerial photo.

Figure 3.3 (left). Aerial photograph of the study site taken in July 2009. The view is from the front of the helicopter icon shown in Figure 3.2. The photograph's saturation settings were adjusted to enhance colour differences between different terrain types.

3.4 DATA ACQUISITION

In July 2009 and 2010, GPR and CCR surveys were conducted over a range of surfaces, including a flat-lying peat deposit, mineral soils with a thin organic layer (≈ 15 cm), as well as a disturbed site consisting of shallow gravelly sand deposits (Figures 3.2 and 3.3). In order to examine seasonal changes in electrical resistivity, CCR surveys were also performed across the peat sites in March 2010. Topographic corrections to the profiles were acquired with a Trimble differential global positioning system (DGPS) at 5-10 m intervals across all transects.

The TR1 capacitively-coupled resistivity system designed by Ohmmapper Geometrics was used for all surveys. The instrument is deployed in dipole-dipole configuration where the transmitter and receiver are placed in a line and separated by a user-defined distance. The system has a relatively high lateral resolution and relatively poor vertical resolution compared to alternative array types (Loke, 2010). Hence, it is most suitable for mapping vertical features like taliks (Associated Geosciences, 2010). The tool induces an alternating current (AC) into the ground at a frequency of 16.5 kHz and AC voltage measurements are made at the receiver's dipole. With the intention of generating pseudosections to a depth of approximately 10 m, the distance between dipoles for individual surveys across one transect ranged from 5-35 m. The n factor, a multiplier used to relate the dipole length to the dipole-dipole separation distance, increased monotonically from 1 to 7 for all investigations (refer to Table 3.1).

Table 3.1. Survey design for CCR investigations

Transect	Date	Dipole length, *a* (m)	Distance between dipoles, *n*a* (m)
C1-C2	March 22, 2010	5	5,10,15,20,25,30,35
C1-C2	July 19, 2010	5	5,10,15,20,25,30,35
P6-P8	July 20, 2010	5	5,10,15,20,25,30,35
P21-P10	July 22, 2010	5	5,10,15,20,25,30,35
Pingo	March 21, 2010	5	5,10,15,20,25,30,35

The MALA Geoscience RAMAC rough terrain concept antenna (RTA) was used for all GPR surveys. The system operated with a central frequency of 50 MHz, which allowed for greater depth penetration, but a weaker resolution compared to higher frequency technology. This frequency was selected in order to increase the probability that the GPR would achieve at least the maximum penetration depth of the Ohmmapper. The RTA, which consists of a transmitter and receiver separated by 4 m, is flexible and easy to use, especially for undulating landscapes. The GPR recorded data continuously under the settings specified in Table 3.2. The time window refers to the amount of time the receiver is instructed to wait for a signal return, and the time interval specifies how often a pulse is generated.

Table 3.2. Survey design for GPR cross-sections

Transect	Date	Time Window (μs)	Time Interval (s)
P6-P8	July 20, 2010	20.00	1.00
P21-P10	July 21, 2010	20.00	0.25
Pingo	March 8, 2009	Missing	Missing

3.5 DATA PROCESSING

3.5.1 Inversion Strategy

MapMap2000, post-acquisition processing software, was used to generate pseudosections from data collected with the Ohmmapper. The pseudosections were converted for use in RES2DINV, a 2D resistivity and induced polarization (IP) inversion software. First, the data files were adjusted to account for topographic changes across the survey lines. A high-degree polynomial function was fit to each transect's DGPS measurements to calculate topography at 1 m intervals across the survey lines. This was incorporated in the inversion process. The program attempts to build a model capable of generating the observed apparent resistivity values. Then, the calculated apparent resistivity values are compared with the observed apparent resistivities. If the misfit is greater than a user-defined tolerance, the model parameters are adjusted and the inversion process is repeated until it converges to acceptable error level (Loke and Barker, 1996).

Similar to Sasaki (1992), the data files were imported using model cells with a width of half the unit electrode spacing (5 m) to ensure a reasonable compromise between model resolution and computer processing time. The resistivity values were then examined for bad data points caused by noise or poor electrode coupling with the surface. Since elevation values were incorporated with the positions of the electrodes, a finite-element mesh was used to carry out the inversion. Multiple damping factors were tested to determine the optimal balance between data smoothing and observed data consistency. Inversions were carried out with maximum damping factors ranging from 0.01 to 0.4. In accordance with previous studies like Hauck and Vonder Muhll (2003), the maximum damping factor was set to a value of five times the minimum damping factor for each test. Since the resolution of resistivity surveying decreases exponentially with depth, the damping factors were increased for each successively deeper layer using automatic calculations built into the software. Larger damping factors result in a larger the degree of smoothing in the inversion process. For all tests, the L_2 norm or smoothness-constrained inversion method (deGroot-Hedlin and Constable, 1990; Ellis and Oldenburg, 1994) was selected to compute the misfit between the logarithms of the measured and calculated apparent resistivity values. More specifically, the L_2 norm minimizes the sum of squares of the data misfit and produces a root mean square (RMS) error. Furthermore, the L_1 norm or robust inversion method was used for the model roughness filter. Here, the L_1 norm technique (Claerbout and Muir, 1973) attempts to minimize the sum of the absolute values of spatial changes in model resistivity. The latter tends to work well in areas with sharp subsurface transitions (Loke et al., 2003) like permafrost areas, which consist of unfrozen/frozen soil boundaries in the thaw season, as well as abrupt contacts between ice-poor sediments and massive ground ice structures. For the simulations in this paper, the inversion process converged if either the RMS error was less than 5% or the relative change between iterations was less than 5%.

Addressing the quality of the field data is important, because model cells with low sensitivity can generate anomalously high or low resistivity zones (Oldenburg and Li, 1999). Loke (1999) identifies a few ways in which to reduce the impact of poor quality data. The first method involves exterminating bad data points from the pseudosections. Since the pseudosections were visually investigated for relatively high or low apparent resistivity values and nothing unusual was found, any section of poor data quality is likely spread out. Alternatives to manual data extraction include the use of larger damping factors and the application of the L_1 norm inversion technique for calculating the data misfit between the observed and calculated apparent resistivity values. This inversion method is less sensitive to outliers (Farquharson and Oldenburg, 1998), but since no obvious outliers were observed in the dataset, the L_2 norm inversion technique for the data misfit was used for several damping factors. After each simulation, the depth of investigation (DOI) test introduced by Oldenburg and Li (1999) was performed to assess the accuracy of the result.

3.5.2 Depth of Investigation Calculations

The DOI test (Oldenburg and Li, 1999) is an empirical method for determining the depth of investigation of a dataset by performing at least two inversions of the dataset using different constraints. It has been used by Marescot et al. (2003) and Hauck and Vonder Muhll (2003) for mountain permafrost studies, as well as by Hilbich et al. (2009) and Fortier et al. (2008) for rock glaciers and permafrost mounds, respectively. For the DOI calculations, each model is assigned a reference resistivity, which is taken as the average of the logarithm of the apparent resistivity values. When the inversion is carried out, the output is termed the reference resistivity model (m_1). When the reference resistivity is changed, each cell is usually assigned a value of one tenth or ten times the reference resistivity. In some cases, extreme perturbations of one hundredth or one hundred times the reference resistivity are needed. The choice on whether to make the reference resistivity more conductive or resistive depends on the nature of the subsurface targets. If the features being mapped are resistive, then the reference resistivity should be made more conductive, and if the targets are conductive, then the reference resistivity should be made more resistive. When the inversion is performed, the output is termed the altered resistivity model (m_2). Comparing the altered model to the reference model is referred to as a one-sided test. In some cases, the subsurface contains both resistive and conductive targets (e.g. alternating ice-rich and ice-poor zones; ice wedges enclosed by ice-poor permafrost). For situations like this, two altered resistivity models (one is made more conductive and the other more resistive) are compared. This latter is also known as a two-sided test. For all transects, a two-sided test, as well as the two types of one-sided tests were carried out. An example of a DOI calculation for a one-sided test is shown in Eq. 3.1, where m_r refers to the reference resistivities applied. The DOI approaches a value of zero where the altered resistivity models generate the same values as the reference resistivity models. In these zones, the cell resistivity is well constrained by the data. In areas where the model cells contain minimal information about the cell resistivity, the DOI approaches a value of 1. Hence, areas with low DOI values are considered reliable and areas with high DOI values are considered unreliable. Oldenburg and Li (1999) suggest that a reasonable cautious cut-off value is 0.1. When a reference model is used in the inversion process, a self-damping factor (α_s) is required to determine the degree of impact the reference resistivity has on the inversion process. For all tests, a relatively high value of 0.1 was used. The horizontal and vertical damping factors (α_x and α_z) were set to 1.0, and as a consequence, equal weights were given to horizontal and vertical features in the inversion process.

$$DOI\ (x,z) = \left| \frac{\log(m_1(x,z)) - log(m_2(x,z))}{m_{r1} - m_{r2}} \right| \quad \textbf{[3.1]}$$

The finite-element mesh used to calculate the DOI values should extend to the edge of the survey lines and to a depth of approximately three to five times the median depth of investigation of the largest electrode spacing used. The pseudodepths for each layer prior to inversion are equal to the median depth of investigations provided by Edwards (1977) for various n-factors and dipole-dipole array lengths. For all simulations, the mesh was extended to a depth of 3.5 times the maximum pseudodepth (Figure 3.4). Similar to Edwards (1977), the thickness of the top layer in the mesh was set to half the median depth of investigation of the shortest electrode spacing used. The thickness of each successively deeper layer was increased by 10% to account for the resolution's exponential decrease with depth (Loke and Dahlin, 2002). There is confidence in the mesh geometry and the self-damping factor, because the DOI values at the bottom of the models exceeded 0.2 (Oldenburg and Li, 1999). Since the bottom cells near the edge of the survey line should theoretically have DOI values close to 1.0, the scaled DOI test proposed by Oldenburg and Li (1999) was applied for all simulations. The scaled DOI is calculated by Eq. 3.2, where DOI_{max} is the maximum value calculated by Eq. 3.1.

$$Scaled\ DOI\ (x,z) = \left| \frac{\log(m_1(x,z)) - log(m_2(x,z))}{DOI_{max}(m_{r1} - m_{r2})} \right| \quad \textbf{[3.2]}$$

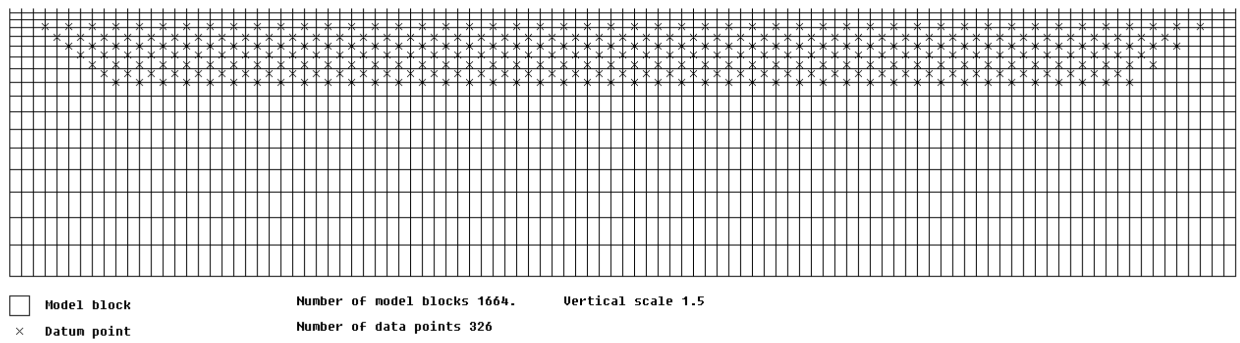

Figure 3.4. An example of a finite-element mesh extended to 3.5 times the maximum pseudodepth

Once all the scaled DOI values were calculated, most of the results were interpolated using the kriging method in Surfer, a 2D and 3D subsurface mapping package. Kriging uses values at known points to estimate the value of a point where no data exists. Unlike alternative interpolation methods like inverse distance weighting, kriging optimizes the weights given to each known point with the use of a variogram. In a variogram, the variability between pairs of points is plotted as a function of the distance between pairs of points. Hence, the average distance for which two data points are not related can be found. For this procedure, it was assumed that no directional bias (i.e. anisotropy) existed for the aforementioned correlation. Once the DOI contour lines were generated, they were superimposed on the inversion outputs. In the Results section, the only exception to the kriging interpolation method is mineral transect 2. For this transect, the inverse distance weighting method was used, because the high resistivity anomalies were quite small. Hence, the smoothing associated with the kriging technique generated 0.1 DOI contours with insufficient variation to identify zones that could be spurious.

3.5.3 GPR

ReflexW was used for the processing and interpretation of the GPR data. The data files first were adjusted to account for topographic changes across the survey lines. Dewow, time-gain, and background removal filters were applied to all GPR data. The dewow filter is used to remove very low frequency components from the cross-section (Annan, 2005). The algorithm works in one dimension (i.e. for each trace) and calculates the average amplitude over a time window equal to one principal period of the electromagnetic wave (20 ns for 50 MHz). The mean is then subtracted from the central point of each window. Subsequently, an energy decay time-gain function was executed to compensate for signal strength loss with depth. The background removal filter acts on a chosen number of traces over a specified time and distance range. By subtracting the average trace from the chosen range, the filter suppresses horizontally coherent energy and emphasizes signals which vary laterally. The algorithm was applied for parts of the cross-sections, but only between what was interpreted as the top of massive ground ice and the maximum depth of investigation (i.e. point at which the signal strength approaches the background noise level). This, in some cases, permitted the removal of temporally consistent noise (i.e. ringing) within the profile and made the ground ice structures easier to interpret.

3.6 RESULTS

3.6.1 Mineral Transect 1

As shown in Figure 5, the three DOI tests explained in section 3.2 were carried out and superimposed on the unaltered resistivity model. All the images illustrated in Figure 5 were processed with a maximum damping factor of 0.01. Since there are clearly both conductive and resistive subsurface targets, the two-sided test is most effective at highlighting relatively high resistivity zones that could be unreliable. The more conductive and resistive models were assigned a reference resistivity of ten times and one tenth the unaltered reference resistivity, respectively. Between 50 and 85 m, as well as between 165 and 240 m, resistivity values exceed 100 000 Ω at depths ranging from 5.6 m to 15.4 m. Represented as a thick black line, the DOI contour of 0.1 is positioned just above the top of the aforementioned features. Resistivities of approximately 30 000 Ω present between 37.5 m and 50 m, as well as from 147.5 m and 160 m, however, are situated above the 0.1 DOI contour. Hence, the maximum resistivities considered to be reliable are close to 30 000 ohm. If a maximum damping factor of 0.05 is used, the DOI tests show better results. As shown in Figure 6, the resistivities in what were originally the two anomalous zones fluctuate between 25 000 and 40 000 Ω. Furthermore, all three DOI tests suggest that these results are reliable. In the middle of the cross-section (87.5 m to 145 m), the subsurface is more conductive. Between a depth of 4 m and the 0.1 DOI contour, resistivities range from 2800 to 6200 Ω. Across the same horizontal segment of the cross-section, there is also a noticeable difference in the near-surface properties compared to the rest of the survey line. Here, resistivities fluctuate between 1000-2000 Ω up to a depth of 4 m, whereas, other areas are more conductive with resistivities less than 1000 Ω. In this region, the DOI also extends to a greater depth. At a position of 100 m, the 0.1 DOI contour is located at a depth of 20 m. According to the borehole logs for P6, P7, and P8, the depths to the top of massive ground ice range from 1.8 to 2.4 m. Conversely, resistivity does not plateau until 5.6 m. This demonstrates the relatively poor vertical resolution of a dipole-dipole CCR system (Loke, 2010).

CCR surveys were complimented with GPR, which has a comparatively better resolution. More specifically, the vertical resolution of a 50 MHz GPR antenna is 0.5 m when the EM wave is travelling at a speed of 110 m/μs (a value typical for permafrost). As shown in Figure 7a, the GPR cross-section is able to resolve the active layer, as well as top of massive ground ice. The diffraction pattern with coordinates of (165,-3) was used to determine a suitable average EM velocity. The diagonal reflector intersecting P7 is representative of the transition from massive ground ice to a gravelly sand deposit, and knowing that GPR is capable of distinguishing between the two materials is important, particularly for mineral transect 2. The GPR also illustrates two well-defined zones of intense scattering between 10-50 m, in addition to 90-130 m. When viewed with the CCR cross-section at an equal vertical exaggeration (Figure 7b), these areas are located in the more conductive regions of the subsurface below the active layer. The shallow lateral changes in resistivity demonstrate the instrument's sensitivity to unfrozen water content, which will be discussed in greater detail for the peat deposit.

3.6.2 Mineral Transect 2

The three DOI tests explained in section 3.2 were carried out and superimposed on the unaltered resistivity model (Figure 8). All the images illustrated in Figure 8 were processed with a maximum damping factor of 0.01. Since the subsurface is predominantly resistive, a one-sided test with a disturbed conductive model is most effective at highlighting relatively high resistivity zones that could be unreliable. Unlike mineral transect 1, the reference resistivity needed to be adjusted by a factor of 100 so as to demonstrate that the feature seen between 160-180 m could be spurious. The rise of the 0.1 DOI contour in the feature is more easily visible in Figure 9b. Compared to mineral transect 1, the high resistivity anomaly is small, which could explain why the structure is not completely enclosed by the contour. With the exception of the aforementioned zone, the ground ice body is characterized by reliable resistivity data in the upper 10 m of the ground. Unlike mineral transect 1, the resistivities for mineral transect 2 are fairly uniform from 55-230 m. In particular, the values range between 25 000 and 40 000 Ω. On the left side of borehole P21, however, there is a slight reduction in resistivity from 30-45 m. Here, values oscillate below and above 15 000 Ω. Note that P21 is one of only two boreholes on site that do not contain massive ground ice in the upper 15 m of the subsurface. Instead, the core is comprised of a silty clay layer in the upper 2 m, which is underlain by sandy gravel and gravelly sand units up to a depth of 16.4 m. The average volumetric ice content in the coarse-grained deposit is 31%, but a thin ice-rich sand unit with a volumetric ice content of 85% is encountered between a depth of 3.4 and 4.6 m. Despite the minor decline in resistivity, CCR does not map a clear transition from massive ice to coarse-grained materials.

On the other hand, the GPR cross-section (Figure 9a) displays an unmistakable v-shaped structure from 15-95 m. The depression, which represents the contact between coarse-grained materials and underlying massive ground ice, reaches a maximum depth of 17 m. The reflector intersects borehole P21 at a depth of 13 m. This is greater than 16.4 m (depth to the top of massive ground ice observed from the borehole), but the P21 core does not consist of any other major stratigraphic contacts. Hence, the error between the recorded and GPR depths is likely due to an inaccurate EM velocity, as well as inexact horizontal positioning of the borehole. Furthermore, the reflector's depth changes rapidly over short distances, and as a consequence, any minor misalignment between the GPR's position on the surface and the location of its measurements could generate erroneous results. Between 205-235 m at relative elevations ranging from 7 to -1 m, there is increased scattering of the radar signal. Since the latter is in the form of multiple overlapping diffraction patterns, it likely represents small heterogeneities in the ice. Similar to transect 1, the GPR does not suggest that continuous sediment layers exist within massive ice anywhere along the profile.

3.6.3 Pingo Transect

To test our method, an unconstrained survey was conducted across a small pingo located adjacent to the East Channel of the Mackenzie River on eastern Richards Island (close to

Swimming Point). A pingo has a reasonably predictable internal structure, and thus, the survey was expected to detect an ice/ice-rich core. The pingo is characterized by a long axis measuring approximately 150 m and a maximum height of 10 m. Since closed-system pingos are common ice-rich landforms in the Mackenzie Delta (Mackay, 1966), CCR surveys were performed to observe how similar electrical resistivity values are between pingo ice and the massive ice at Parsons Lake. In addition, GPR cross-sections were carried out to compare ground ice structure between the two sites. Unlike the mineral transects at Parsons Lake, the GPR cross-section suggests a stratified cryostructure of intrasedimental massive ice (Figure 3.10a). Below the base of the snowpack, a strong unbroken reflector representing the top of massive ice is absent. Hence, either the veneer of sediment covering the ice is too thin to be resolved, or the sediments contain enough ice to produce a very weak dielectric contrast in the near surface. Throughout the pingo, there are continuous layers, which repeat at successively greater depths. Although no core data exists for validation, these are likely sediment units separating massive ground ice layers. Between 35-50 m, there is a weak diagonal reflector, which could be the boundary between the stratified cryostructure and the enclosing ice-poor sediments. Above the diagonal contact, the CCR results (Figure 3.10b) show an abrupt change in resistivity. The massive ice structure is described by resistivities ranging from 10 000 to 15 000 Ω, whereas the enclosing materials predominantly oscillate around 5000 Ω. Since the GPR and CCR profiles were carried out in back to back years, they are not aligned perfectly. This is demonstrated by the fact that the diagonal shift in resistivity is located roughly 10 m to the right of the diagonal reflector shown in the GPR cross-section.

3.6.4 Peat Transect

In order to examine how resistivity varies seasonally, CCR surveys were carried out in both winter and summer. The three DOI tests explained in section 3.5.2 were carried out and superimposed on the unaltered winter resistivity model (Figure 3.11). All the images illustrated in Figure 3.11 were processed with a maximum damping factor of 0.01. Since resistive and conductive subsurface targets exist, a two-sided test is most effective at highlighting unreliable high resistivity zones below the maximum pseudodepth. Overall, the DOI tests suggest that there are zero artifacts generated by the inversion within the depth of interest (upper 10 m). The borehole logs for C1 and C2 show three major stratigraphic units in the upper 10 m. More specifically, the upper 5 m is dominated by ice-rich peat and icy sediments composed of black clayey silt extend from 5-8 m and 5-10 m for C1 and C2, respectively. Moreover, the icy sediments are underlain by sand and gravel. Compared to the mineral soil transects, the peat deposit is characterized by thicker layers in the near-surface. Hence, the CCR is capable of mapping the transition from ice-rich peat to icy sediments at an accurate depth. In the ice-rich peat zone, resistivities range from 6000-9000 Ω, whereas resistivities range from below 1000 Ω to just under 3000 Ω for the icy sediments. At the core locations, the resistivities for the icy sediments oscillate between 1800-2900 Ω. The high resistivities near the surface are partially affected by snow, but since the average snow depth over the profile was only 35 cm, its influence is probably minor.

In July 2010, a one-sided test with a disturbed conductive model is most effective at isolating relatively low resistivity zones that could be unreliable (Figure 3.12). Between 20-35 m, as well as from 100-113 m and 140-160 m, there are very low resistivity pockets (fewer than 1000 Ω) that fall below the 0.1 DOI contour. Fortunately, these areas do not intersect the boreholes. Unlike the winter tests, electrical resistivity gradually increases from approximately 2500 Ω at the surface to just below 6000 Ω at a depth of 5.6 m. At C1 and C2, resistivities for icy sediments range from 4500-6000 Ω, whereas they swing from just under 1500 Ω to 6000-ohm for the rest of the profile. The most intriguing result is that the icy sediments can be up to three times more conductive in the winter than summer at borehole locations. Although this is possible, as will be addressed in the discussion, the magnitude of the seasonal shift could be exaggerated, because the RMS error is 4.6% larger in the winter compared to summer.

Regressions between resistivity and gravimetric moisture content for C1 and C2 were performed for both seasons. As shown in Figure 3.13, there is a positive linear relationship between the log of resistivity and the log of gravimetric moisture content in winter, but a relatively weak negative linear correlation in summer. This occurs, because the ice-rich zone is situated in the upper 5 m of the subsurface, which undergoes considerable thermal changes throughout the year. Therefore, the unfrozen water component of the total moisture content is likely driving resistivity changes as a function of depth in summer.

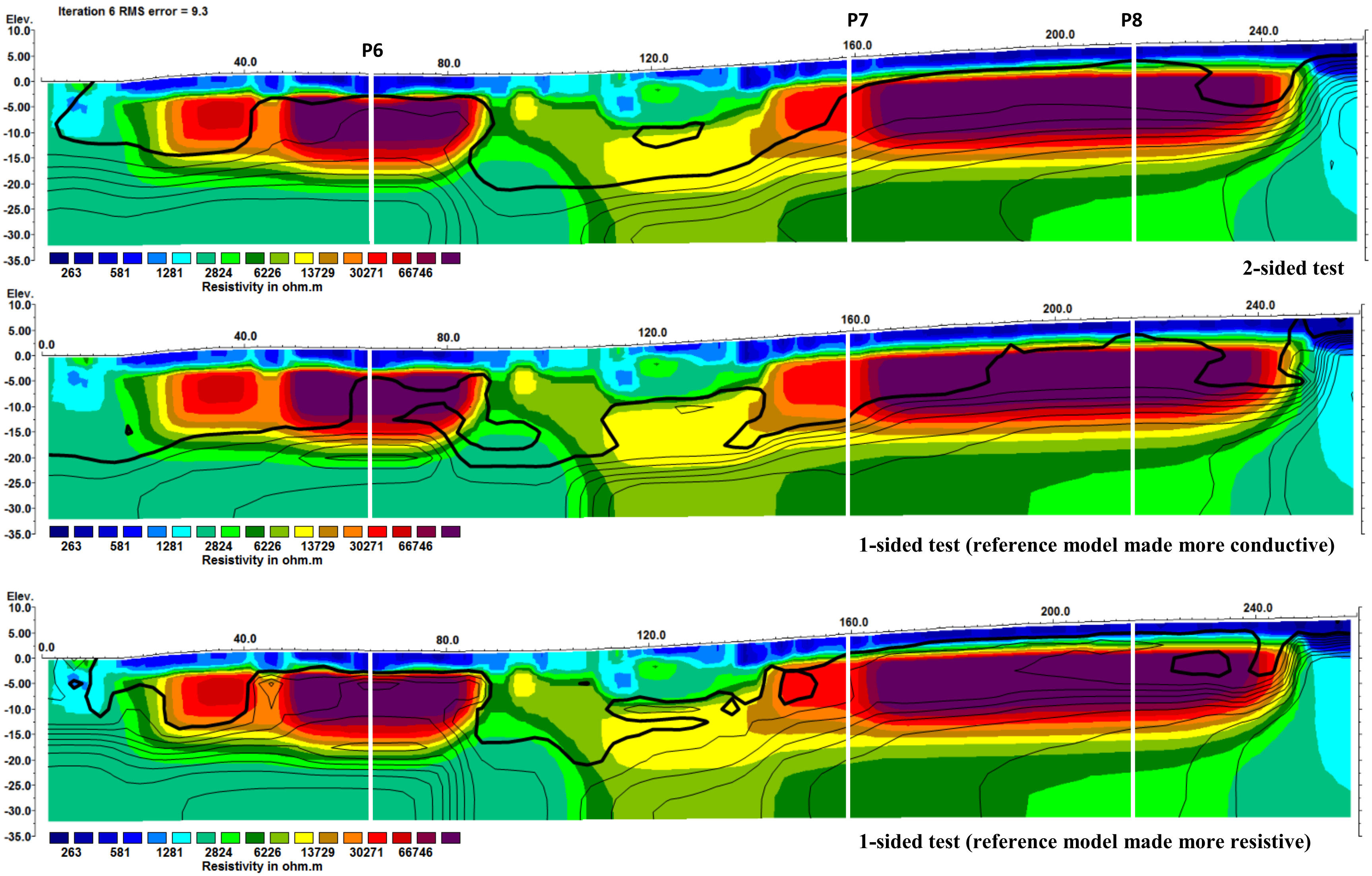

Figure 3.5. The data was collected on July 21st, 2010 and DOI tests are superimposed upon the reference resistivity model for mineral transect 1. The inversions were run with a maximum damping factor of 0.01 and the DOI tests were executed with a perturbation factor of 10. The DOI contour interval is 0.1 with smaller values being closer to the surface. All models cells above the 0.1 contour (thick black line) are considered reliable, whereas model cells below the 0.1 contour are not. The vertical exaggeration of the cross-sections is 1 and all positional units are in metres.

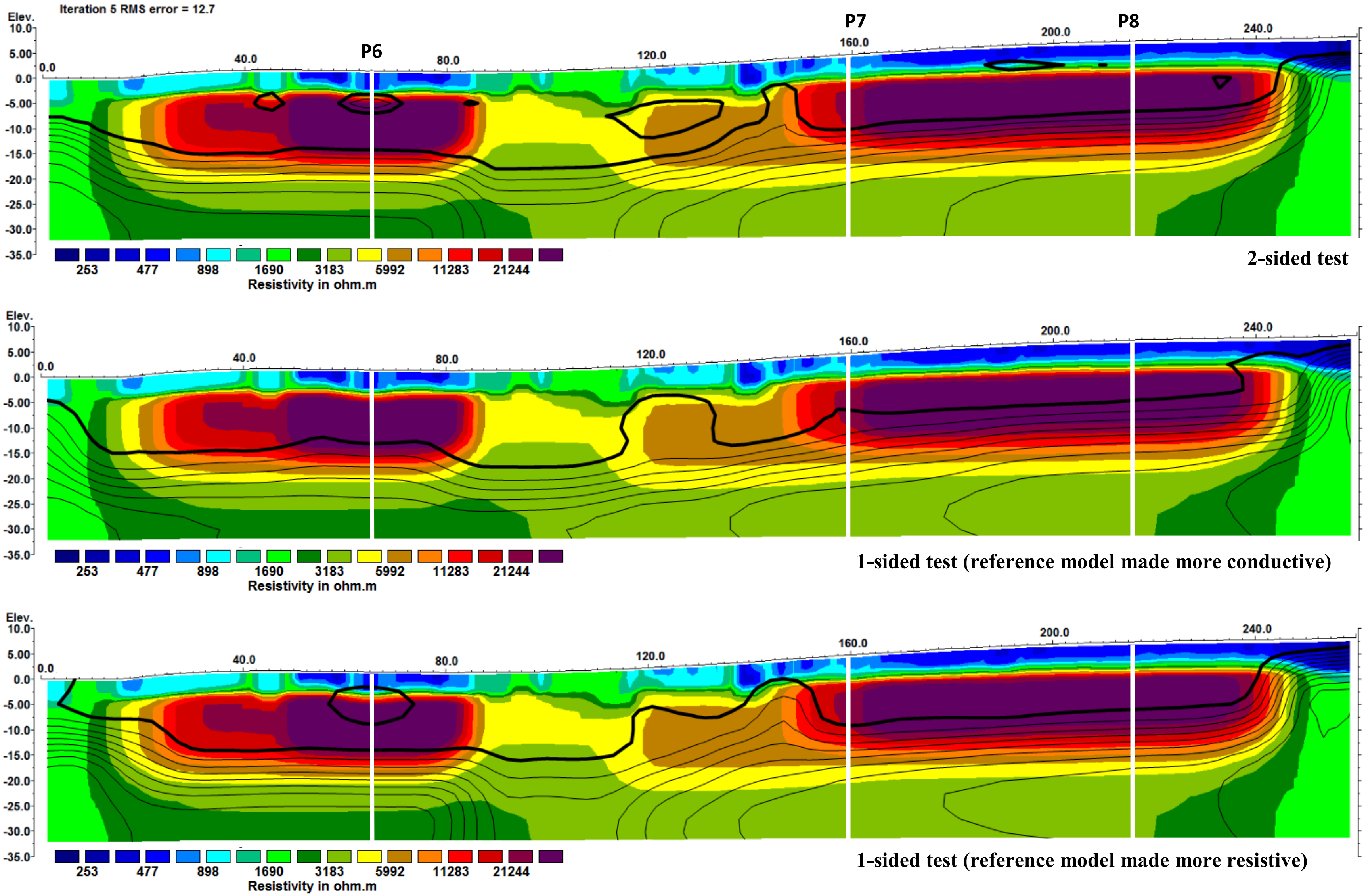

Figure 3.6. The data was collected on July 21st, 2010 and DOI tests are superimposed upon the reference resistivity model for mineral transect 1. The inversions were run with a maximum damping factor of 0.05 and the DOI tests were executed with a perturbation factor of 10. The DOI contour interval is 0.1 with smaller values being closer to the surface. All models cells above the 0.1 contour (thick black line) are considered reliable, whereas model cells below the 0.1 contour are not. The vertical exaggeration of the cross-sections is 1 and all positional units are in metres.

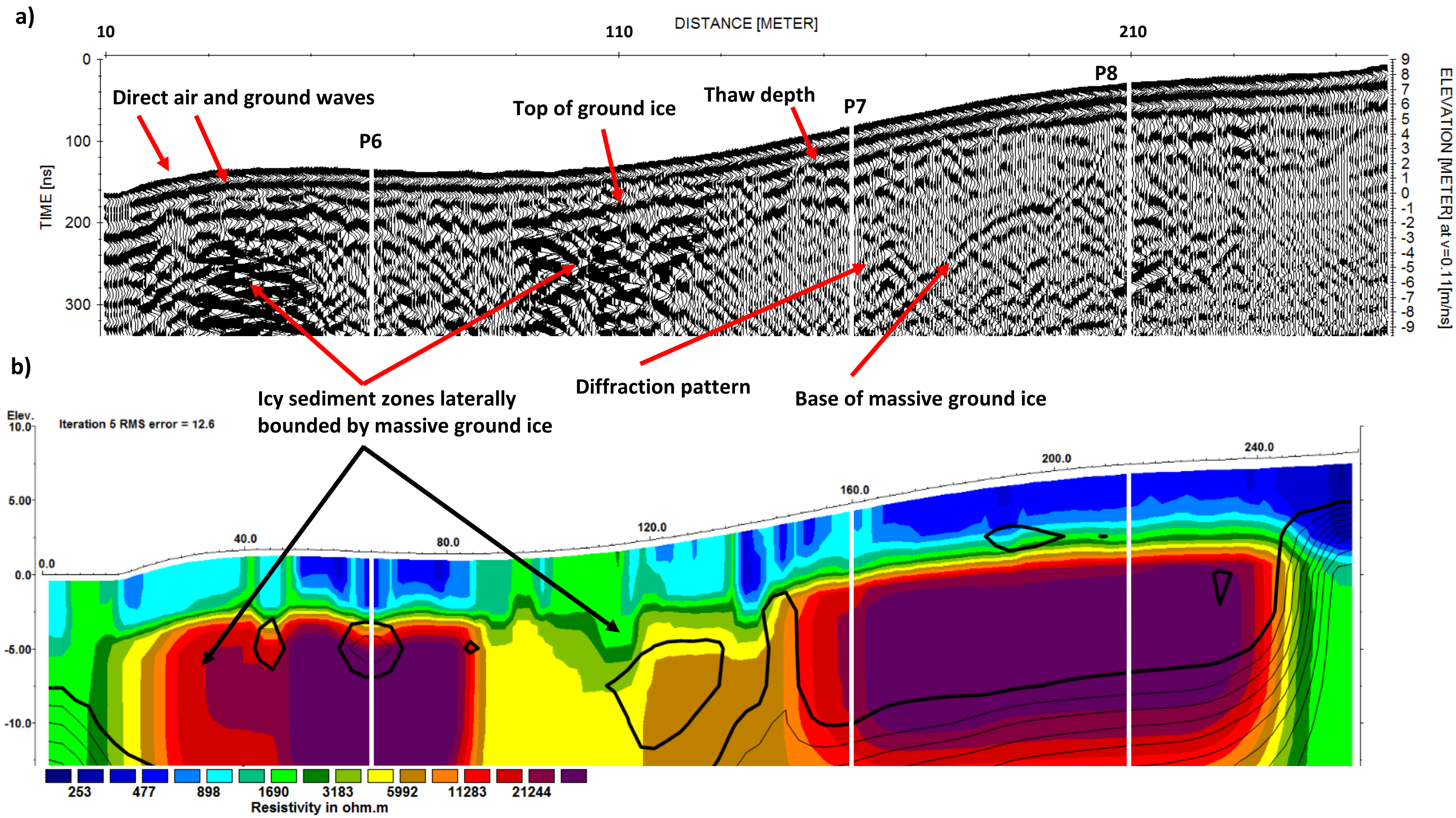

Figure 3.7. The vertical exaggeration of the cross-sections is 2.93 and all positional units are in metres. (a) 50 MHz GPR profile conducted on July 20th, 2010. The two areas of intense signal scattering are interpreted as icy sediments. The icy sediments are surrounded by massive ground ice, which is characterized by homogeneous zones with little or no reflection events. (b) CCR profile carried out on July 21st, 2010. Resistivity for massive ice ranges from 25 000 to 40 000 Ω, while it oscillates between 2800 and 6200 Ω for icy sediments. In (b), the icy sediment and massive ground ice layers start at a depth of roughly 4 m.

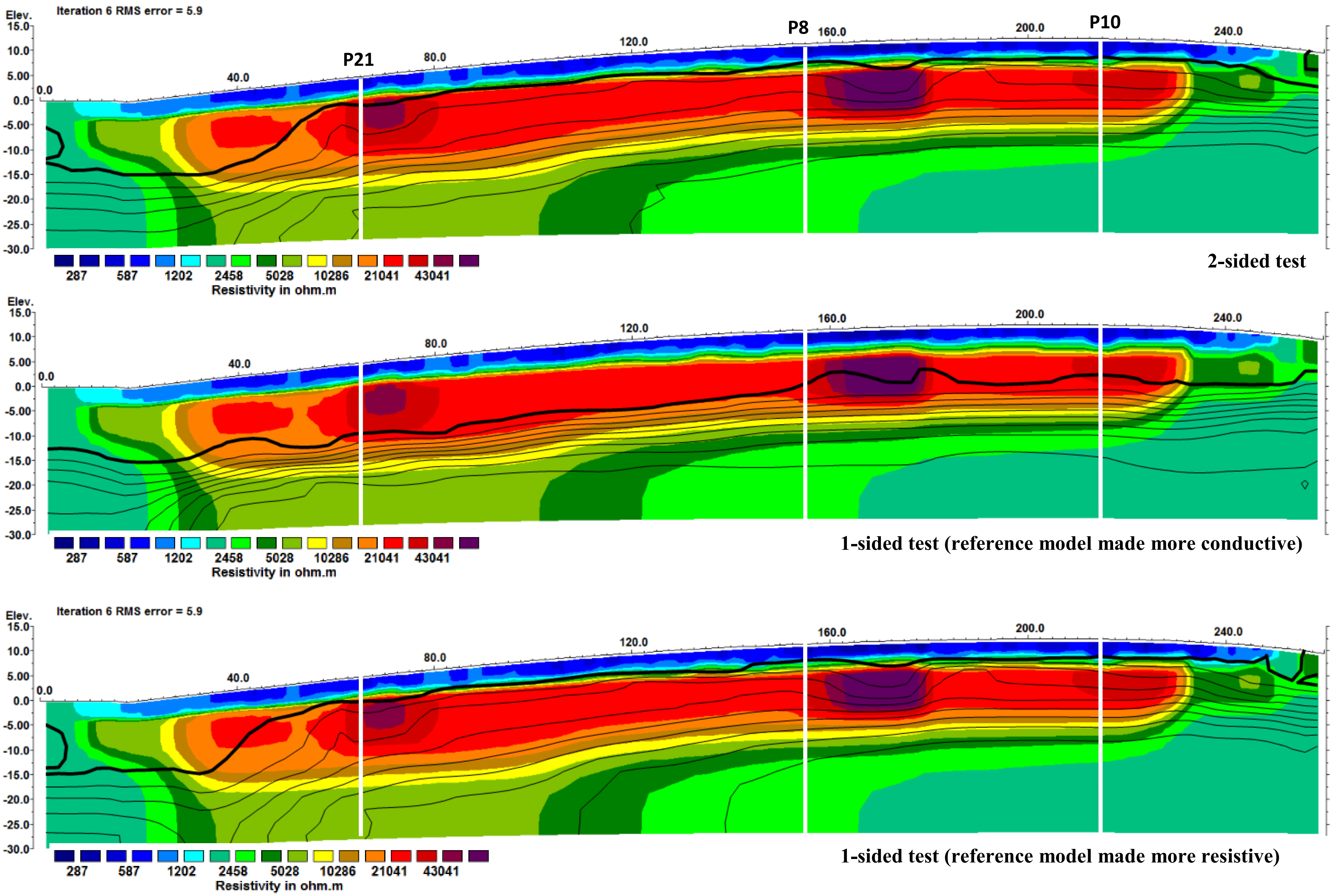

Figure 3.8. That data was collected on July 22nd, 2010 and DOI tests are superimposed upon the reference resistivity model for mineral transect 2. The inversions were run with a maximum damping factor of 0.01 and the DOI tests were executed with a perturbation factor of 100. The DOI contour interval is 0.1 with smaller values being closer to the surface. All models cells above the 0.1 contour (thick black line) are considered reliable, whereas model cells below the 0.1 contour are not. The vertical exaggeration of the cross-sections is 1 and all positional units are in metres.

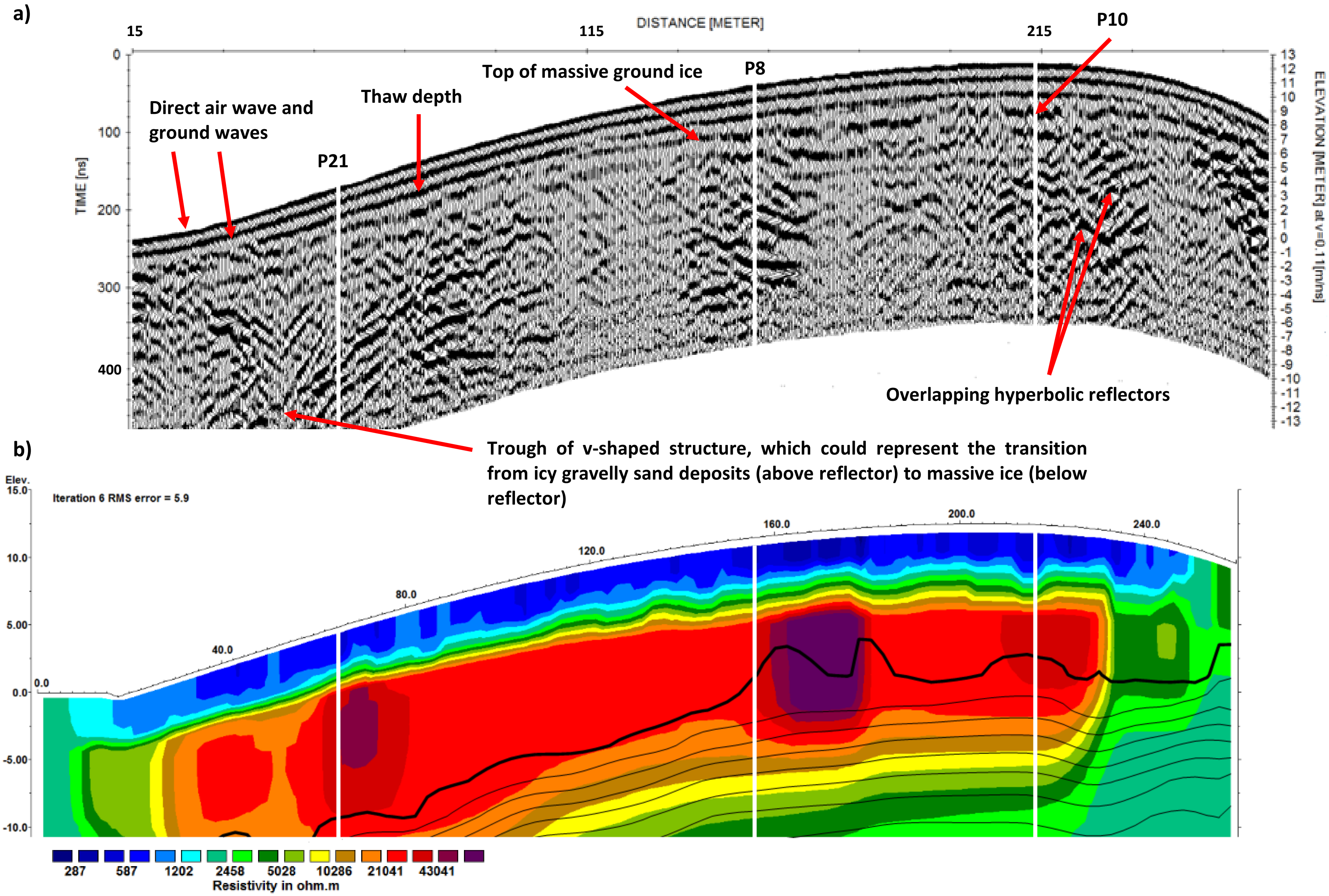

Figure 3.9. The vertical exaggeration of both cross-sections is 2.93 and all positional units are in metres. (a) 50 MHz GPR profile conducted on July 21st, 2010. The overlapping hyperbolic reflectors near P10 likely represent small heterogeneities within the massive ground ice unit. (b) CCR profile carried out on July 22nd, 2010. The image's contents are identical to Figure 3.8 (middle), but the extent and vertical exaggeration are adjusted. CCR does not map a clear near-surface lateral transition from massive ice (observed at P8 and P10) to coarse-grained materials (observed at P21). The lateral transition in near-surface materials occurs at 105 m (right horizontal edge of v-shaped structure shown in the GPR image).

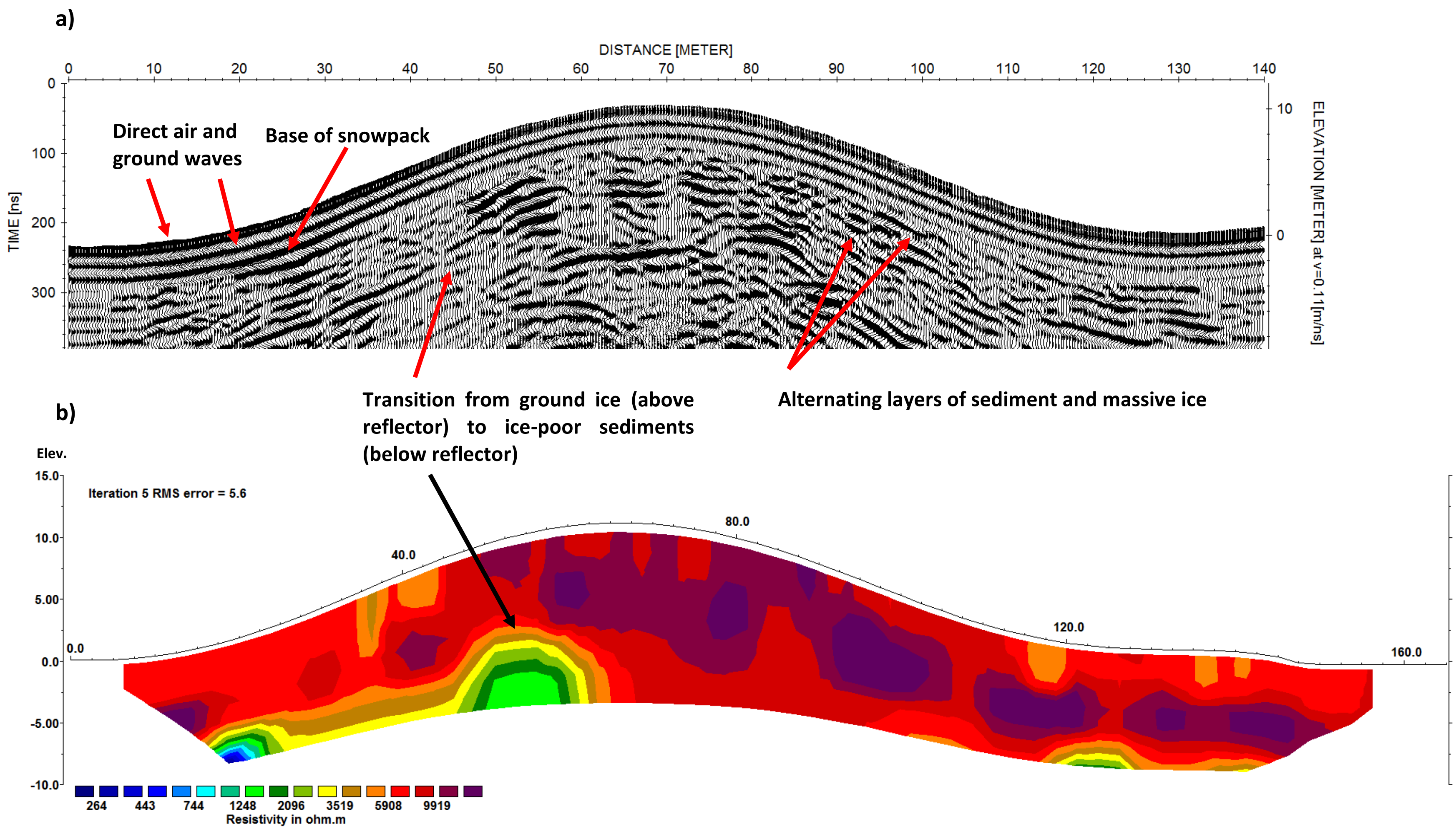

Figure 3.10. The vertical exaggeration of both cross-sections is 1.46 and all positional units are in metres. (a) 50 MHz GPR profile taken along the major axis of a pingo 40 km northwest of Parsons Lake on March 8th, 2009. The cross-section suggests that massive ice layers are thin and are separated by sediment units. The diagonal reflector from 40 to 50 m (horizontal) and 0 to -7.5 m (vertical) could represent the transition from intrasedimental massive ice to ice-poor sediments. (b) CCR profile carried out along the major axis of the pingo on March 22nd, 2010. Since the depth of investigation test introduced in section 3.5.2 was not performed, the finite-element mesh was not expanded for the inversion. All other inversion parameters are consistent with the data processing methodology presented in section 3.5.

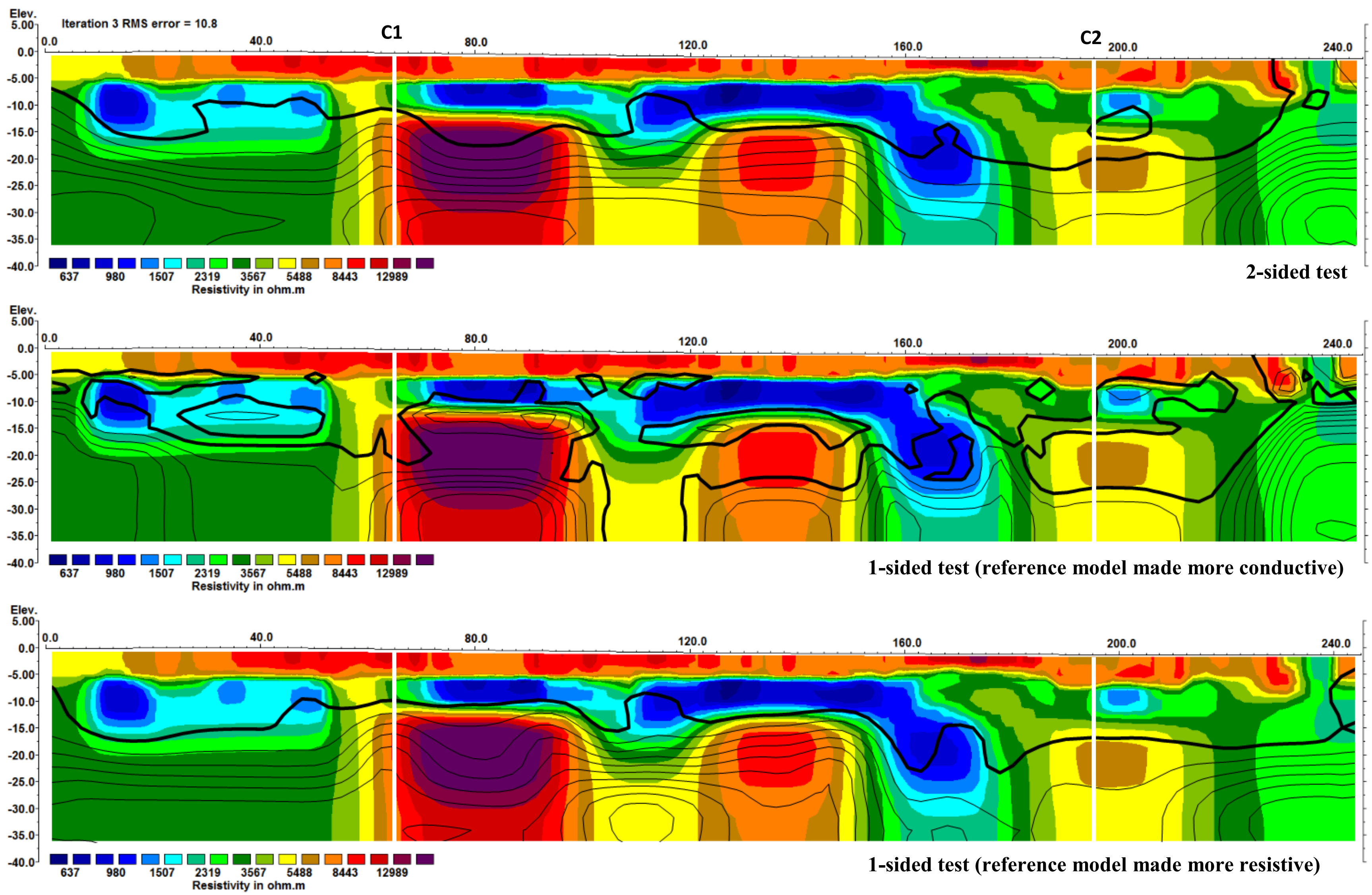

Figure 3.11. DOI tests superimposed upon the reference resistivity model for the peat deposit in winter (March 22nd, 2010). The inversions were run with a maximum damping factor of 0.01 and the DOI tests were executed with a perturbation factor of 10. The DOI contour interval is 0.1 with smaller values being closer to the surface. All models cells above the 0.1 contour (thick black line) are considered reliable, whereas model cells below the 0.1 contour are not. The vertical exaggeration of the cross-sections is 1 and all positional units are in metres.

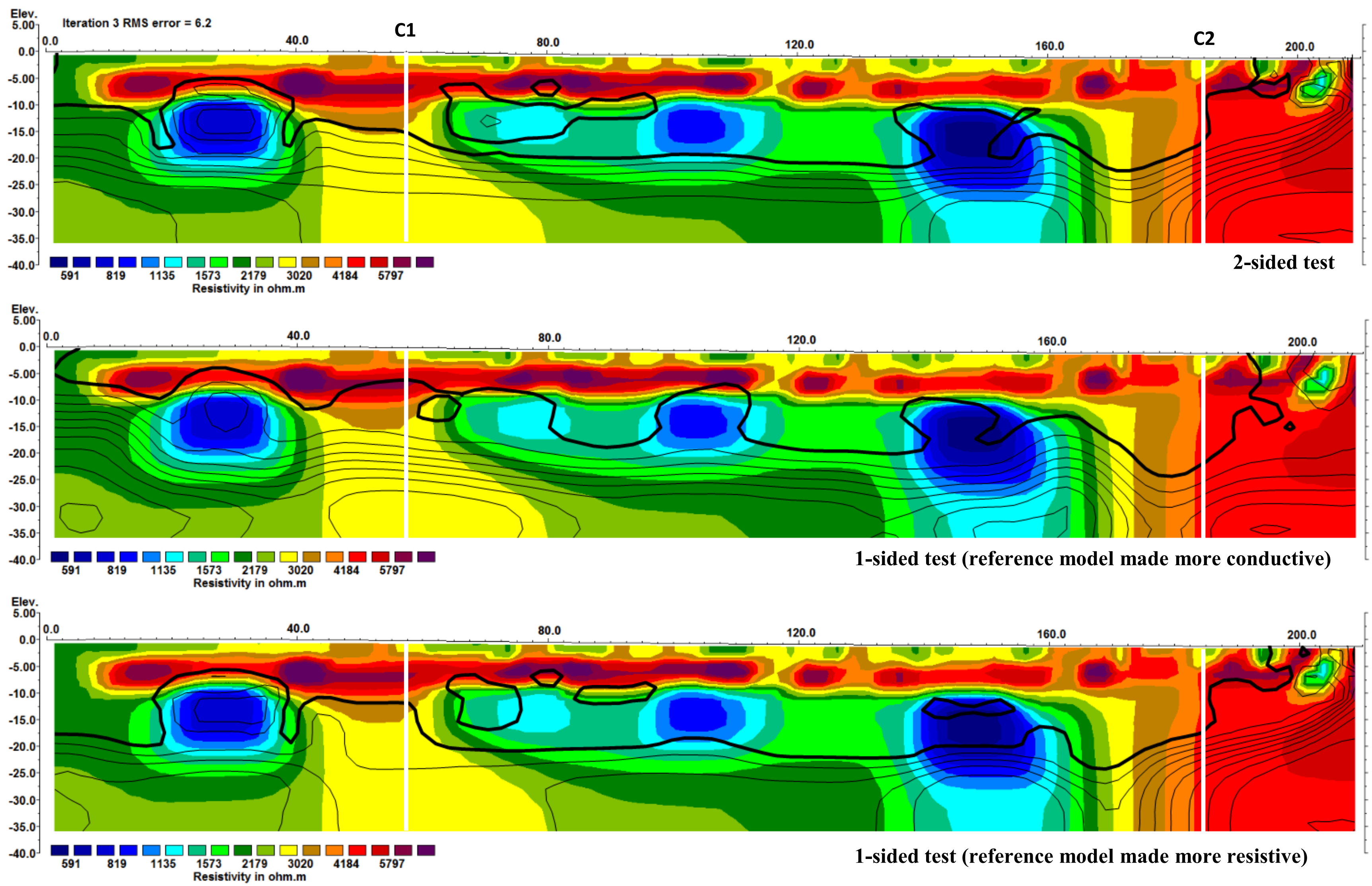

Figure 3.12. DOI tests superimposed upon the reference resistivity model for the peat deposit in summer (July 19th, 2010). The inversions were run with a maximum damping factor of 0.01 and the DOI tests were executed with a perturbation factor of 10. The DOI contour interval is 0.1 with smaller values being closer to the surface. All models cells above the 0.1 contour (thick black line) are considered reliable, whereas model cells below the 0.1 contour are not. The vertical exaggeration of both cross-sections is 1 and all positional units are in metres.

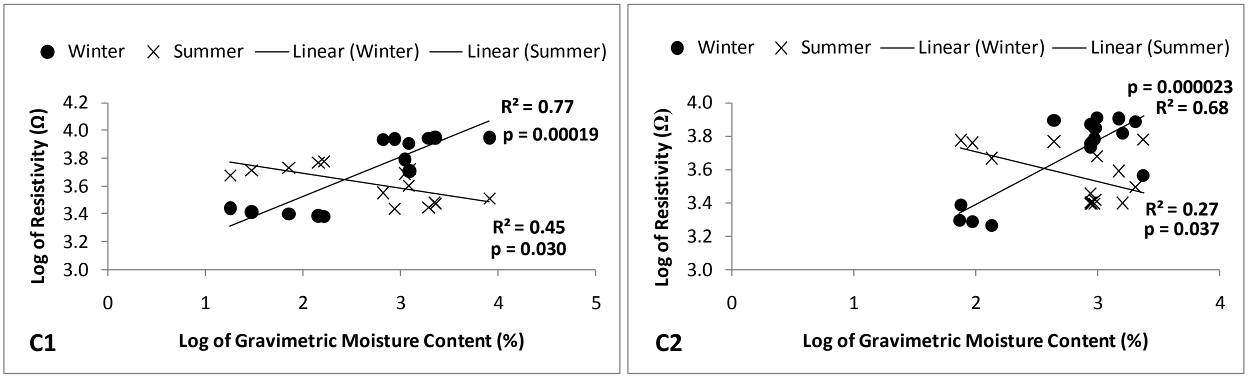

Figure 3.13. High degree polynomial functions were fit to plots of resistivity versus depth for winter and summer results, and the R^2 values for all correlations exceeded 0.99. The functions were used to generate resistivity values at depths containing gravimetric moisture content (GMC) data. Linear regressions between the log of resistivity and the log of GMC were performed for boreholes C1 (left) and C2 (right). The GMC data is from Kiggiak-EBA (2004), and due to variations in active layer moisture contents, GMC data from the top 1 m of the subsurface was not used. The correlations are significant for a 95% confidence level.

3.7 DISCUSSION

The results from the mineral soil (transects 1 & 2) and peat deposit surveys provide strong evidence that CCR is capable of mapping spatial and seasonal changes in ground ice properties. The ability to distinguish between different frozen ground characteristics, however, depends on an optimal selection of inversion parameters. Figure 3.14 plots the maximum or plateau resistivity of vertical slices intersecting boreholes as a function of the maximum damping factor used in the inversion process. For each simulation, a DOI test was carried out to quantify data quality. All points with a DOI greater than 0.1 are shown in red and are considered unreliable. The optimal resistivity values are deemed to be those that are correlated with the smallest possible damping factor capable of generating a DOI less than 0.1. For transects 1 and 2, the most favourable maximum damping factors are 0.05 and 0.01, respectively. If a maximum damping factor of 0.01 is used for both profiles, the resistivity values show a greater degree of scattering for a specific ground ice type (thick massive ice in this case). More specifically, resistivities range from 30 000 to 140 000 Ω. As a result, the preservation of unreliable data points could force one to conclude that ground ice properties are drastically different between the two profiles. Ground-truth data from the cores, however, suggest that they are similar.

Transect 1 is interesting, because of the unmistakable and abrupt lateral change in electrical resistivity. The more conductive region is interpreted as a zone of icy sediments, because the gradual increase in resistivity with depth suggests that resistivity is dependent on the ground thermal regime, and as demonstrated by Hauck (2002), the effects of temperature on resistivity are related to fluctuations in unfrozen water content. Although the high resistivity zones enclosing this region contain more ice, there is not enough sediment to preserve unfrozen water films. The maximum unfrozen water content for a given soil type and temperature develops at saturation when the optimal balance between moisture and sediment volume exists. For parts of this section, the GPR shows increased scattering of the radar signal. Since multiple undersized heterogeneities can exist in icy sediments, GPR supports the conclusions drawn from the CCR survey. From 130-170 m, however, the GPR shows a reflection free response within the conductive area. This could be because, either 1) this portion of the conductive sector has a uniform ratio of ice versus sediment, or 2) the lateral transition in resistivity occurs in more than one dimension. Unlike GPR, the vertical resolution of a CCR survey deteriorates with depth, because apparent resistivities are characteristic of larger volumes as the separation between the transmitter and the receiver increases. In general, this area has a thinner active layer, which results in comparatively higher resistivity and less signal attenuation in the near surface. This is why the 0.1 DOI contour extends to a comparatively greater depth. The formation of the conductive anomaly is subject to debate, but could be due to differential intrasedimental ice formation across the survey line. During ice genesis, growth of a specific lens depends on the balance between the rate at which latent heat is removed (i.e. thermal conductivity and temperature above the freezing front) and the rate at which water is supplied to the system (Smith, 1985). Since the diagonal reflector (Figure 3.7a) representing the shift from massive ice to gravel and sand plunges to a depth of at least 17 m towards the right edge of the anomaly, the moisture migration rate could have been slower in this area. Perhaps the latter in combination with a frost front moving sufficiently fast produced an isolated zone of icy sediments.

Transect 2 is intriguing, because P21 contains no record of massive ice until a depth of 16.5 m. The GPR cross-section suggests that this irregularity is part of a larger v-shaped structure measuring 90 m in length (Figure 3.9a). Although sand and ice have similar dielectric permittivity values, the presence of cobbles in the coarse-grained deposit could have generated increased scattering. Since the electrical resistivity diminishes by roughly 10 000 Ω for only a small fraction of this structure 10 m to the left of P21, CCR does not successfully map the change in near surface materials. This is supported by a Fortier et al. (1994) whose geophysical logging studies show that the apparent electrical resistivities of ice can be similar to those found for saturated sand and gravel at temperatures well below freezing (Hoekstra and McNeill, 1973). Sharma (1997) also shows that even the resistivities of unfrozen gravelly sand mixtures can overlap with those of frozen ground. For this reason, GPR should be used in conjunction with CCR to identify areas within massive ice that may require coring for a more confident assessment of subsurface conditions.

When the correct damping factors are used, Figure 3.14 implies that it is easier to distinguish between thick massive ice (Figure 3.15a) from ice-rich peat (Figure 3.15b) or icy fine-grained sediments (Figure 3.16c). As the damping factor increases, the gap between the maximum electrical resistivities observed between the different cryostructures narrows. For example, it becomes impossible to separate massive ground ice observed in summer from ice-rich peat surveyed in winter with a maximum damping factor of 0.2. Work at the pingo, however, suggests that resistivities for massive ground ice structures could be lower if they are thin and buffered by sediment layers. Hence, distinguishing between this type of massive ice and ice-rich peat could become complicated at an even lower damping factor.

Figure 3.14 also illustrates that the peat deposit experiences seasonal changes in electrical resistivity. In the ice-rich peat layer, these changes are expected, because it is subject to drastic changes in temperature that affect the amount of unfrozen water content present. Although Kujala et al. (2008), as well as Smith and Riseborough (2010) show that a peat might only be subject to 12-6% or 10-3% decline in the unfrozen water content versus total moisture content ratio for a -1 °C to -5 °C drop in temperature, Figure 3.15b suggests that the peat inclusions are interconnected. As a result, the presence of unfrozen water in summer could generate uninterrupted conduits for current flow, which as demonstrated by Fortier et al. (1994) and Bogolyubov (1973), can reduce the resistivity values recorded for ground ice. Furthermore, the icy sediments also point up a seasonal change in resistivity, but for this layer, the winter results are more conductive than the summer results. In a related study (Manuscript 2), it was found that temperatures were warmer between 5-10 m depths in July compared to April. Temperature logs from 2004 exist for model validation, and as shown in Figure 3.16a, the models are accurate to within 1 °C for P6 in the summer. Moreover, the predicted temperatures reproduce the observed cross-over shown at a depth 5 m where the winter thermal regime becomes warmer than the summer thermal regime. The study concluded that the Inuvik climate data used for setting the upper boundary conditions of the model are applicable to Parsons Lake. Although thermal modelling results are not as accurate for the peat site (Figure 3.16b), the study was still able to generate the cross-over seen at a depth of 5 m. When the models were run to predict temperatures during the times of the fieldwork campaign, a thermal cross-over was shown to exist in 2010 as well. Since the icy sediments are composed of black clayey silt, unfrozen water can exist at temperatures below -5 °C (Smith and Tice, 1988). Furthermore, Figure 18c implies that the unfrozen water films could be continuous. Although the thermal studies suggest that the seasonal changes in resistivity between 5 and 10 m depths are due to variations in unfrozen water content, this should be treated with caution due to the principle of equivalency. The latter states that multiple geological models can satisfy a given dataset of apparent resistivity (Associated Geosciences, 2010).

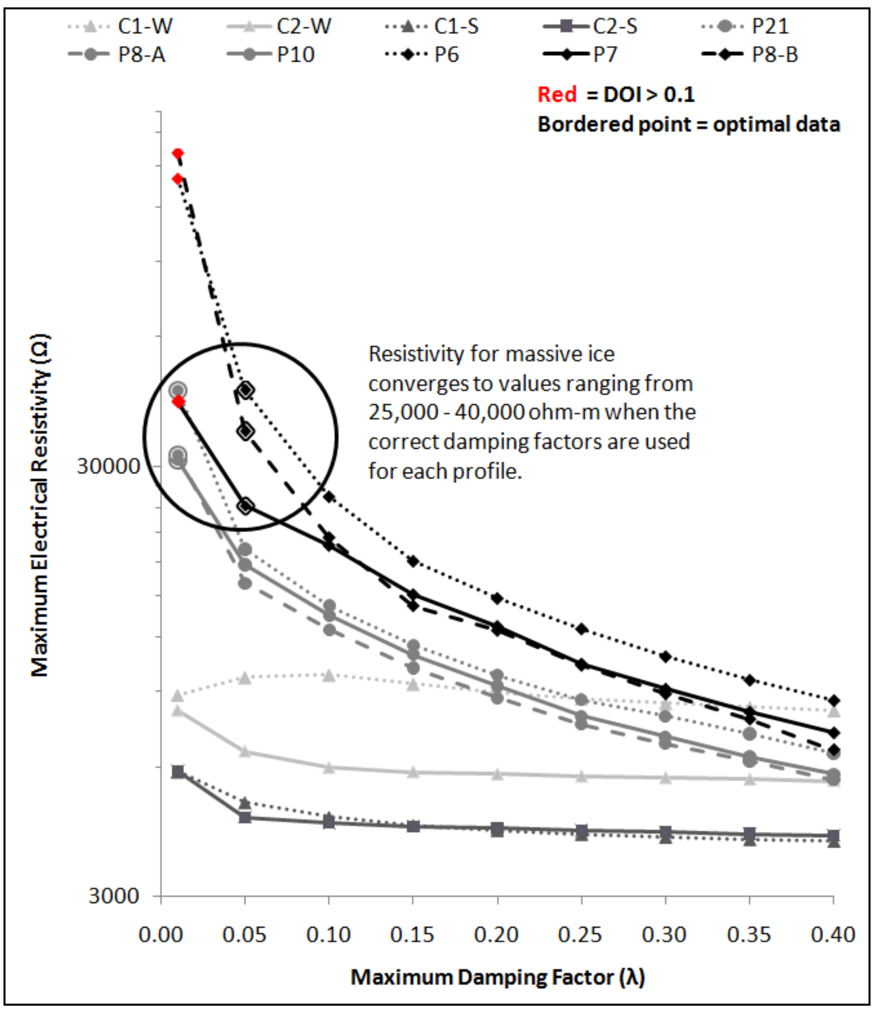

Figure 3.14. Vertical slices of the CCR profiles intersecting borehole locations were analysed from the surface to a depth of 10 m. The maximum resistivity for each slice is plotted as a function of the maximum damping factor used in the inversion. In cases where the resistivity reaches a plateau with depth, the first resistivity value observed for this pattern is used. The symbols W and S pertain to winter and summer, respectively. Since borehole P8 is encountered for two transects, P8-A refers to the P6-P8 survey and P8-B refers to the P21-P10 survey.

The maximum electrical resistivity (MER) values for P6, P7, P8-A, P8-B, P10, and P21 are all associated with massive ground ice. The MER values for C1-W and C2-W pertain to ice-rich peat, whereas the MER values for C1-S and C2-S are associated with icy sediments.

Figure 3.15. Pictures of core segments from the Kiggiak-EBA geotechnical assessment report (2004) for massive ice at P8 (a), ice-rich peat at C1 (b), and icy sediments at C1 (c)

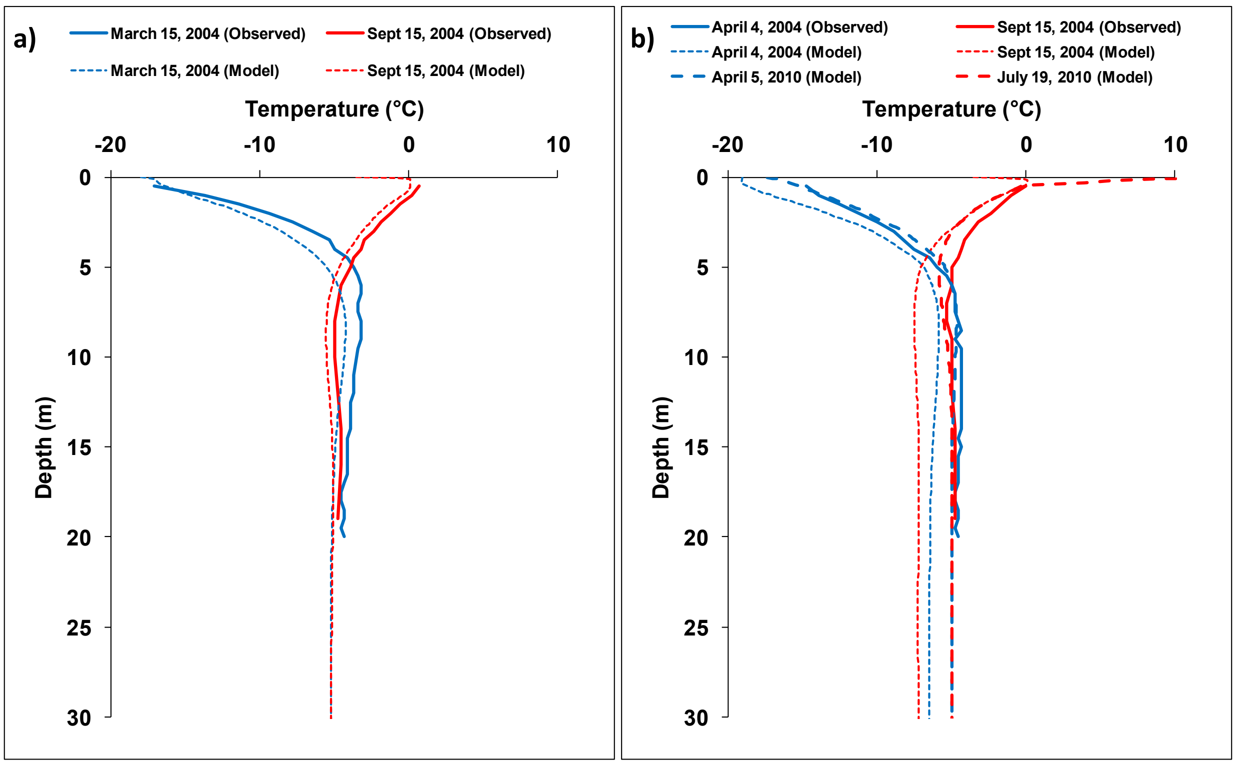

Figure 3.16. The observed temperatures are from the Kiggiak-EBA geotechnical assessment report (2004). In a related study (Manuscript 2), one-dimensional thermal models were constructed using TONE, a heat conduction model. Inuvik climate data and borehole logs were used to set the upper boundary conditions and parameterize subsurface materials, respectively. For borehole P6 (a), the model is accurate to within 1 °C at any depth in summer. Although the thermal model is not as accurate for peat soils at C2 (b), the predicted temperatures are still able to reproduce the thermal regime overlap seen at a depth of 5 m. When the model is run to predict temperatures during the times of the fieldwork season in 2010, a thermal regime overlap is generated again.

3.8 CONCLUSION

When the right combination of inversion parameters is used, CCR can identify areas that could contain massive ground ice at Parsons Lake. Where cores exist for validation, the observed resistivity of massive ice ranges between 25 000 and 40 000 Ω. When the DOI tests are not performed, choosing the correct damping factors becomes difficult, and as a consequence, the range of resistivity for massive ice can be as widespread as 30 000 - 140 000 Ω. Since CCR may generate the same signature for icy deposits of gravelly sand as it does for massive ice, GPR surveys can be performed to identify anomalies within the ice that may require additional coring for a proper assessment of subsurface conditions. The use of GPR is also valuable for mapping sediment layers within massive ice, which as studies at the pingo suggest, could reduce resistivity values. Results also show that CCR can distinguish massive ice from ice-rich peat and icy sediments, but only if an optimal balance between observed data consistency and data smoothing is achieved in the inversion process. At the peat deposit, electrical resistivity is very sensitive to temperature, and thus unfrozen water changes in the near surface, but also at a depths ranging from 5-10 m. Icy sediments composed of black clayey silt display a more conductive signature in the winter compared to summer, and thermal modelling studies suggest that the ground thermal regime in April 2010 is warmer at 5-10 m depths than July 2010. Hence, carrying out surveys in more than one season can help scientists identify areas that experience water phase changes. This, in turn, will allow for a better evaluation of the materials present.

Preface to Chapter 4

Chapter 4 is the second of two manuscripts to be submitted to peer-reviewed journals for publication. It has been written in accordance to the guidelines set by McGill University's Graduate and Postdoctoral Studies Office.

In chapter 4, one-dimensional thermal models are constructed using TONE at previously undisturbed borehole locations. The accuracy of the models is assessed by comparing the outputs to observed temperatures from March, April, and September 2004. The models deemed to be accurate are applied to project maximum active layer thickness values from 2011-2070 based on climate change scenarios for the Mackenzie Valley.

Geophysical surveys are employed to determine which of the MALT developments is most representative of Parsons Lake, as well as to assess the current state of properties beneath the gravel pads. The conclusions drawn from Chapter 3 are central to this discussion.

Chapter 4 - Describing the current and future conditions of the near-surface thermal regime at Parsons Lake, Northwest Territories

Michael C. Angelopoulos[1], Wayne H. Pollard[1], Nicole J. Couture[2], and Daniel W. Riseborough[2]

[1] Department of Geography, McGill University, Montreal, QC
[2] Geological Survey of Canada, Ottawa, ON

ABSTRACT

Ground thermal regime analyses were performed in an area of ice-rich permafrost at Parsons Lake, a potential hydrocarbon development site. During the 2004 ConocoPhillips Canada (CPC) winter drilling program, 26 cores ranging from 7.5 to 33.5 m depths were extracted. Ground temperature measurements were recorded at these sites in March, April, and September 2004. One-dimensional thermal models were constructed at some of the undisturbed boreholes. The material properties and upper boundary conditions were set using the coring results and climate data from Inuvik. Thermal outputs were produced and compared with the observed values, and it was found that the error for the modelling results in September at boreholes described by near-surface mineral soils is less than 1 °C at any depth. By employing mean annual air temperature changes available from regional climate warming studies, these models were used to project maximum active layer thickness (MALT) changes from 2011-2070. In some cases, simulations showed that the MALT increased from 0.72 m in 2011 to 1.80 m in 2058. At this time, the active layer propagates into massive ice, and since the models do not consider geomorphic changes, taliks form in the simulations by 2064. In March and July 2010, capacitively-coupled resistivity (CCR) and ground-penetrating radar (GPR) surveys were carried out between boreholes to identify areas where similar situations might occur. They were also applied in disturbed areas where results suggest a talik might exist today.

4.1 INTRODUCTION

Considerable research on terrain disturbance in Canada and Alaska has been inspired by hydrocarbon exploration activities (e.g., Kurfurst, 1973, van Everdingen, 1979, Lawson et al., 1978, French, 1981, Jorgenson, 1997), but numerous investigations have focused on other types of anthropogenic, as well as natural disturbances (e.g. Forbes, 1996; Radforth, 1972; French, 1975; Mackay, 1995). Lawson (1986), Heginbottom (1973), Brown and Grave (1979), and Walker et al., (1987) provide excellent summaries about permafrost stability and disturbance. Disturbances of the ground surface in permafrost areas inevitably change the surface energy balance, and thus, induce changes in the ground thermal regime. Mackay (1970) states an important factor influencing the level and extent of disturbance is the amount and distribution of various types of ground ice. The geomorphic changes to the ground surface caused by the melting of ground ice are collectively known as thermokarst. Thermokarst is generally initiated in one of two ways. Either, the active layer increases in thickness or part of it is removed. Either way, the top of the underlying permafrost becomes subject to melting.

To enable decision-making about the possible uses and development of an area, projections about future conditions must be made. This is accomplished by modelling how the terrain will respond to changes at the ground surface. Parsons Lake, a potential hydrocarbon development site, is an integral part of the proposed 1200 km pipeline for the Mackenzie Valley. It also lies close to the proposed extension of the Dempster Highway. Hence, assessing the current and future state of the ground thermal regime is important. TONE, a one-dimensional thermal conduction model used in previous permafrost studies (e.g. Smith and Riseborough, 2010; Riseborough, 2007; Sushama et al., 2007; Oelke et al., 2003) was used to model the thermal regime at borehole locations that were part of the 2004 ConocoPhillips Canada winter drilling program. Capacitively-coupled resistivity (CCR) and ground-penetrating radar (GPR) surveys were conducted to characterize subsurface conditions between boreholes and areas that were not thermally modelled. Thermal and geophysical investigations were combined to predict climate warming induced active layer changes and to quantify the spatial applicability of the modelling results. A goal of this research is to provide stakeholders with a preliminary assessment of potential terrain stability problems at the Parsons Lake site. Since the models cannot accommodate subsidence, simulation results beyond the time at which the active layer propagates into massive ice are problematic. Through the application of geophysical tools, ground ice conditions between boreholes are interpolated. This provides scientists with a better understanding of differential terrain responses to climate change in this area, which stakeholders can use to help manage current and planned activities.

4.2 STUDY AREA

Parsons Lake (68°59’ N, 133°33’ W) is located 75 km north of Inuvik (Figure 4.1), which has a mean annual air temperature of -8.8 °C and a total annual precipitation of 248.6 mm (Environment Canada). Situated in continuous permafrost, the Parsons Lake area is characterized by extensive massive ground ice bodies (Mackay and Dallimore, 1992). During the CPC winter drilling program, a description of borehole results was prepared by the Kiggiak-EBA Consulting Group for ConocoPhillips Canada. In the report, information on salinity, active layer thickness, and ground temperatures for 2004 is provided. Most cores display intrasedimental ice that is overlain by fine-grained materials and underlain by sand and gravel. The exceptions include boreholes found on gravel pads (Figure 4.2a) and former drilling sumps, as well as flat-lying peat deposits (Figure 4.2b). The disturbed sites are a result of exploratory drilling activities conducted in the 1970's. With the exception of peat soils, vegetation grows on a thin veneer of unfrozen organic or granular substrate in undisturbed areas (Figures 4.2c & 4.2d). In wet zones, sedges, cotton-grasses and sphagnum moss dominate while drier areas support ericaceous shrubs such as cranberry, bog rosemary and Labrador tea (EIS, 2004).

Salinity values were generally low, ranging from 0.5 to 2.0 parts per thousand (ppt), but values as high as 7.0 ppt were recorded in areas adjacent to former drilling sumps. Active layer measurements for September 2004 varied between 0.4 and 1.0 m in undisturbed areas, while the thaw depth was greater than 1.3 m at disturbed sites. Furthermore, the average ground temperature just below the depth of significant annual seasonal temperature fluctuation (6-8 m) ranged from -4.7 °C to -6.0 °C in undisturbed terrain compared to -2.7 °C to -3.4 °C for disturbed areas. For undisturbed terrain, peat soils experienced colder thermal regimes than mineral soils. For example, the average active layer depth in September 2004 was 0.65 m for undisturbed mineral soils and 0.46 m for undisturbed organic soils. During the fieldwork campaign in July 2010, the average active layer depth for the mineral and peat soils were 0.50 m and 0.33 m, respectively.

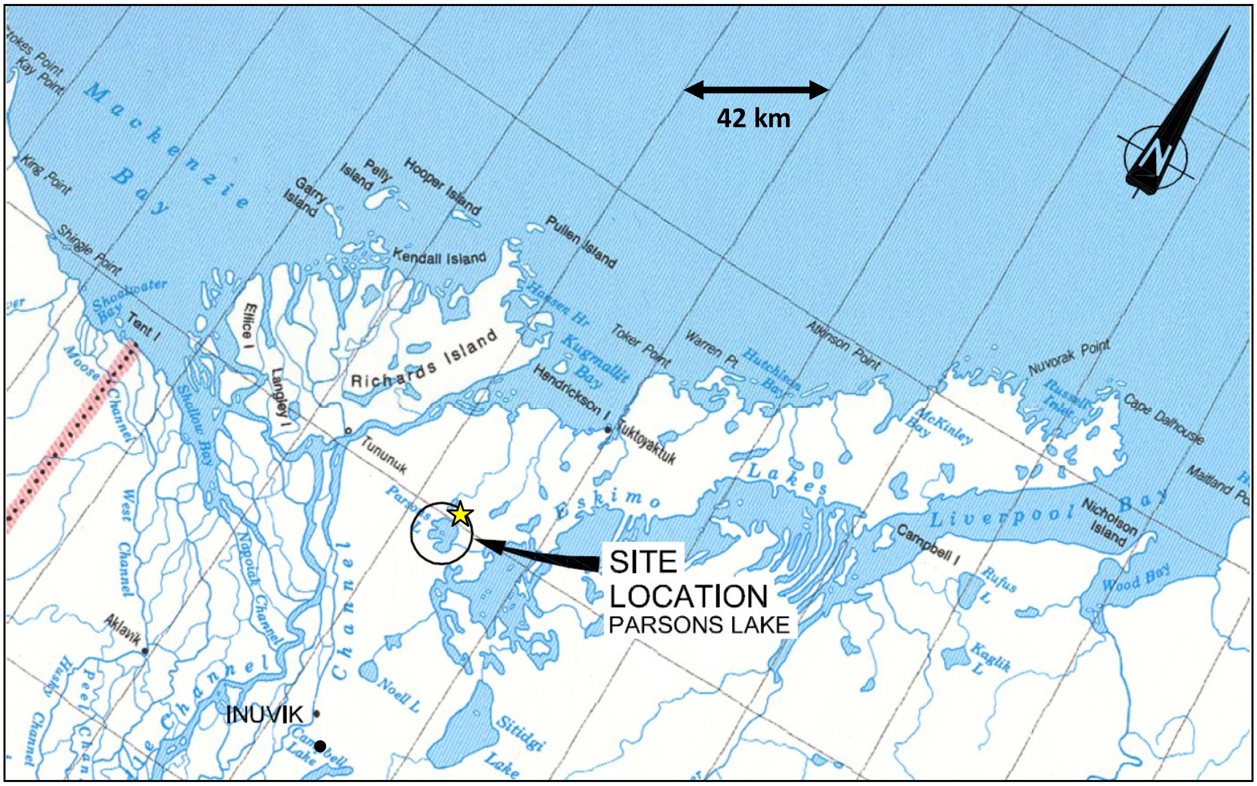

Figure 4.1. The locations of Parsons Lake and Inuvik in the Western Canadian Arctic (Kiggiak-EBA, 2004). The star, which represents the study site, is located on the northeastern side of Parsons Lake.

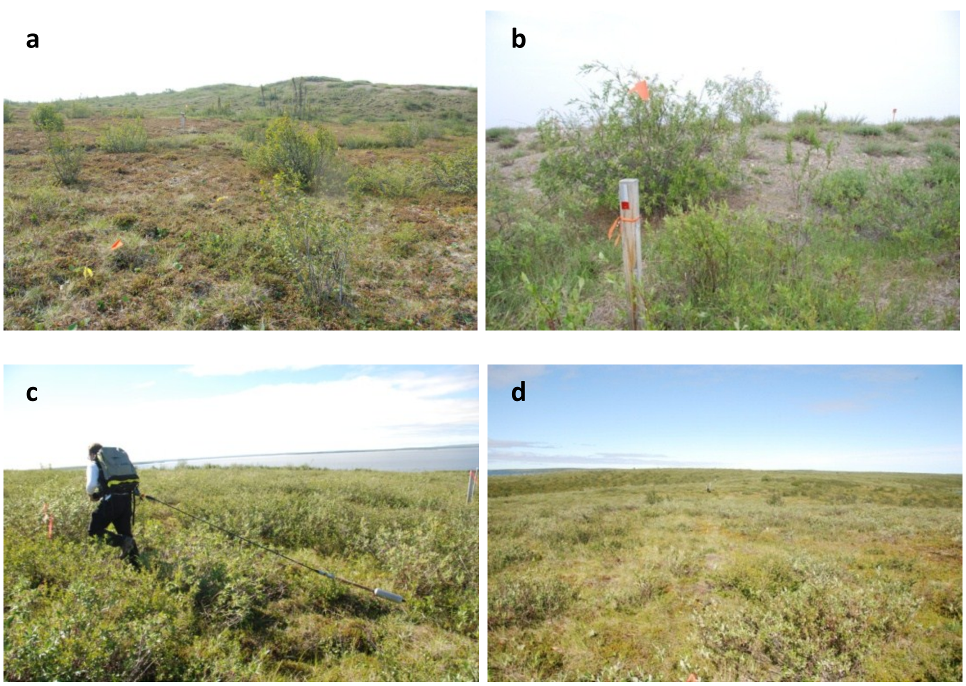

Figure 4.2. Ground cover in the Parsons Lake area includes flat-lying peat deposits (a), gravel fills (b), but most of the terrain is dominated by low shrub vegetation (c and d).

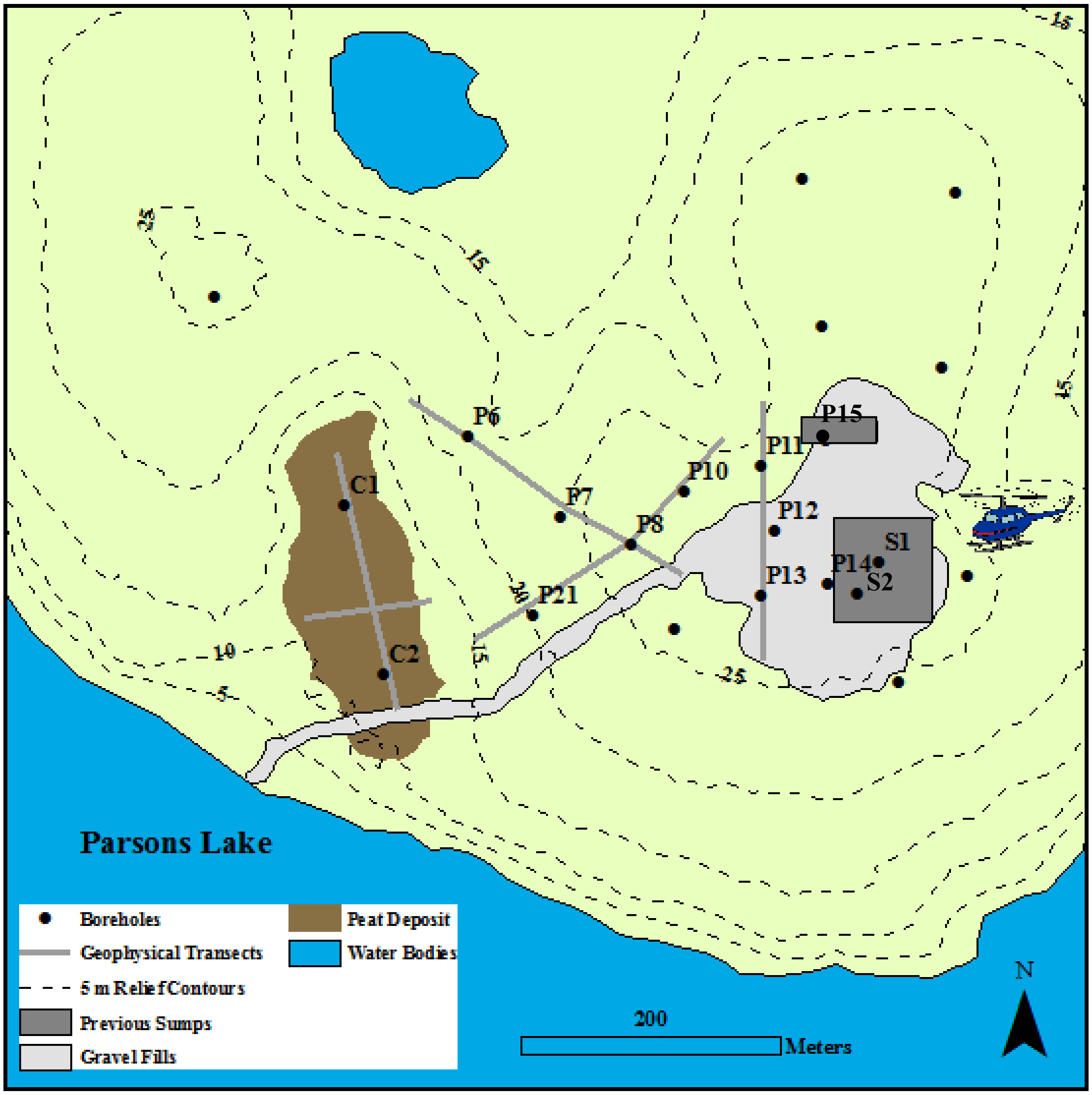

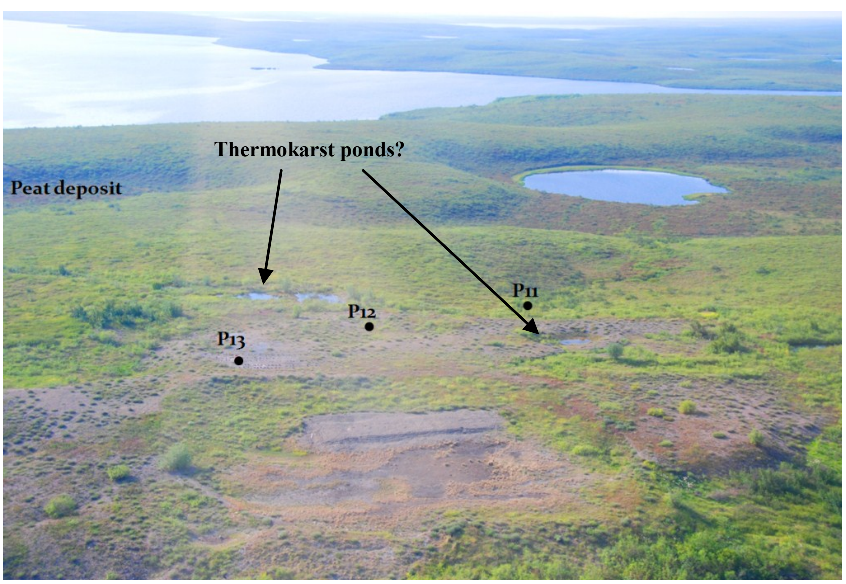

Figure 4.3 (top). Study site map created in ArcGIS. The contour lines and former drilling sumps were generated by digitizing a topographic map from Kiggiak-EBA's geotechnical assessment report (2004). The gravel fill and peat deposit areas were estimated using a georeferenced aerial photo.

Figure 4.4 (left). Aerial photograph of the study site taken in July 2009. The view is from the front of the helicopter icon shown in Figure 4. The photograph's saturation settings were adjusted to enhance colour differences between different terrain types.

4.3 THERMAL MODELLING

4.3.1 Site Selection

With the exceptions of P11, P12, and P13, thermal models were constructed at all the borehole locations that intersected geophysical surveys (Figure 4.3). These three boreholes were not modelled due to recent ground cover changes and the potential existence of contaminants in the near surface. In the 1970's, gravel pads (Figure 4.4) were constructed at these sites for transportation purposes. Furthermore, they are within 50 metres of previous drilling sumps, and on a regional level, studies suggest these structures are degrading (Kanigan and Kokelj, 2010). Refer to Table 4.1 for a general description of the modelled sites.

Table 4.1. General Description of Modelled Sites

Borehole		Near-surface characterization	
#	Depth (m)	Soil type	Presence of massive ice?
P6	20.60	mineral	yes
P7	21.34	mineral	yes
P8	21.34	mineral	yes
P10	22.90	mineral	yes
P21	24.20	mineral	no
C1	13.72	peat	yes
C2	21.34	peat	yes

4.3.2 Model Parameterization

4.3.2.1 Material Properties

Material properties were parameterized to a depth of 50 m at all sites. Since borehole depths ranged from 13.72 - 22.90 m, a generic material was established to occupy the region between a borehole's maximum extent and a depth of 50 m. The number of soil layers in each model is a function of the number of sediment and moisture content changes observed in the borehole logs. For the TONE models, a new layer was set at every depth characterized by a change in soil description or a 5% shift in volumetric moisture content (VMC) from the previous layer. Since the logs contain gravimetric moisture contents (GMC), the data was converted to volumetric form using Eq. 4.1, where ρ_{ice} = 0.917 g/cm^3, $\rho_{dry\ soil\ (mineral)}$ = 1.460 g/cm^3 (Kezdi, 1974), and $\rho_{dry\ soil\ (peat)}$ = 0.300 g/cm^3 (Williams and Smith, 1989).

$$VMC = \left(\frac{\frac{GMC/100}{\rho_{ice}}}{\frac{GMC/100}{\rho_{ice}} + \frac{1}{\rho_{dry\ soil}}} \right) \text{, where} \qquad [4.1]$$

Unfrozen water content:

To determine whether or not a given layer was unsaturated, saturated, or supersaturated theoretical porosities for the observed soil types (Table 4.2) were used and compared to the volumetric moisture contents. The porosities for mineral and peat soils were taken from Kezdi (1974) and Williams and Smith (1989), respectively.

Table 4.2. Physical Properties of Soil Types

Soil Type	Porosity (θ) (%)	Quartz (%)	Particle k (W m^{-1} K^{-1})	VMC (%)
Clay	50.0	20	2.62	
Silty Clay	47.0	20	2.62	
Silt	44.0	20	2.62	
Silty Sand	41.0	50	3.92	
Sand	38.0	90	6.73	
Gravel	33.0	90	6.73	
Sandy Gravel	35.5	90	6.73	
Peat	70.0	0	0.25	
Generic	40.0	50	3.92	40

Once the degree of saturation was found, unfrozen water content versus temperature function was created for that layer. Unfrozen water content versus temperature functions for various mineral soils summarized in Andersland and Ladanyi (2004) were used as references to accomplish this task. Each reference function is expressed as a power function of the form $\alpha|T|^{\beta}$, where $|T|$ is the temperature below 0 °C and the parameters α and b are empirically derived constants (Table 4.3). Since unfrozen water content is expressed gravimetrically in Andersland and Ladanyi (2004), the functions were converted to volumetric unfrozen water content (VUWC) versus temperature functions using Eq. 4.1 (Figure 4.5). In addition, VUWC values for peat soils were taken from Kujala et al. (2008). In order to comply with TONE input requirements, it was necessary to express VUWC content as a fraction of the total VMC for a given temperature. With the exception of the peat data, it was assumed that the functions in Figure 4.5 are based on moisture conditions near or at saturation. The strategy for generating unfrozen water content versus temperature functions was dependent on the degree of saturation.

Table 4.3. Unfrozen Water Content Functions

		Constants		
Material	**Location**	**Alpha (α)**	**Beta (β)**	**Source**
Clay	Inuvik	14.5	-0.254	M.W. Smith (1985)
Silty clay	Suffield	11.1	-0.254	M. Smith and Tice (1988)
Silt	Fairbanks	4.8	-0.326	Anderson, Tice, and McKim (1973)
Gravel	Lebanon	2.1	-0.408	M. Smith and Tice (1988)

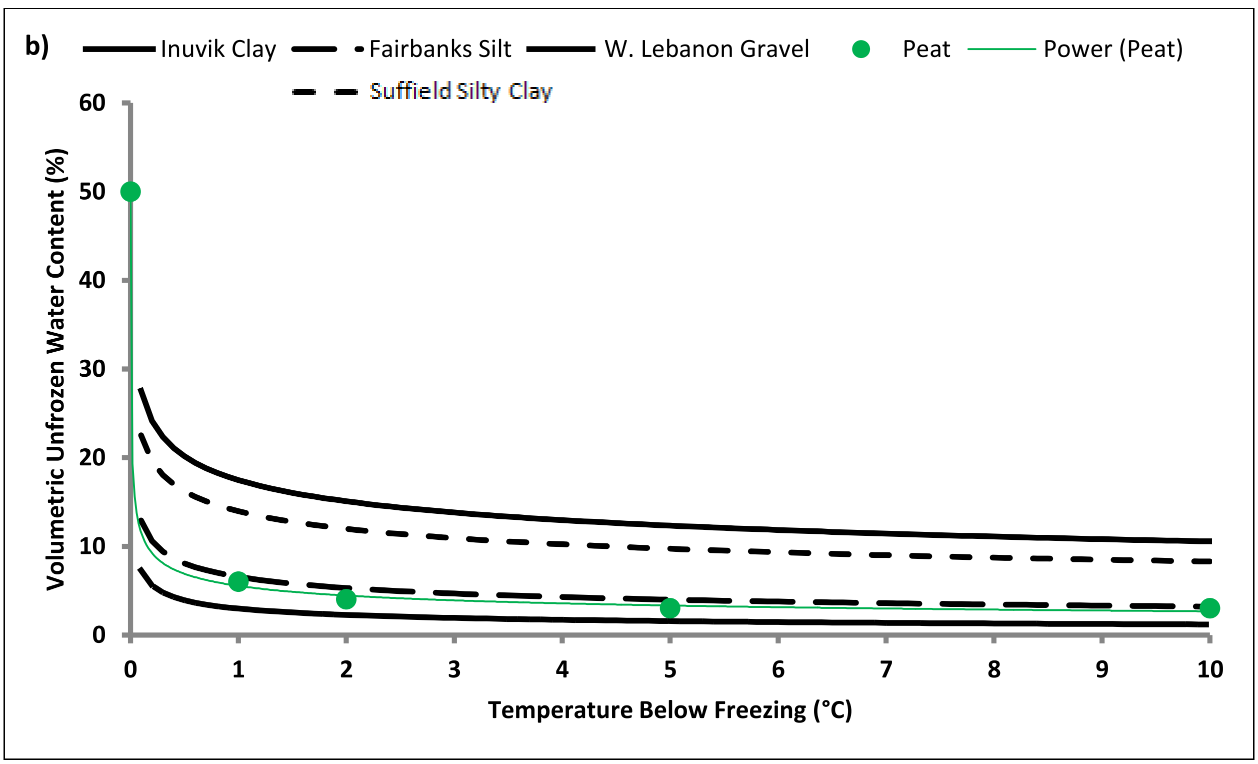

Figure 4.5. Gravimetric unfrozen water content curves presented in Andersland and Ladanyi (2004) are converted to volumetric unfrozen water contents. In addition, data for peat soils (Kujala et al., 2008) is included.

i. Supersaturated condition

The amount of unfrozen water is dependent on temperature, soil type, and the distribution of sediment. Since the functions from Andersland and Ladanyi (2004) are assumed to be at or near saturation, the unfrozen water content/sediment ratio for a given mineral soil at a specific temperature is known. Seeing as the total moisture content for peat is given, the curve in Figure 5 was adjusted to represent a saturated condition. Hence, the concentration of unfrozen water can be determined with Eq. 4.2, where S = the volumetric sediment content, S_{sat} = the sediment content under a saturated condition, and $S_{supersat}$ = the sediment content under the supersaturated condition.

$$VUWC\ (soil, T) = \left(\frac{VUWC\ (soil,T)_{sat}}{S_{sat}}\right) S_{supersat} \quad \text{, where} \qquad [4.2]$$

$$S_{sat} = 1 - \theta$$
$$S_{supersat} = 1 - VMC$$

The distribution of sediment is important, because unfrozen water films develop more easily on concentrated volumes of matter (Torrance and Schellekens, 2006). Since the spatial arrangements of ice and sediment within each layer are not known, it is assumed that sediment is uniformly distributed within the soil matrix if the volumetric ice content equals or exceeds 80% (Couture, personal communication[1]). Under this condition, unfrozen water content is 0% at any temperature below 0 °C.

ii. Unsaturated condition:

The volumetric sediment content (1 - θ) remains constant for any unsaturated condition. As moisture content increases, void space decreases and UWC increases, because more moisture is available to stick to the sediment at a given temperature. Hence, the concentration of unfrozen water can be determined with Eq. 4.3.

$$VUWC\ (soil, T) = \left(\frac{VUWC\ (soil,T)_{sat}}{VMC_{sat}}\right) VMC_{unsat} \qquad [4.3]$$

[1] Dr. Nicole J. Couture, a permafrost scientist at the Geological Survey of Canada, Ottawa, ON

Thermal Conductivity:

For a composite material, the thermal properties of all substances must be considered when calculating a geometrically weighted thermal conductivity (κ). Since κ at 0 °C is undefined, κ calculations for each layer started at -0.05 °C. In TONE, κ calculated for -0.05 °C was used for all temperatures > -0.05 °C. Subsequently, thermal conductivities were calculated for all temperatures between -0.1 °C and -10 °C at intervals of 0.1 °C. In TONE, κ calculated for -10 °C was used for all temperatures < -10 °C. Thermal conductivity for a given layer at a specific temperature is a function of the particle conductivity, as well as the fractions of air, ice, sediment, and UWC (estimated for each layer as previously shown in this section). The particle conductivities (Table 2) were calculated as a function of soil type and quartz content (Johansen, 1975). Similar to UWC estimates, κ calculations are dependent on the degree of saturation.

i. Supersaturated condition:

The physical materials required to calculate κ are VMC, VSC, and VUWC, which is a function of soil type, temperature, and VSC. Hence, κ can be determined from Eq. 4.4 (Johansen, 1975), where k_p = particle conductivity (refer to Table 2), k_{ice} = 2.24 $Wm^{-1}K^{-1}$, and k_{water} = 0.56 $Wm^{-1}K^{-1}$.

$$k_{supersat}(soil, T) = e^{\alpha}, where \qquad [4.4]$$

$$\alpha = (1 - VMC)\ln(k_p) + (VMC - VUWC(soil, T, S_{sat})\ln(k_{ice}) + VUWC(soil, T, S_{sat})\ln(k_w)$$

ii. Unsaturated condition:

In this case, κ is a function of the degree of saturation, κ for dry soil, and the saturated κ (VMC = θ). The dry soil κ can be estimated with the dry soil density ($\rho_{dry\ soil}$) using Eq. 4.5 from Johansen (1975).

$$k_{unsat}(soil, T) = (k_{sat} - k_{dry\ soil})\left(\frac{VMC}{\theta}\right) + k_{dry\ soil}, where \qquad [4.5]$$

$$k_{dry\ soil} = \frac{0.135\rho_{dry\ soil} + 64.7}{2700 - 0.947\rho_{dry\ soil}}$$

$$k_{sat}(soil,T) = e^{\alpha} \ and$$

$$\alpha = (1-\theta)\ln(k_p) + (\theta - VUWC(soil,T,S_{sat})\ln(k_{ice}) + VUWC(soil,T,S_{sat})\ln(k_w)$$

Heat Capacity:

When the mass heat capacity is multiplied by the material's density (ρ), the volumetric heat capacity, C (J m^{-3} K^{-1}), is obtained. Since soil contains fractions of multiple materials, a linearly weighted average value for heat capacity must be used. Since C for air is so low (≈ 1.21 J m^{-3} K^{-1}), it is neglected in Eq. 4.6 and Eq. 4.8 for frozen heat capacity (FHC), as well as Eq. 4.7 and Eq. 4.9 unfrozen heat capacity (UHC). In these equations, $\rho_{ice}C_{ice}$ = 1970 KJm^{-3}K, $\rho_{water}C_{water}$ = 4220 KJm^{-3}K, $\rho_{mineral\ soil}C_{mineral\ soil}$ = 2120 KJm^{-3}K, and $\rho_{peat\ soil}C_{peat\ soil}$ = 2496 KJ m^{-3}K.

i. Supersaturated condition:

$$FHC = (\rho_{ice}c_{ice})VMC + (\rho_{soil}c_{soil})(1 - VMC) \quad [4.6]$$

$$UHC = (\rho_{water}c_{water})VMC + (\rho_{soil}c_{soil})(1 - VMC), where \quad [4.7]$$

ii. Unsaturated condition:

$$FHC = (\rho_{ice}c_{ice})VMC + (\rho_{soil}c_{soil})(1 - \theta) \quad [4.8]$$

$$UHC = (\rho_{water}c_{water})VMC + (\rho_{soil}c_{soil})(1 - \theta) \quad [4.9]$$

Since UWC is temperature-dependent, near-surface heat storage changes are dominated by latent heat effects, especially within a few degrees below 0 °C (Williams and Smith, 1989). When latent heat effects are considered, materials are described as having an apparent heat capacity. Given that the TONE model accounts for latent heat effects, only the FHC and UHC must be specified.

4.3.2.2 Boundary Conditions

Simulations assumed that the initial ground thermal condition was in equilibrium with the normal climate of 1971-2000 from Inuvik. Air temperature was modelled as a sine-wave to match values for freezing-degree days (FDD) and thawing-degree days (TDD). More specifically, the area above the air temperature curve for values < 0 °C was equal to FDD and the area under the same curve for values > 0 °C was equal to TDD. Once the surface temperature dropped below 0 °C, snow cover was initiated and accumulated with the square root of time. The annual maximum snow cover depth is based on the climate normal data and occurs just before the onset of ablation, which is controlled by thawing-degree days at a rate of 1.5 kg m^{-2} per degree-day (Riseborough and Smith, 1993). The snow density is assumed to be 220 kg m^{-3} based on regional studies (Brown et al., 2001). During FDD periods, TONE automatically calculates the ground surface temperature (GST) based on snow depth. When no snow is present, TONE uses the air temperature and a regional N-factor of 0.8 (Duschesne[2], personal communication) to calculate GST values. Due to the ramping of snow cover, simulations ran from mid-year to mid-year (starting date on July 1st).

In order to reach periodic equilibrium, the one-dimensional models were run with the normal climate data for hundreds of cycles. For each model run, the thermal outputs were compared to the result of the previous cycle. Once the difference reached a pre-defined level of tolerance (< 0.001 °C), the sequence was terminated. The final output became the initial condition for 2001-2010. During this timeframe, air temperature sine waves and maximum snow cover depths were generated each year. Hence, the length of the snow cover season was adjusted on an annual basis. The final year of any simulation used daily meteorological inputs (i.e. air temperature and depth of snow cover) from the Inuvik airport weather station.

A geothermal heat was used as the lower boundary condition for all simulations. According to Majorowicz and Grasby (2010), the geothermal heat flux in the Western Canadian Arctic is between 50-60 mW m^{-2}. Hence, a value of 55 mW m^{-2}, which can also be expressed as 4.75 KJ m^{-2} day^{-1}, was used.

[2] Caroline Duchesne, a physical scientist at the Geological Survey of Canada, Ottawa, ON

4.3.2.3 Climate Change Scenarios

Climate normal statistics show that mean annual air temperatures (MAAT) in the Mackenzie Valley have increased by 1 °C over the last three decades, which is one of the fastest rates in the polar regions (Serreze et al., 2000). Burn et al. (2004) summarize the results of seven global climate models (GCMs) designed to simulate the effects of climate change under varying scenarios of greenhouse gas emissions during 2010-2039, 2040-2069, and 2070-2099. All GCMs resolve the Mackenzie Valley into two sectors, one south of Fort Good Hope and one north of Fort Good Hope. For thermal modelling purposes, only the 2010-2069 timeframe is considered. When the outputs from all GCMs are grouped together, the median MAAT projections show increases in 1.6 °C and 3.6 °C for the 2010-2039 and 2040-2069 periods respectively.

These MAAT projections were used to predict active layer thickness changes at Parsons Lake. In addition, no change in the annual maximum snow depth was assumed. As a baseline for the climate change scenarios, a sine wave was fit to the average air temperatures from the 2000-2010 Inuvik climate data. Although annual maximum snow depths were consistent with the average of 2000-2010 for the duration of the simulations, MAAT increases adjusted the length of the snow seasons accordingly.

4.4 RESULTS

4.4.1 Model Accuracy

Daily thermal outputs were produced and compared with observed data. The thermal models for September 2004 perform well for all the boreholes characterized by near-surface mineral soil (Figures 4.6a-4.6e). It was found that the error between the observed and predicted temperatures oscillate between -1.0 °C and 1.0 °C for all depths. The model accuracies for March and April are relatively poor due to the spatial and temporal heterogeneity of snow cover. In general, the error decreases from the surface until the depth of significant seasonal temperature variation (≈ 6 m). For example, at P7, the error can be as large as 5.0 °C half a metre below the surface and less than 0.5 °C at a depth of 6 m or greater. Despite the results, there is confidence in the total annual snow accumulation estimates. Otherwise, the mean annual ground surface temperatures would be inaccurate, and as a consequence, the errors for the September models would be greater. Given that the models are one-dimensional and that there is no directional bias for the magnitude and sign of the errors, lateral heat flows for the P6-P7-P8 and P21-P8-P10 transects are minimal. Hence, the models are suitable for projecting active layer changes. Furthermore, these changes can be combined with 2D geophysical surveys to describe relative terrain sensitivity to climate change.

For the peat deposit, the accuracies of the models for September are poor compared to the mineral soils. The error increases from the surface to the depth of significant seasonal temperature variation (≈ 6 m). At or below this depth, errors fluctuate from 2.0 to 3.0 °C and from 1.0 to 2.0 °C for C1 and C2, respectively. In April, the error half a metre below the surface ranges from 4.0 to 5.0 °C for both cores. At 6 m, the error is 2.0 °C for C1 and 1.5 °C for C2. At C1, the error increases from 2.0 °C at 6 m to just below 3.0 °C at 10 m. This is unique, because for all other boreholes, the error either decreases or remains constant from the depth of significant annual temperature variation downwards. Irrespective of the overall inaccuracies for the peat site, the models were still used to project active layer changes so as to demonstrate the buffering capacity of organic soils to climate warming.

4.4.2 Maximum Active Layer Thickness Projections

Maximum active layer thicknesses (MALT) for boreholes P6, P8, P10, and C2 are plotted as a function of time in Figure 4.7. These four sites are chosen for illustration, because results for the remaining boreholes require follow-up analyses. The MALT for P6 increases from 0.73 m in 2011 to 1.10 m in 2040, which corresponds to a growth rate of 1.28 cm/year. In 2040, the rate of MALT development increases, because the mean annual ground surface temperature's (MAGST) rate of change accelerates. From 2040-2063, the MALT increases from 1.10 m to 1.92 m (3.57 cm/yr). From 2063-2070, the MALT decreases from 1.92 m to 1.81 m (-1.57 cm/yr). Results beyond 2058 are inaccurate, because the maximum thaw depth encounters massive ground ice at a depth of 1.8 m. TONE does not account for geomorphic changes associated with the melting of excess ice in permafrost.

The MALT for P10 increases from 1.36 m in 2011 to 1.62 m in 2040 (0.90 cm/year). From 2040-2070, the MALT increases from 1.62 m to 2.12 m (1.67 cm/year). Since massive ice is not observed until a depth of 2.3 m, no deceleration of MALT versus time similar to P6 is observed. Notice that the rates of change for the MALT from 2011-2040 and 2040-2058 are greater for P6 (1.28 cm/yr; 3.94 cm/yr) compared to P10 (0.90 cm/yr; 1.44 cm/yr). Firstly, this is because massive ice is closer to the surface for P6, and as demonstrated in Figure 4.8a, the thermal diffusivity of the ice is high (0.10 m^2/day). Secondly, P6 contains both silt and silty clay layers near the surface. P10, however, consists of only silty clay above the massive ice. As illustrated in Figures 4.8a and 4.8c, the frozen thermal diffusivities for P6 are relatively high in the near surface (0.06-0.08 m^2/day) compared to P10 (0.04-0.06 m^2/day) for temperatures between 0 °C and -4 °C.

The MALT for P8 increases from 1.18 cm in 2011 to 1.29 m in 2040 (0.38 cm/yr). From the 2040-2070, the MALT increases by only an additional 1 cm. For the entire period, the MALT versus time relationship is best described as a logarithmic function. Although the MAGST increases at an average rate of 0.14 °C per year between 2040 and 2070, its effect is potentially offset by decreasing apparent thermal diffusivity values. Similar to P10, P8 is characterized by silty clay units, which overly massive ground ice encountered at a depth of 1.8 m. Although P8 and P10 have similar frozen thermal diffusivities (Figures 4.8b and 4.8c) for near-surface soils, P8 and P10 have average volumetric moisture contents of 37% and 28%, respectively. Furthermore, VMC for the soil units increases with depth for P8 and decreases with depth for P10. Hence, the quantities of latent heat absorbed during the thaw season increases with time for P8. Thus, very low apparent thermal diffusivities could be preventing further growth in the MALT.

The MALT for C2 increases from 0.70 m in 2011 to 0.78 m in 2040 (0.28 cm/yr). From 2040-2070, the MALT increases from 0.78 m to 1.02 m (0.80 cm/yr). Similar to P8, C2 is characterized by relatively low near-surface frozen thermal diffusivities (Figures 4.8b and 4.8d), and because of high moisture contents, strong latent heat effects. The MALT growth rate, however, does not plateau. This is probably because the model's initial active layer thickness in 2011 is relatively thin, and as a result, it is more susceptible to MAGST changes.

4.4.3 Geophysical Surveys

In a related study (Manuscript 1), the data quality of the CCR surveys was analysed through depth of investigation (DOI) tests introduced by Oldenburg and Li (1999). This is an empirical method that compares two inversions of the dataset using different reference resistivities for the model cells. The DOI approaches a value of zero where the two inversions generate similar values. In these zones, the cell resistivity is well constrained by the data. In areas where the model cells contain minimal information about the cell resistivity, the DOI approaches a value of 1. Oldenburg and Li (1999) suggest that a reasonable cautious cut-off value is 0.1. By employing these tests, optimal values for the inversions of electrical data were found. When CCR was used in conjunction with GPR cross-sections, it was found that the resistivity of massive ground ice ranged from 25 000 to 40 000 Ω, and that the resistivity of ice-rich peat oscillated between 6000 and 9000 Ω in winter when unfrozen water content was minimal or absent in the near surface.

For the two undisturbed transects intersecting boreholes categorized by near-surface mineral soil, massive ground ice bodies were successfully mapped. Mineral transect 1 (Figure 4.9) illustrates two icy sediment zones enclosed by massive ground ice. Resistivities for the icy sediments range between 2800 and 6200 Ω, and as shown in the GPR cross-section, these areas are correlated with increased scattering of the GPR signal. Hence, these regions should not be as susceptible to the subsidence MALT scenario shown in Figure 4.7. Depending on the texture and moisture contents of the materials underlying and overlying the active layer and massive ground ice bodies, respectively, any one of the scenarios presented for the mineral soils (Figure 4.7) is possible. The different MALT developments are also applicable to segments of the P21-P10 profile (Figure 4.10) where massive ground ice is encountered. The exception is found between horizontal distances of 0 and 90 m. Borehole P21, which is situated at a horizontal position of 65 m, does not contain massive ice until a depth of 16. m. Instead, fine-grained materials in the upper 2 m cover icy gravelly sand deposits. At boreholes P8 and P10, however, fine-grained soils overly massive ground ice structures, which are encountered at 1.8 and 2.3 m, respectively. It was found that CCR does not map a clear lateral transition between massive ground ice and coarse-grained materials. When combined with GPR, however, the icy gravelly sand anomaly can be mapped (Figure 4.10). Here, the subsidence scenario is not applicable, but given that sand

and gravel have higher thermal diffusivities than ice (Williams and Smith, 1989), MALT growth should occur at a faster rate than the adjacent terrain. As a consequence, this zone could provide an efficient conduit for meltwater generated from adjacent melting of ground ice.

The P13-P11 profile starts on the edge of a gravel pad and terminates on undisturbed terrain (Figures 4.10a and 4.10b). Since portions of the profile are located only 60 m to the west of former drilling sumps (Figure 4.3), this profile is more susceptible to contamination resulting from sump leakage than any of the other surveyed sites. Between 35-85 m, as well as between 140-165 m, two pockets of very low resistivity (190-600 Ω) are observed. Depending on the type of DOI test performed, Figures 4.11a and 4.11b suggest that either a portion or virtually none of the anomaly intersecting P13 is an artifact generated by the inversion. Hence, the highly conductive structure is real, and can up to 50 m long and 5 m thick. On the other hand, the anomaly to the left of P11 is considered unreliable irrespective of the type of DOI test executed.

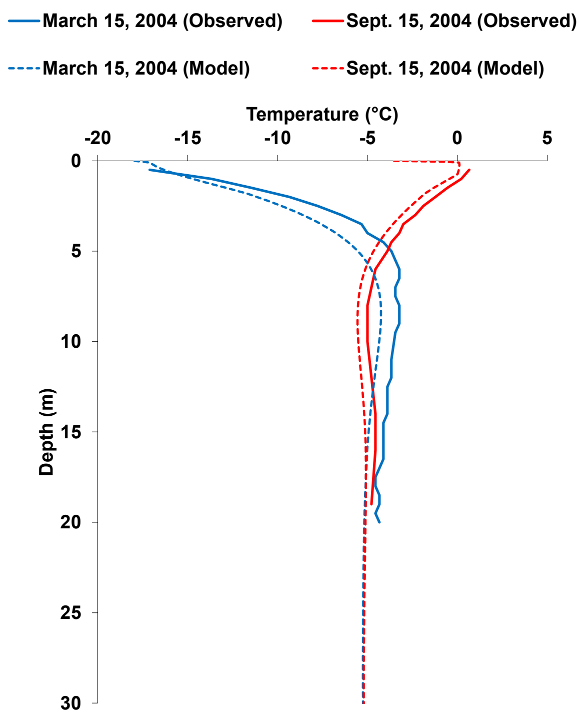

Figure 4.6a (borehole P6)

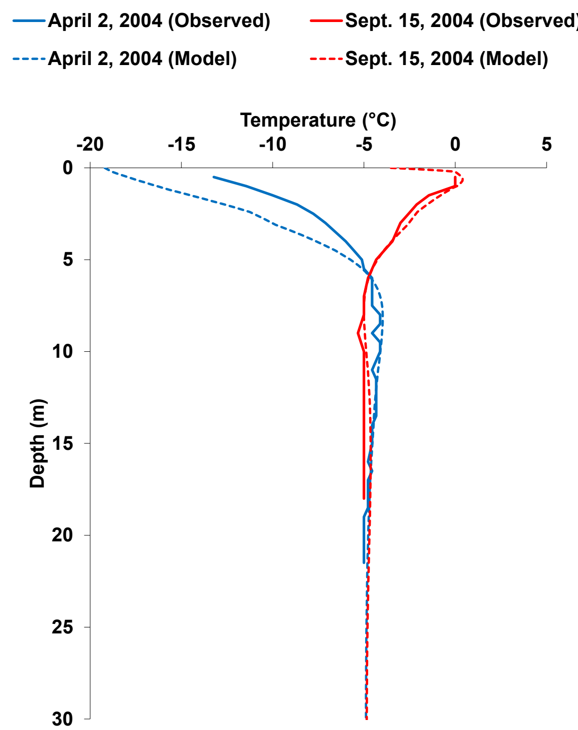

Figure 4.6b (borehole P7)

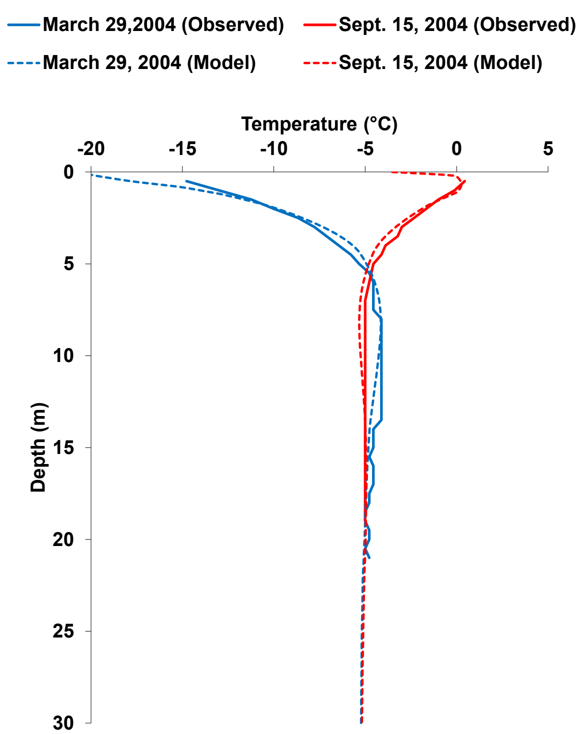

Figure 4.6c (borehole P8)

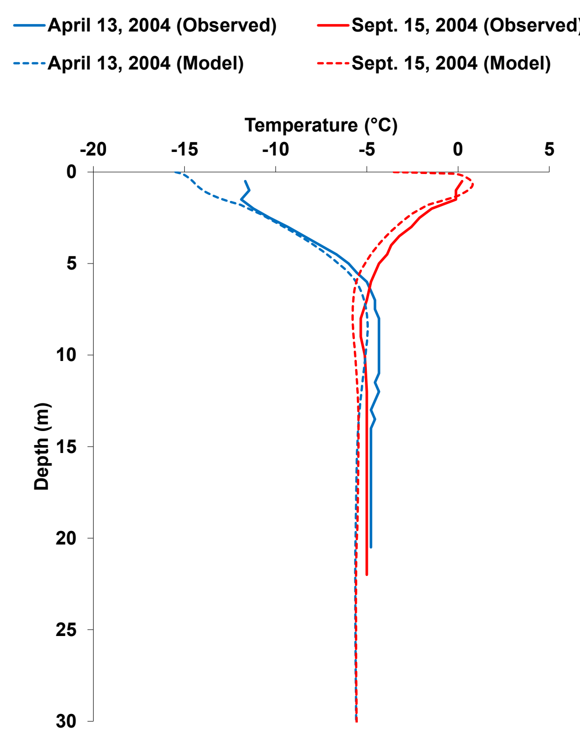

Figure 4.6d (borehole P10)

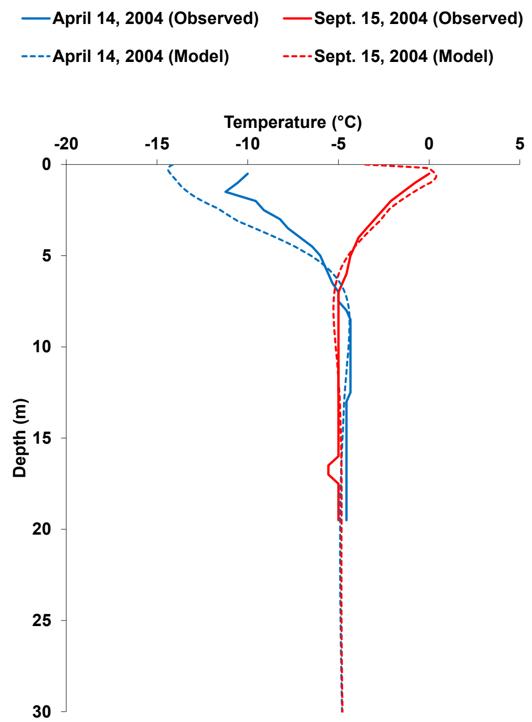

Figure 4.6e (borehole P21)

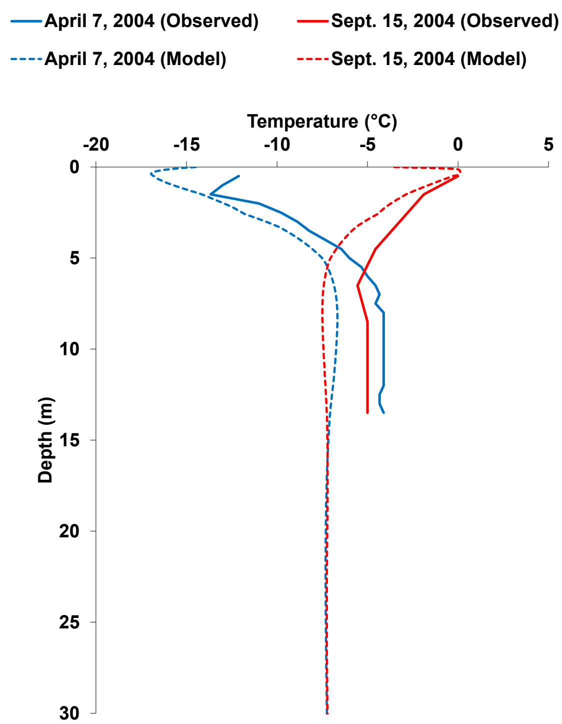

Figure 4.6f (borehole C1)

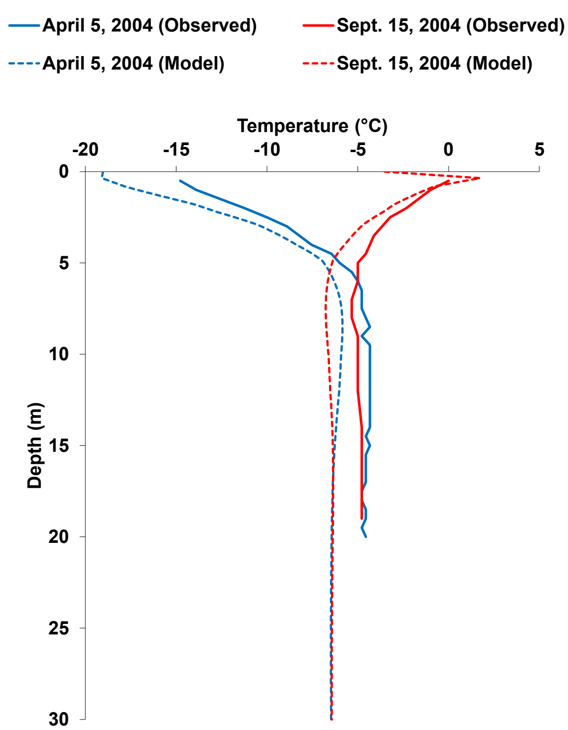

Figure 4.6g (borehole C2)

Figure 4.6. During the ConocoPhillips Canada (CPC) winter drilling program in 2004, ground temperature measurements were recorded at boreholes in March, April, and September of that year. For some of these cores, 1D thermal models were constructed with TONE. The modelling results are compared with the observed data.

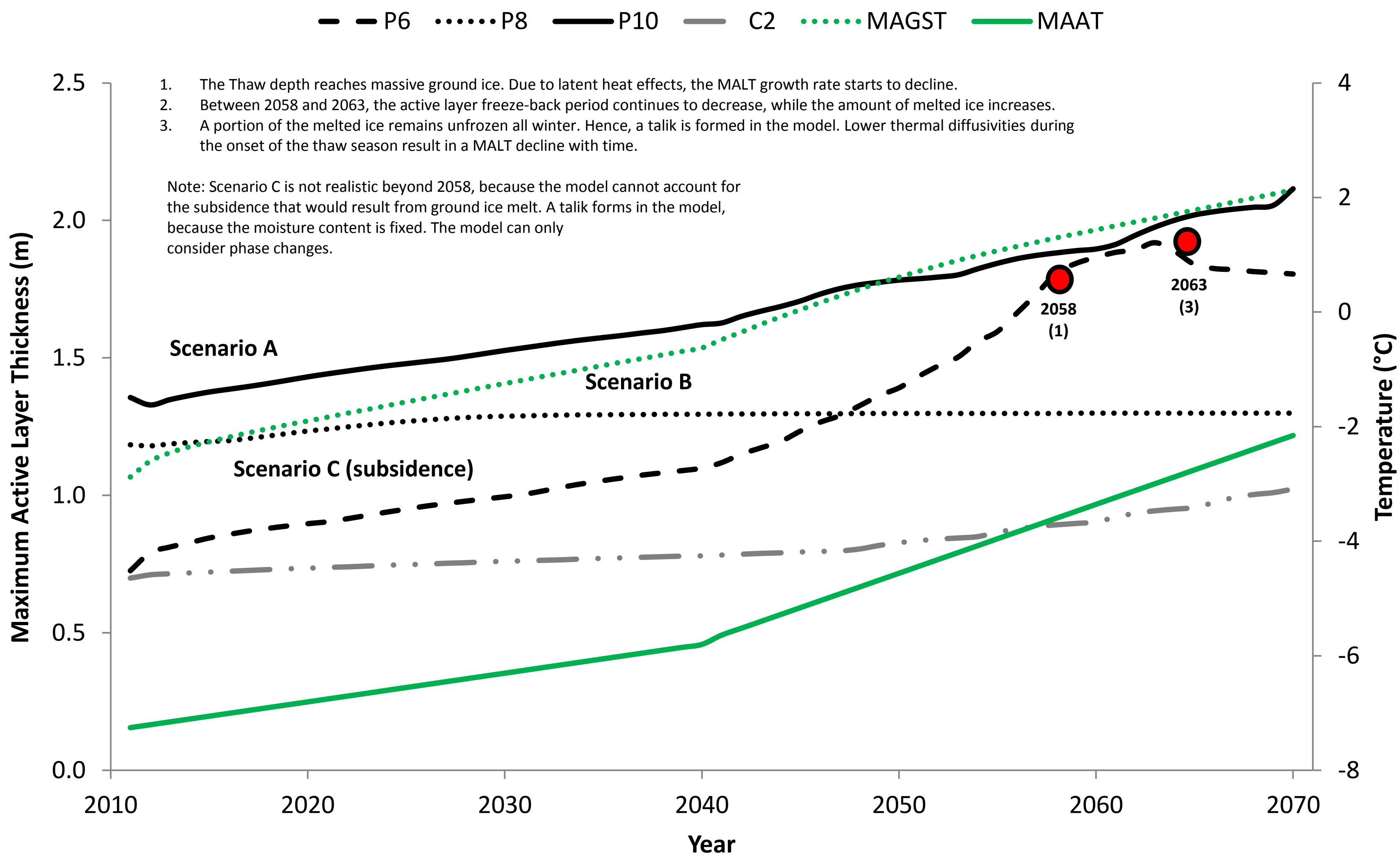

Figure 4.7. Using climate change scenarios for the Mackenzie Delta and Mackenzie Valley (Burn et al., 2004), maximum active layer thickness (MALT) projections for multiple undisturbed boreholes are shown. For cores characterized by near-surface mineral soils (P6, P8, and P10), three scenarios resulting from climate warming are presented. In scenario A, the MALT for silty clays with relatively low volumetric moisture contents (< 30%) increase linearly with time (0.90 cm/yr from 2011-2040; 1.44 cm/yr from 2040-2070). In scenario B, the MALT for silty clays with relatively high moisture contents (≈ 50%) increases for a brief period and then stabilizes (0.38 cm/yr from 2011-2040, 1 cm from 2040-2070). In scenario C, a talik is formed by the model as explained on the diagram.

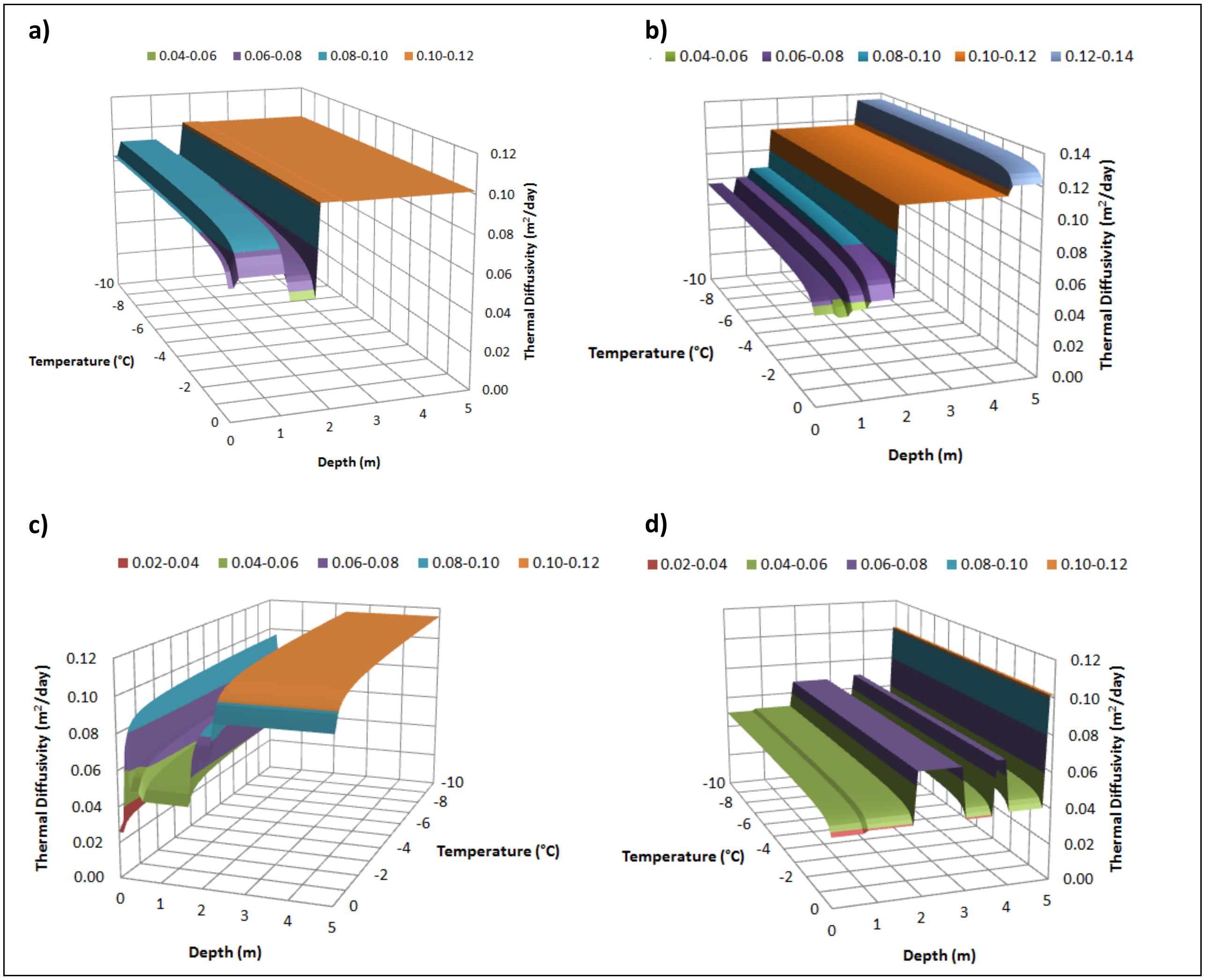

Figure 4.8. Frozen thermal diffusivities as a function of depth and temperature for P6 (a), P8 (b), P10 (c), and C2 (d). Note that apparent thermal heat capacities are not included in the calculations for this diagram. Hence, these values represent the frozen thermal diffusivities of the materials in situations where phase changes are not occurring. Refer to Chapter 2.3 for a discussion on ground thermal regimes.

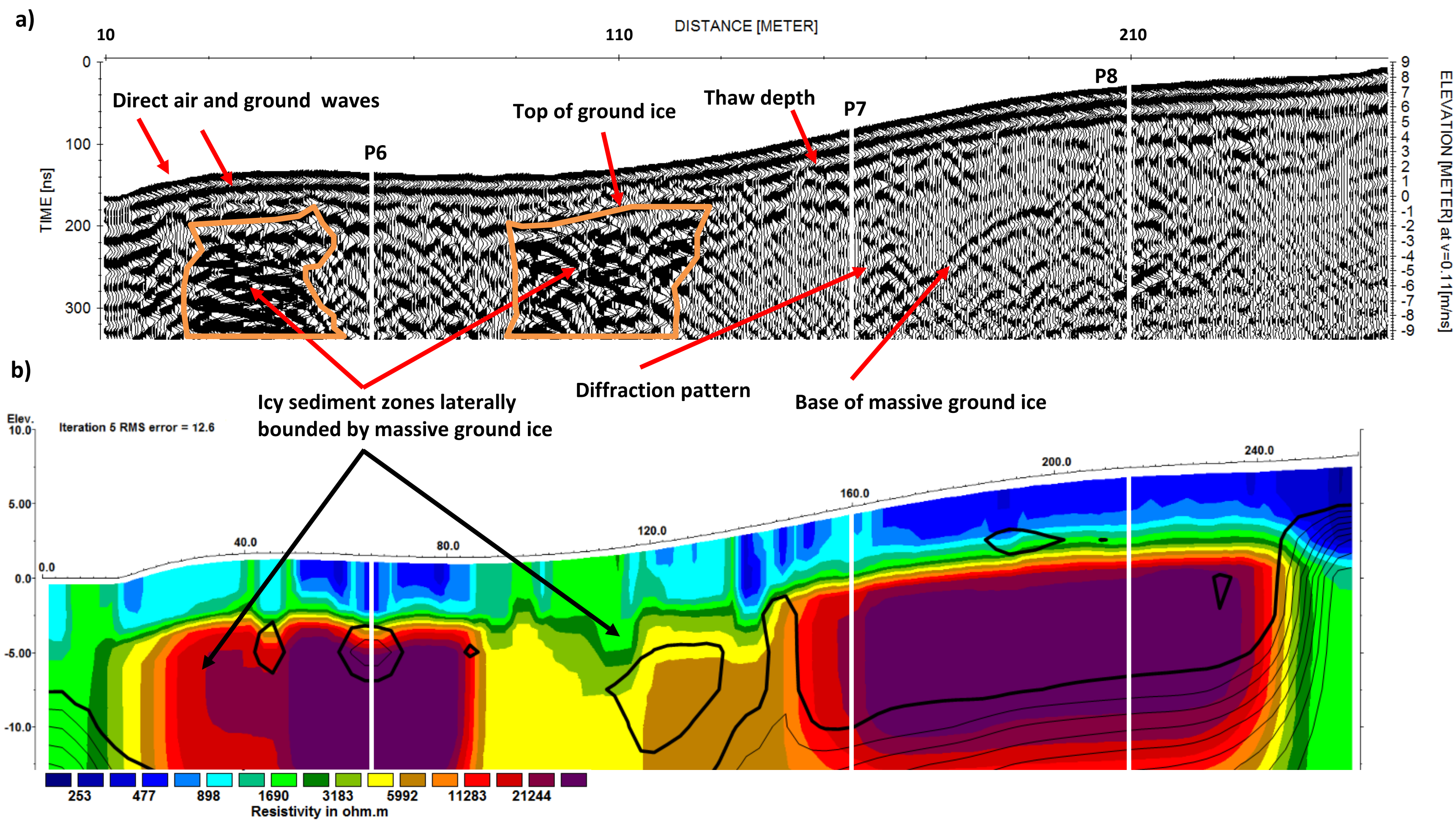

Figure 4.9. The vertical exaggeration of both images is 2.93 and all positional units are in metres. (a) 50 MHz GPR profile conducted on July 20th, 2010. The two areas of intense signal scattering are interpreted as icy sediments. The icy sediments are surrounded by massive ground ice, which is characterized by homogeneous zones with little or no reflection events (black lines). (b) CCR profile carried out on July 21st, 2010 with DOI tests superimposed upon the resistivity results. The DOI contour interval is 0.1 with smaller values being closer to the surface. All models cells above the 0.1 contour (thick black line) are considered reliable, whereas model cells below the 0.1 contour are not. Resistivity for massive ice ranges from 25 000 - 40 000 Ω, while it oscillates between 2800 and 6200 Ω for icy sediments. In (a), the icy sediments are outlined. For these sections, scenario C (subsidence by 2058) presented in Figure 4.7 is not expected to occur.

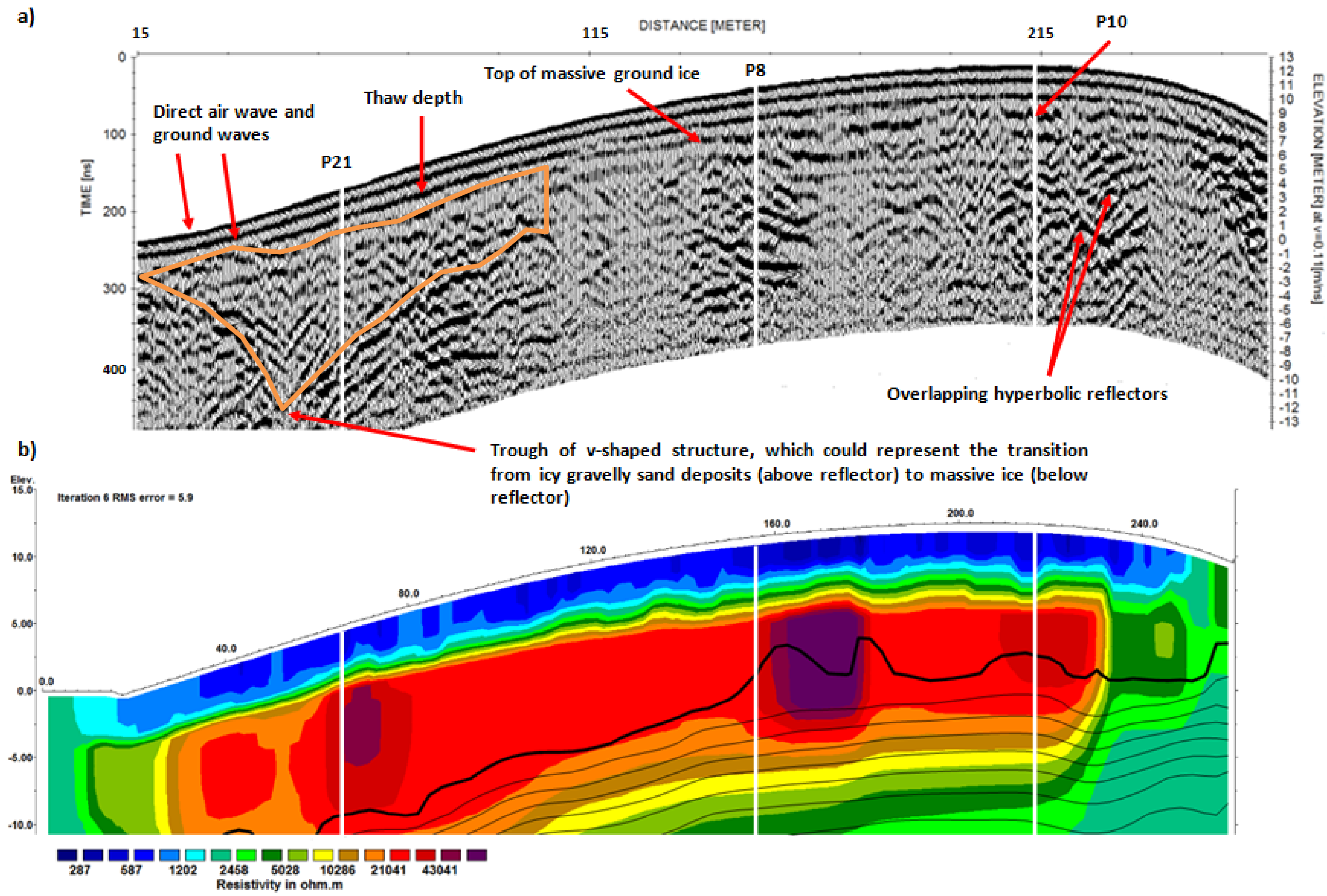

Figure 4.10. The vertical exaggeration of both cross-sections is 2.93 and all positional units are in metres. (a) 50 MHz GPR profile conducted on July 21st, 2010, and (b) CCR profile carried out on July 22nd, 2010. The DOI contour interval is 0.1 with smaller values being closer to the surface. All models cells above the 0.1 contour (thick black line) are considered reliable, whereas model cells below the 0.1 contour are not. CCR does not map a clear near-surface lateral transition from massive ice (identified at P8 and P10) to coarse-grained materials (identified at P21), but when combined with the GPR survey, the icy gravelly sand deposit can be mapped. For this section, scenario C (subsidence by 2058) shown in Figure 4.7 is not expected to occur.

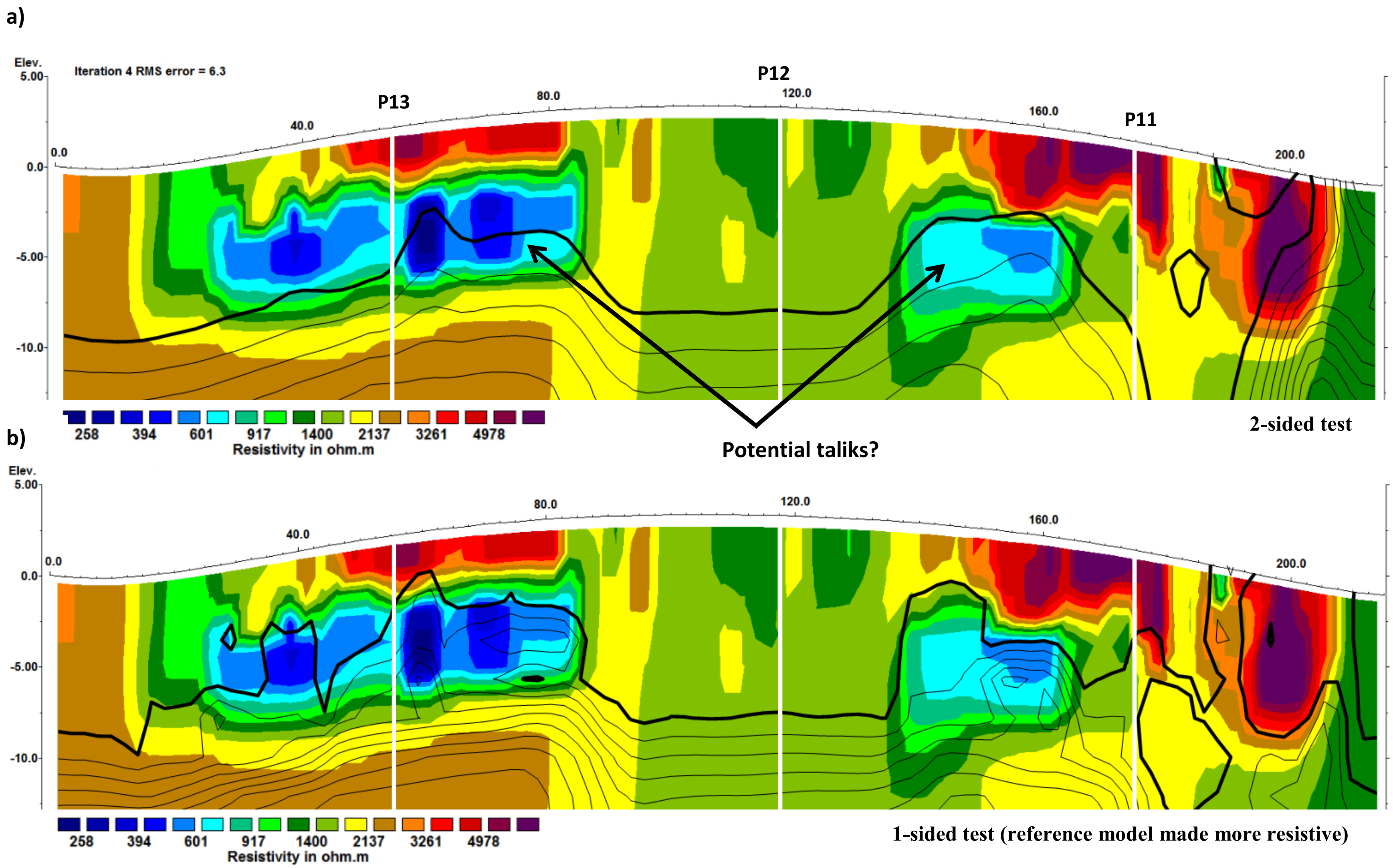

Figure 4.11. The vertical exaggeration of both cross-sections is 2.93 and all positional units are in metres. The DOI contour interval is 0.1 with smaller values being closer to the surface. All models cells above the 0.1 contour (thick black line) are considered reliable, whereas model cells below the 0.1 contour are not. (a) The DOI values were calculated by comparing two inversions of the dataset. One inversion was assigned a reference resistivity of 1/10[th] the original value and the other was assigned a reference resistivity of 10 times the original value (2-sided test). This method works best when both resistive and conductive targets are being mapped (Oldenburg and Li, 1999). (b) In this case, an inversion with a default reference resistivity and an inversion with a reference resistivity of 10 times the original value were compared (1-sided test). This strategy works well when the features of interest are conductive (Oldenburg and Li, 1999).

4.5 DISCUSSION

4.5.1 Thermokarst in Anthropogenically Undisturbed Areas

Simulations for P6 show that the active layer penetrates massive ice in 2058 and since TONE cannot accommodate subsidence, a talik forms in the model by 2064. Between 2058 and 2064, the active layer increases by 12 cm (2 cm/yr). This is approximately 50% of the MALT increase projected between 2040-2058, because latent heat effects are more dominant. Since the projected MALT continues to increase after 2058, the total volume of melted ice freezes again during the winter. Over time, the amount of liquid water generated during the thaw season increases and the length of the active layer freeze-back period shortens. As a consequence, there is a point in time when not all the water transforms back to ice, and this occurs between 2063 and 2064. Since a portion of the melted ice remains unfrozen for the entire winter, the thermal diffusivity of this layer is much lower upon the onset of the thaw season than it was in the previous summer. As a consequence, the energy required to melt the ice near the surface is transported downwards at a slower rate. Thus, the MALT could reach the top of the talik, but will not extend beyond the base of the talik. This is why the models show MALT decreasing at a rate of 1.57 cm/yr from 2064 to 2070.

At P8, the active layer propagates into a silty clay layer having a volumetric moisture content of 54%. Instead of forming a talik, the MALT stabilizes and increases by only 1 cm from 2040-2070. This could be because the energy used to melt the ice is not conducted away from the thawing front at a sufficiently fast rate. As shown in Figure 4.8, the frozen thermal diffusivity of massive ice can be more than double that of ice-rich silty clay at temperatures approaching 0 °C. At P8, the thawed portion of the ice-rich silty clay is underlain by 50 cm of the same materials before massive ice is encountered.

As illustrated in Figure 4.7, the projected increase for the MALT does not slow down (e.g. borehole P10) if the top of massive ice is located at a deep enough position (2.3 m for P10 compared to 1.8 m for P6). Hence, areas with relatively shallow depths to the top of massive ground ice are bounded by materials that could experience a faster MALT increase. This, in turn, should accelerate permafrost degradation by producing conduits for meltwater generated by thermokarst. This effect could be even more pronounced in areas where near-surface massive ice is laterally bounded by sand and gravel deposits (Figure 4.10).

4.5.2 Thermokarst in Anthropogenically Disturbed Areas

There is reason to suggest that the anomalously low resistive pockets observed on the P13-P11 profile are the result of taliks. Although the resistivity of unfrozen materials in permafrost areas have been shown to be less than 1000 Ω (e.g. Fortier et al. 2008), it is unlikely that the talik is 5 m thick. Logs for this borehole show that massive ice is encountered at a depth of 1.3 m, and it is overlain by silt and silty clay units between 0.3 and 1.3 m depths, as well as gravel in the upper 30 cm of the subsurface. Results in Kiggiak-EBA's geotechnical assessment report presented an active layer greater than 1.3 m in September 2004, and thus, extending to the massive ice. The evidence in favour of a talik is supported by observed temperatures for March 14th, 2004, which approach 0 °C (Figure 12). For example, the temperature of the ice was -0.5 °C at a depth of 2.5 m. As a result, one might suspect that the unusually low resistivities are due to high concentrations of unfrozen water within permafrost. Since the average volumetric ice content exceeds 80%, however, the occurrence of unfrozen water films on soil particles is unlikely. For example, assuming that the soil particles in the ice are clumped together, the maximum VUWC estimated for any portion of the massive ice on March 14th, 2004 is 4%. This estimate is based on the calculations shown in section 4.2.1. Since the permafrost probe measurements revealed that the active layer extended into the massive ice in the summer of 2004, some of the ice must have melted. It is conceivable that a similar situation occurred in the summer of 2003, and thus, the high moisture contents could have released an enormous amount of latent heat during active layer freeze-back. This could explain why the temperature was warmest at a depth of 2.5 m in 2004. Although low resistivity values are partially a result of high concentration of dissolved solids in porewater (Associated Geosciences, 2010), it is unlikely that any potential leakage from a previous drilling sump triggered the formation of the talik. Firstly, the salinity of the ice was measured at 2.0 ppt between 2.65 and 2.80 m depths during the CPC winter drilling program (Kiggiak-EBA, 2004), which was similar to undisturbed areas. Secondly, the P13-P11 profile is situated on an equal elevation with the former drilling sumps. Thirdly, the migration of moisture into permafrost is possible, but the hydrologic conductivity can be as slow as 1.67 cm per year (Burn and Michel, 1987).

Since the volume of materials detected by the CCR increases with depth, it is conceivable that the thick nature of the anomaly is a result of deep materials a few to several metres adjacent to the survey line. The thickness of the gravel pad increases from its edge towards the centre. For example, the core from P14 consists of sand and gravels in the upper 4 m of the subsurface, which is underlain by mixtures of silt, clay, sand, and ice. For thermal diffusivities greater or equal to 0.1 m^2/day, Williams and Smith (1989) suggest the active layer can exceed four metres. Therefore, it is possible that deeper active layers and higher concentrations of unfrozen water below the permafrost table a few to several metres adjacent to the survey line exaggerated the thickness of the anomaly in Figures 11a and 11b. Note that since the logs from March 2004 did not reveal a layer of unfrozen ground, the formation of any talik occurred between 2004 and 2010. Since shallow temperatures for P13 are very close to 0 °C in March 2004 (Figure 4.12), only a slight change in the surface energy balance (e.g deeper snow cover, warmer air temperatures) would have been required to bring the near-surface massive ice to its melting point. Given that no terrain disturbance was observed in at P13 in July 2009 or March 2010, the geophysical surveys likely represent thawing permafrost on the verge of collapse. Nearby ponds shown in Figure 4.4 could represent areas that have already undergone thermokarst subsidence.

4.5.3 Model Parameterization

Based on the active layer projections, it is clear that the MALT growth rate is very sensitive to minor fluctuations in the thermal diffusivity and moisture contents of the soils above massive ice. Although the geophysical results can indicate where talik formation and subsidence might occur, they cannot determine which of the MALT projections shown in Figure 4.7 is most representative of Parsons Lake. As a result, future fieldwork at Parsons Lake should attempt to acquire more moisture content data for modelling projects. The thermal models were built using moisture contents from cores extracted from Parsons Lake in March 2004. Although values below the maximum thaw depth that occurred between 2004 and 2010 are accurate, moisture contents from the active layer might not be representative of the average conditions throughout the year.

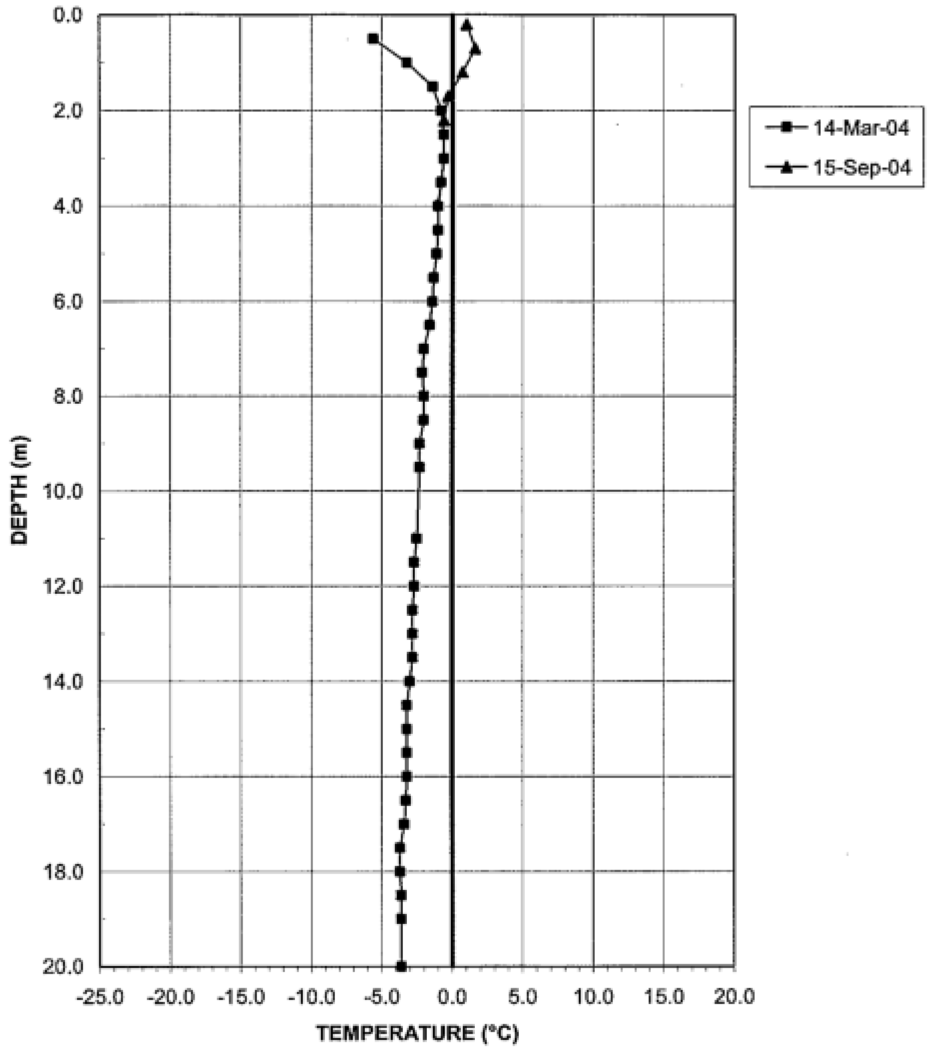

Figure 4.12. Ground temperature profiles for borehole P13 on March 14th, 2004 and September 15th, 2004 (Kiggiak-EBA, 2004)

Future investigations should also attempt to improve the accuracy of the thermal models at the peat site. Problems with the models shown in this paper could include the following:

i. *Inaccurate ground surface temperatures:* Since the peat deposit lies in a depression (Figure 4.4), snow depths from Inuvik might not be attributable to this area. The bowl-shaped zone could trap moving snow, and thus, warm the ground thermal regime. As shown in Figures 4.6f and 4.6g, the modelled temperature curves are colder than the observed data.

ii. *Inaccurate parameterization of materials:* As illustrated in Figures 4.6f and 4.6g, the average error for C1 is 0.6 °C greater than C2. The inaccuracy of C1 is considerably greater than any other model, which is probably due to poorly assigned thermal conductivities below the borehole's maximum extent. Since the depth of this borehole is only 13.9 m, generic material was assigned between this position and a depth of 50.0 m. The high thermal conductivity of the generic material could allow energy from the Earth's interior to escape the subsurface at a rate not representative of real conditions.

iii. *Lateral heat flow*: Although the results presented in Figures 4.6a-6e suggest that lateral heat flow is minimal across the mineral soil profiles, it should be noted that P6 and P21, the two boreholes closest to the peat deposit, are situated 80-90 m away (Figure 4.3). On the other hand, C1 and C2 are only separated by 25-40 m from mineral soils. Hence, these cores are more susceptible to lateral gradients in temperature, which could trigger heat flow between the two terrain types. Therefore, future research should consider 2D or 3D thermal models at the peat location.

4.6 CONCLUSION

Depending on the nature of massive ice, as well as the texture and moisture contents of the overlying sediments, simulations show that a wide range of maximum active layer thickness (MALT) projections at Parsons Lake for 2011-2070 are possible. For fine-grained materials characterized by relatively high moisture contents (near saturation) and low thermal diffusivities, MALT growth behaves logarithmically, and increases by as little as 11 cm before stabilizing with time. Fine-grained materials consisting of moderate moisture contents (1/2 saturation) show that the MALT can increase by as much as 76 cm. For situations where the thaw depth penetrates massive ice, subsidence is possible by as early as 2058. Capacitively-coupled resistivity and ground-penetrating radar surveys show that the massive ground ice bodies are extensive, so any one of the aforementioned MALT evolution scenarios is possible in these areas. Furthermore, the geophysical profiles illustrate pockets of icy sediments, some of which consist of gravelly sand deposits. Although only minimal thermokarst is expected in these areas, MALT development could occur at a faster rate. Hence, efficient conduits for the drainage of meltwater generated from adjacent ground ice melt exist, and as a consequence, permafrost degradation may accelerate. The surveys also suggest the possibility of a present day talik beneath the gravel pads, which did not exist during the 2004 CPC fieldwork campaign. Hence, additional fieldwork is recommended to verify the geophysical results.

Chapter 5 - Summary

This research contributed to a better understanding of permafrost conditions at Parsons Lake, and as a result, potential benefits exist for stakeholders interested in natural resource development. In this study, a new approach for the interpretation of geophysical data has been introduced, allowing the nature and extent of ground ice in the Parsons Lake area to be mapped with a greater degree of confidence in the future. Although boreholes are still recommended for subsurface characterization, the quantity of cores needed to constrain geophysical surveys can be reduced from the status quo. Geophysical surveys can provide a first approximation of conditions that can be used to guide aspects of coring programs needed for engineering purposes. This, in turn, will lower operating costs for future research conducted by ConocoPhillips Canada and ExxonMobil. This thesis also provides industry with a thermal model capable of predicting the onset of permafrost degradation at undisturbed locations dominated by low-shrub dominated tundra.

In order to satisfy the thesis's first goal of mapping ground ice distribution, it was necessary to successfully carry out objectives 2 and 3. The second aim of the thesis presented in Chapter 3 was to determine the best balance between data consistency and smoothing in the inversion process by employing depth of investigation (DOI) tests. Provided that correct inversion parameters are used, it was found that the observed resistivity of massive ice ranges from 25 000 to 40 000 Ω. When the DOI tests are not performed, choosing the correct damping factors becomes difficult. For example, if the smoothing factor is too low, the range of resistivity for massive ice can be as widespread as 30 000 - 140 000 Ω. Conversely, if the smoothing factor is too high, the resistivities of massive ice overlap with other materials like entirely frozen ice-rich peat (≈ 9000 Ω). The third objective of the thesis was to combine CCR with GPR and borehole logs for a more accurate evaluation of permafrost properties. Although CCR may generate the same signature for icy deposits of gravelly sand as it does for massive ice, it was found that GPR surveys can map the contact between the two materials. In cases where boreholes do not exist for validation, the use of GPR is valuable for identifying future drilling sites. The use of GPR is also valuable for mapping sediment layers within massive ice, which as studies at the pingo suggest, could reduce resistivity values.

The fourth objective of the thesis presented in Chapter 4 was to develop one-dimensional thermal models capable of predicting the observed temperatures from 2004. It was found that the difference between the observed and predicted values during the thaw season at boreholes characterized by near-surface mineral soils is less than 1 °C at any depth. Since no directional bias concerning the magnitude and sign of the errors was observed, lateral heat flow is minimal at these sites. At the peat deposit, however, the models performed relatively poorly with errors as high as 2-3 °C for C1 and 1-2 °C for C2. Factors potentially affecting the accuracy of model include inaccurate parameterization, lateral heat flows, as well as the local bowl-shaped topography, which could affect snow accumulation, and thus, ground surface temperatures.

Despite the problems with the thermal models at the peat deposit, the predicted temperatures are still able reproduce the observed *cross-over* shown between 5-15 m depths. Throughout this interval, the winter thermal regime is warmer than the summer thermal regime. When the models were run to predict temperatures during the fieldwork campaign in support of objective 5a, the *cross-over* was shown to exist in 2010 as well. Due to electrical resistivity's dependence on unfrozen water content, the *cross-over* could explain why icy sediments composed of black clayey silt at a depths ranging from 5-10 m display a more conductive signature in the winter compared to summer. The study demonstrates that carrying out surveys in more than one season can help scientists identify areas that experience water phase changes. This, in turn, will allow for a better evaluation of the materials present.

Objective 5b of the thesis presented in Chapter 4 was to project maximum active layer thickness (MALT) changes from 2011-2070 by employing climate change scenarios developed for the Mackenzie Valley region. Depending on the nature of massive ice, as well as the texture and moisture contents of the overlying materials, simulations show that a wide range of maximum MALT projections is possible. For silty clays with relatively low volumetric moisture contents (1/2 saturation), the MALT increases linearly with time (0.90 cm/yr from 2011-2040; 1.44 cm/yr from 2040-2070). For silty clays with relatively high moisture contents (near saturation), the MALT increases for a brief period and then stabilizes (0.38 cm/yr from 2011-2040, 1 cm from 2040-2070). For situations where the thaw depth penetrates massive ice, subsidence can begin as early as 2058. Since the thermal models do not account for geomorphic changes, the MALT projections are inaccurate beyond the point at which the active layer propagates into massive ice.

The sixth and final objective of the thesis was to assess the spatial applicability of MALT predictions. CCR and GPR surveys show that the massive ground ice bodies are extensive, so widespread subsidence can develop in approximately 50 years. Furthermore, the surveys illustrate pockets of icy sediments in the near-surface, some of which consist of gravelly sand. MALT development is expected to occur at a faster rate in these areas, and as a result, efficient conduits for the drainage of meltwater generated from adjacent thermokarst exist. This, in turn, could accelerate permafrost degradation. The surveys also illustrate low resistivity anomalies (< 600 Ω) beneath the edge of the gravel pads, which could be representative of taliks or high volumes of unfrozen concentrated on thin bands of sediment in the massive ice. Hence, additional fieldwork is recommended to verify the geophysical results.

Future research at Parsons Lake should consider the addition of a gravimeter for geophysical surveys. Unlike CCR and GPR, which respond to electrical properties, gravimetric profiling (GP) interpret underlying composition based on differences in the densities of subsurface materials. This would facilitate the identification of coarse-grained deposits within permafrost, which as this thesis and other studies suggest, could exhibit the same electrical resistivity as massive ice. Since GP depends on relative changes in gravitational acceleration affected by differential volumetric subsurface densities, it is effective at mapping lateral as opposed to vertical changes in materials. Hence, the application of GPR is the best option to provide a high-resolution image of the gravitational anomaly's location. From a ground thermal regime perspective, all undisturbed boreholes should be modelled to determine which of the MALT projections presented in this thesis is most representative of Parsons Lake. In addition, multidimensional thermal models should be considered for the gravel pad and former drilling sumps, which results suggest, could already be undergoing the first phases of permafrost degradation.

REFERENCES

ACIA. 2004. ACIA, *Impact of a Warming Arctic: Arctic Climate Impact Assessment*, Cambridge University Press (2004), p. 139.

al Hagrey, S.A. and Muller, C. 2000. GPR study of pore water content and salinity in sand. Geophysical Prospecting, 48(1): 63-85.

Andersland, O.B. and Ladanyi, B. 2004. Frozen Ground Engineering, 2nd edition. John Wiley & Sons, New Jersey. 363 p.

Andersland, O.B. and Anderson, D.M. 1978. Geotechnical Engineering for Cold Regions. New York, McGraw Hill, 566 pp.

Anderson, D.M., Tice, A.R., and McKim, H.L. 1973. The unfrozen water and apparent specific heat capacity of frozen soils. *In North Am. Contrib., 2nd Int. Conf. on Permafrost*, Yakustk, USSR.

Annan, A.P., 2005, The Principals of Ground Penetrating Radar, in Near-Surface Geophysics, – Investigations in Geophysics - editor Dwain Butler; Society of Exploration Geophysicists No. 13; Pg. 357-438.

Arcone, S.A. and Delaney, A.J. 2003. Radiowave pulse refraction and ground wave propagation through permafrost and the active layer. In: Proceedings, Eighth International Conference on Permafrost, 2003: 21-26.

Arcone, S.A., Lawson, D.E., Delaney, A.J., Strasser, J.C., and Strasser, J.D. 1998. Ground penetrating radar reflection profiling of groundwater and bedrock in an area of discontinuous permafrost. Geophysics 63: 1573-1584.

Associated Geosciences, 2010. Appendum to Permafrost Geophysics Short Course. 63rd Canadian Geotechnical Conference and 6th Canadian Permafrost Conference, 12-16 September 2010, Calgary, Alberta, Canada.

Bockheim, J.G. and Tarnocai, C. 1998. Nature, occurrence, and origin of dry permafrost. Proceedings of the Seventh International Permafrost Conference. Yellowknife, N.W.T., pp 57-63.

Bogolyubov, A.N. 1973. Investigation of dependence of specific resistance of unconsolidated frozen deposits in original bedding on cryogeneous textures and temperatures. In:

Proceedings, Second International Conference on Permafrost, Yakutsk, USSR Contribution Volume, pp. 482-485.

Brown, R.D.; B. Brasnett and D. Robinson. 2001. Development of a gridded North American daily snow depth and snow water equivalent dataset for GCM validation. *Proceedings, Fifty-eighth Annual Eastern Snow Conference, Ottawa, Canada*, pp. 333–340.

Brown, J., and Grave, N. A., 1979. Physical and thermal disturbance and protection of permafrost. *Special Report* 79-5, Cold Regions Research and Engineering Laboratory, Hanover, N.H., 43 pp.

Brown, R.J.E. 1973. Influence of climatic and terrain factors on ground temperatures at three locations in the permafrost region of Canada. *Proceedings of the Second International Conference on Permafrost, Yakutsk, USSR, North American Contribution*, pp. 27-34. Washington D.C.: Nat. Acad. Sci.

Burn, C.R., Barrow, E., and Bonsal. B. Climate change scenarios of the Mackenzie River Valley. In Proceedings: 57th Canadian Geotechnical Conference, Québec, 7A, vol. 2, pp. 2–8.

Burn, C.R. and Michel, F.A. 1987. Evidence for recent temperature-induced water migration into permafrost from the tritium content of ground ice near Mayo, Yukon Territory, Canada.

Calvert, H.T., Dallimore, S.R., and Hunter, J.A. 2001. Application of geophysical techniques for mapping ice-bearing sediments, Mackenzie Delta, Western Arctic, Canada. Conference on the Geophysical Detection of Subsurface Water on Mars, Abstract 7041.

Claerbout, J.F. and Muir, F. 1973. Robust modelling with erratic data. Geophysics 38: 826-844.

Couture, N.J. and Pollard W.H., 1998. An assessment of ground ice volume near Eureka, Northwest Territories. *Permafrost, Seventh International Conference*, June 23-27, Yellowknife, Canada. A.G. Lewkowicz and M. Allard (eds.). Université Laval, Centre d'études nordiques, Collection Nordicana, 195-200.

deGroot-Hedlin, C. and Constable, S. 1990. Occam's inversion to generate smooth, two-dimensional models from magnetotelluric data. Geophysics 55: 1613-1624.

De Pascale, G.P., Pollard, W.H., and Williams, K.K. 2008. Geophysical mapping of ground ice using a combination of capacitive coupled resistivity and ground-penetrating radar, NWT, Canada. *Journal of Geophysical Research*, 113, F02S90.

Edwards, L.S. 1977. A modified pseudosection for resistivity and induced-polarization. Geophysics 42: 1020-1036.

Ellis, R.G. and Oldenburg, D.W. 1994. Applied geophysical inversion. Geophysical Journal International 116: 5-11.

Environment Canada. National Climate Data and Information Archive. http://climate.weatheroffice.gc.ca/climate_normals/results_e.html?stnID=1669&lang=e&dCode=1&province=NWT&provBut=Search&month1=0&month2=12

Environmental Impact Statement for the Mackenzie Gas Project (EIS). 2004. Volume 3: Biophysical Baseline: Part D, Terrestrial Resources: Soils, Landforms and Permafrost and Vegetation. Published online by the Mackenzie Gas Project. <http://www.mackenziegasproject.com/theProject/regulatoryProcess/applicationSubmission/Applicationscope/EIS.html#threed>

van Everdingen, R. O., 1979. Potential interactions between pipelines and terrain in a northern environment. *NHRI Paper* 8, National Hydrology Research Institute, Inland Waters Directorate, Ottawa, Ontario, 7 pp.

Farouki, O.T. 1981. Thermal properties of soils. *Monograph 81-1*, Cold Regions Research and Engineering Laboratory, Hanover, N.H., 136 pp.

Farquharson, C.G. and Oldenburg, D.W. 1998. Non-linear inversion using general measures of data misfit and model structure. Geophysical Journal International 134: 213-227.

Forbes, B. C., 1996. Plant communities of archaeological sites, abandoned dwellings, and trampled tundra in the eastern Canadian Arctic: A multivariate analysis. *Arctic*, 49, 141-154.

Fortier, R., LeBlanc, A.M., Allard, M., Buteau, S., and Calmels, F. 2008. Internal structure and conditions of permafrost mounds at Umiujaq in Nunavik, Canada, inferred from field investigation and electrical resistivity tomography. Canadian Journal of Earth Sciences 45: 367-387

Fortier, R., Allard, M., and Seguin, M.K. 1994. Effect of physical properties of frozen ground on electrical resistivity logging. Cold Regions Science and Technology 22: 361-384

French, H. M., 1996. *The Periglacial Environment*, Longman, London, 341 pp.

French, H. M., Bennett, L., and Hayley, D. W., 1986. Ground ice conditions near Rea Point and on Sabine Peninsula, eastern Melville Island. *Canadian Journal of Earth Sciences*, 23, 1389-1400.

French, H. M., 1981. Sump studies IV: Permafrost terrain disturbances adjacent to exploratory well sites, northern Yukon Territory. *Environmental Studies* No. 19, Arctic Land Use Research Program, Department of Indian and Northern Affairs, Ottawa, Ontario, 41 pp.

French, H. M., 1975. Man-induced thermokarst, Sachs Harbour airstrip, Banks Island, Northwest Territories. *Canadian Journal of Earth Sciences*, 12, 132-144.

Furgale P T, Barfoot T D, Osinski G R, Williams K, and Ghafoor N. 2010. Field Testing of an Integrated Surface/Subsurface Modeling Technique for Planetary Exploration. International Journal of Robotics Research, special issue on "Field and Service Robotics", 29(12):1529–1549.

Goodrich, L.E. 1982. The influence of snow cover on the ground thermal regime. *Canadian Geotechnical Journal* 19: 421-432.

Harris, S.A., French, H.M., and Heginbottom, J.A. 1988. Glossary of permafrost and related ground-ice terms. Permafrost Subcommittee, National Research Council of Canada.

Harry, D.G. 1988. Ground ice and permafrost. In: Advances in Periglacial Geomorphology. John Wiley & Sons, Great Britain.

Hauck, C. and Kneisel, C. 2006. Application of capacitively-coupled and DC electrical resistivity imaging for mountain permafrost studies. Permafrost and Periglacial Processes, 17: 169-177.

Hauck, C., Vonder Muhll, D., and Maurer, H. 2003. Using DC resistivity tomography to detect and characterize mountain permafrost. Geophysical Prospecting, 51: 273-284.

Hauck, C.H. and Vonder Muhll, D.V. 2003. Inversion and interpretation of two-dimensional geoelectrical measurements for detecting permafrost in mountainous regions. Permafrost and Periglacial Processes 14: 305-318.

Hauck, C.H. 2002. Frozen ground monitoring using DC resistivity tomography. Geophysical Research Letters 29(21), 2016, doi:10.1029/2002GL014995, 2002.

Hauck, C., Isaksen, K., Vonder Muhll, D., and Sollid, D. 2004. Geophysical surveys designed to delineate the altitudinal limit of mountain permafrost: an example from Jotunheimen, Norway. Permafrost and Periglacial Processes, 15: 191-205.

Heginbottom, J. A., 1973. Some effects of surface disturbance on the permafrost active layer at Inuvik, N.W.T. *Environmental-Social Committee Northern Pipelines, Task Force on Northern Oil Development* 73-16, Geological Survey of Canada, 29 pp.

Hilbich, C., Marescot, L., Hauck, C.H., Loke, M.H., and Mausbacher, R. 2009. Applicability of electrical resistivity tomography monitoring to coarse blocky and ice-rich permafrost landforms. Permafrost and Periglacial Processes 20: 269-284.

Hinkel, K.M., Doolittle, J.A., Bockheim, J.G., Nelson, F.E., Paetzold, R., Kimble, J.M., and Travis, R. 2001. Detection of subsurface permafrost features with ground-penetrating radar, Barrow, Alaska. Permafrost and Periglacial Processes, 12: 179-190.

Hoekstra, P, Sellman, P.V., and Delaney, A. 1975. Ground and airborne resistivity surveys of permafrost near Fairbanks, Alaska. Geophysics 40: 641-656.

Hoekstra, P. and McNeill, D. 1973. Electromagnetic probing of permafrost. In: Proceedings, Second International Conference on Permafrost, 1973, Washington, National Academy of Sciences.

Horvath, C.L. 1998. An evaluation of ground penetrating radar for investigations of palsa evolution, MacMillan Pass, NWT, Canada. In: Proceedings, Seventh International Conference on Permafrost, Yellowknife, Canada: 473-478.

Hughes, O.L. 1969. Distribution of open-system pingos in central Yukon Territory with respect to glacial limits. Geological Survey of Canada, Ottawa, Paper 69-34. 8 p.

Johansen, O. 1975. Thermal Conductivity of Soils. Ph.D. thesis. Trondheim, Norway. (CRREL Draft Translation 637, 1977), ADA044002.

Jorgenson, M. T., 1997. Patterns and rates of, and factors affecting natural recovery on land disturbed by oil development in arctic Alaska. In: *Disturbance and Recovery in Arctic Lands*, R. M. M. Crawford, ed., Kluwer Academic Publishers, 421-442.

Kanigan, J.C.M. and Kokelj, S.V. 2010. Review of current research on drilling mud sumps in permafrost terrain, Mackenzie Delta Region, NWT, Canada. In proceedings: 63rd Canadian Geotechnical Conference and 6th Canadian Permafrost Conference, Calgary.

Keller, G. 1987. Rock and mineral properties. Electromagnetic methods in applied geophysics - theory, 1, Nabighian (ed.), Society of Exploration Geophysicists.

Kezdi, A. 1974. Handbook of soil mechanics: soil physics. Elsevier Scientific Publications Ltd., New York, NY. *294* p.

Kiggiak-EBA Consulting Ltd. 2005. ConocoPhillips Canada Winter 2004 Work Programs Geotechnical Assessment Program Parsons D-20 Lease Site, NWT. Report prepared for ConocoPhillips Canada.

Kneisel, C., Hauck, C., Fortier, R., and Moorman, B. 2008. Advances in geophysical methods for permafrost investigations. Permafrost and Periglacial Processes 19: 157-17

Kneisel, C. 2004. New insights into mountain permafrost occurrence and characteristics in glacier forefields at high altitude through the application of 2D resistivity imaging. Permafrost and Periglacial Processes, 15: 221-227.

Konrad, J.M. 1990. Theoretical modelling of massive icy beds. *In* Permafrost - Canada, Proceedings of the Fifth Canadian Permafrost Conference, Quebec City, Quebec: Centre d'études nordiques, 31-35.

Kujala, K., Seppala, M., and Holappa, T. 2008. Physical properties of peat and palsa formation. Cold Regions Science and Technology 52: 408-414

Kurfurst, P. J., 1973. Terrain disturbance susceptibility, Norman Wells area, Mackenzie Valley. *Environmental-Social Committee Northern Pipelines, Task Force on Northern Oil Development* 73-24, Geological Survey of Canada, 36 pp.

Lawson, D. E., 1986. Response of permafrost terrain to disturbance: A synthesis of observations from northern Alaska, U.S.A. *Arctic and Alpine Research*, 18, 1-17.

Lawson, D. E., Brown, J., Everett, K. R., Johnson, A. W., Komarkova, V., Murray, B. M., Murray, D. F., and P.J., W., 1978. Tundra disturbance and recovery following the 1949 exploratory drilling, Fish Creek, Northern Alaska. *Report* 78-28, Cold Regions Research and Engineering Laboratory, Hanover, N.H., 91 pp.

Loke, M.H. 2010. Tutorial: 2D and 3D electrical imaging surveys. www.geoelectrical.com

Loke, M.H. 1999. Tutorial: 2D and 3D electrical imaging surveys. www.geoelectrical.com

Loke, M.H., Acworth, I., and Dahlin, T. 2003. A comparison of smooth and blocky inversion methods in 2D electrical imaging surveys. Exploration Geophysicists 34: 182-187.

Loke, M.H. and Dahlin, T. 2002. A comparison of the Gauss-Newton and quasi-Newton methods in resistivity imaging inversion. Journal of Applied Geophysics 49: 149-162.

Loke, M.H. and Barker, R.D., 1996. Rapid least-squares inversion of apparent resistivity pseudosections by a quasi-Newtonian method. Geophysical Prospecting 44: 131-152.

Lunardini, V. 1981. Heat transfer in cold regions. New York: Van Nostrand Reinhold. 731 pp.

Mackay, J. R., 1995. Active layer changes (1968 to 1993) following the forest-tundra fire near Inuvik, N.W.T., Canada. *Arctic and Alpine Research*, 27, 323-336.

Mackay, J.R. and Dallimore, S.R. 1992. Massive ice of the Tuktoyaktuk area, western Arctic coast, Canada. Canadian Journal of Earth Sciences 29-66: 1235-1249.

Mackay, J.R. 1985. Pingo ice of the western Arctic coast, Canada. Canadian Journal of Earth Sciences, Vol. 22, No. 10,pp.1452-1464.

Mackay, J.R., 1979. Pingos of the Tuktoyaktuk Peninsula, Northwest Territories. Géographic physique et Quaternaire,Vol. 33, No.1, pp. 3-61

Mackay, J.R. 1977. Changes in the active layer from 1968 to 1976 as a result of Inuvik fire. *Geological Survey of Canada*, Paper 77-1B, 273-275.

Mackay, J.R. 1973. The growth of pingos, western arctic coast, Canada. Canadian Journal of Earth Sciences 10-6, pp. 979-1004.

Mackay, J.R. and Black, R.F. 1973. Origin, composition, and structure of perennially frozen ground and ground ice: a review, in *Permafrost: North American Contribution to the Second International Conference*, Yakutsk, USSR, National Academy Press, Washington, DC, pp. 185-92.

Mackay, J.R. 1972. The world of underground ice. *Annals of the Association of American Geographers* 62, pp. 1-22.

Mackay, J.R. 1971. The origin of massive icy beds in permafrost, western arctic coast, Canada. *Canadian Journal of Earth Sciences 84:* 397-422.

Mackay, J. R., 1970. Disturbances to the tundra and forest tundra environment of the western Arctic. *Canadian Geotechnical Journal*, 7, 420-432.

Mackay, J.R. 1966. Pingos in Canada. *Permafrost International Conference, Proceedings.* National Academy of Science - National Research Council, Publication 1287:71-76

Marescot, L., Loke, M.H., Chapellier, D., Delaloye, R., Lambiel, C., and Reynard, E. 2003.

Majorowicz, J. and Grasby, S.E. 2010. Heat flow, depth-temperature variations and stored thermal energy for enhanced geothermal systems in Canada. J. Geophys. Eng. 7: 232-241.

Assessing reliability of 2D resistivity imaging in mountain permafrost studies using the depth of investigation method. Near Surface Geophysics: 57-67.

Maxwell, B. 1997. Responding to Global Climate Change in Canada's Arctic: Volume II of the Canada Country Study: Climate Impacts and Adaptation

McNeill, J.D. 1980. Electrical conductivity of soils and rocks. Geonics Letd., Technical Note TN-5.

Moorman, B.J., Robinson, S.D., and Burgess, M.M. 2003. Imaging periglacial conditions with ground-penetrating radar. Permafrost and Periglacial Processes, 14: 319-329.

Muller, S.W. 1947. Permafrost or permanently frozen ground and related engineering problems. L.J.W. Edwards, Ann Arbor.

Murton, J.B. 2005. Ground-ice stratigraphy and formation at North Head, Tuktoyaktuk Coastlands, Western Canadian Arctic: a product of glacier-permafrost interactions. Permafrost and Periglacial Processes 16: 31-50.

Natural Resources Canada. 1993. Canada-Permafrost [map]. Fifth Edition, National Atlas of Canada.

Nicholson, F.H. and Granberg, H.B. 1973. *Permafrost and snow cover relationships near Schefferville. Proceedings of the Second International Permafrost Conference, Yakutsk, USSR, North American Contribution*, pp. 151-158. Washington D.C.: Nat. Acad. Sci.

Oelke, C., Zhang, T., Serreze, M.C., and Armstrong, R.L. 2003. Regional-scale modelling of soil freeze/thaw over the arctic drainage basin. Journal of Geophysical Research 108 (D10), 4314, doi:10.1029/2002JD002722.

Olhoeft, G.R. 1981. Electrical properties of rocks. Physical properties of rocks and minerals 2 Touloukian and Ho (eds.), McGraw Hill.

Oldenburg, D.W. and Li, Y. 1999. Estimating depth of investigation in dc resistivity and IP surveys. Geophysics 64-2: 403416.

Osterkamp, T.E. and Lachenbruch, A.H. 1990. Thermal regime of permafrost in Alaska and predicted global warming. Journal of Cold Regions Engineering 4-1.

Parkhomenko, E.I. 1967. Electrical properties of rocks, Plenum Press.

Perfect, E. and Groenevelt, P.H. 1990. A model for the clarification of perennial ground ice by thermally-induced regelation. *In* Permafrost - Canada, Proceedings of the Fifth Canadian Permafrost Conference, Quebec City, Quebec: Centre d'études nordiques, 37-42.

Pollard, W.H. and Dallimore, S.R. 1988. Petrographic characteristics of massive ground ice, Yukon Coastal Plain, Canada. In: Proceedings, Fifth International Conference on Permafrost, August 1988, Trondheim, Norway. Tapir Press, Trondheim, Norway: 224-229.

Pollard, W. H., and French, H. M., 1980. A first approximation of the volume of ground ice, Richards Island, Pleistocene Mackenzie Delta, NWT. *Canadian Geotechnical Journal*, 17, 509-516.

Radforth, J. R., 1972. Immediate effects of wheeled vehicle traffic on tundra during the summer. *ALUR* 72-73-12, Arctic Land Use Research Program, Department of Indian and Northern Affairs, Ottawa, Ontario, 32 pp.

Rennie, J.A., Henderson, J., and Reid, D. 1978. Permafrost extent in the southern fringe of the discontinuous permafrost zone, Fort Simpson, N.W.T. In: Proceedings of the Third International Conference on Permafrost, Edmonton, Vol. 1, pp 439-444.

Riseborough, D.W., Shiklomanov, N., Etzelmuller, B., Gruber, S., and Marchenko, S. 2008. Recent advances in permafrost modelling. *Permafrost and Periglacial Processes* 19: 137-156.

Riseborough, D.W. 2007. The effect of transient conditions on an equilibrium permafrost-climate model. Permafrost and Periglacial Processes 18: 21-32. doiL10.1002/ppp.579.

Riseborough, D.W. and Smith, M.W. 1993. Modelling permafrost response to climate change change and climate variability. Proceedings of the Fourth International Symposium on Thermal Engineering and Science for Cold Regions, Hanover, New Hampshire, U.S.A.

Sasaki, Y. 1992. Resolution of resistivity tomography inferred from numerical simulation. Geophysical Prospecting 40: 453-464.

Scott, W., Sellman, P., and Hunter, J. 1990. Geophysics in the study of permafrost, in *Geotechnical and Environmental Geophysics,* S. Ward (Ed.), Society of Exploration Geophysicists, Tulsa: 355-384.

Scott, W.J. and Mackay, J.R. 1977. Reliability of permafrost thickness determination by DC resistivity sounding. National Research Council, Technical Mem. 119, pp 25-38.

Serreze, M.C., Walsh, J.E., Chapin III, F.S., Osterkamp, T., Dyurgerov, M., Romanovsky, V., Oechel, W.C., Morison, J., Zhang, T., and Barry, R.G. 2000. Observational evidence of recent change in the northern high-latitude environment. Climatic Change, 46: 159-207.

Sharma, P.V. 1997. *Environmental and engineering geophysics*. Cambridge University Press, Cambridge, UK: 475pp.

Smith, S.L. and Riseborough, D.W. 2010. Modelling the thermal response of permafrost terrain to right-of-way disturbance and climate warming. Cold Regions Science and Technology 60: 92-103.

Smith, M. and Tice, A. 1988. Measurement of unfrozen water content of soils. *In Proc. 5th Int. Conf. on Permafrost*, Trondheim, Norway, ed. K. Senneset. Trondheim, Norway: Tapir, vol. 1, pp. 473-77.

Smith, M.W. 1985. Observations of soil freezing and frost heave at Inuvik, Northwest Territories, Canada. *Canadian Journal of Earth Sciences* 22-2: 283-90

Smith, M.W. 1975. Microclimatic influences on ground temperatures and permafrost distribution, Mackenzie Delta, Northwest Territories. *Canadian Journal of Earth Sciences* 12: 1421-38.

Stevens, C.W., Moorman, B.J., Solomon, S.M., and Hugenholtz, C.H. 2008. Mapping subsurface conditions within the near-shore zone of an Arctic delta using ground penetrating radar. Cold Regions Science and Technology. doi:10.1016/j.coldregions.2008.09.005

Sushama, L., Laprise, R., Caya, D., Verseghy, D., and Allard, M. 2007. An RCM projection of soil, thermal, and moisture regimes for North American permafrost zones. Geophysical Research Letters 34, L20711, doi: 10.1029.2007GL031385.

Timofeev, V.M., Rodozinski, A.W., Hunter, J.A., and Douma, M., 1994. A new ground resistivity method for engineering and environmental geophysics. Proceedings of the Symposium on the Application of Geophysics to Engineering and Environmental Problems, EEGS: 701-715

Torrance, J.K. and Schellekens, F.J. 2006. Chemical factors in soil freezing and frost heave. Polar Record 42 (220): 33-42

Vondermuhll, D., Hauck, C., and Gubler, H. 2002. Mapping of mountain permafrost using geophysical methods. Progress in Physical Geography 26-4: 643-660.

Walker, D. A., Cate, D., Brown, J., and C., R., 1987. Disturbance and recovery of arctic Alaskan tundra terrain: A review of recent investigations. *Report* 87-11, Cold Regions Research and Engineering Laboratory, Hanover, N.H., 70 pp.

Williams, P.J. and Smith, M.W. 1989. The Frozen Earth: Fundamentals of Geocryology, Cambridge University Press, New York. 306 p.

Yoshikawa, K., Leuschen, C., Ikeda, A., Harada, K., Gogineni, P, Hoekstra, P., Hinzman, L., Sawada, Y., and Matsuoka, N. 2006. Comparison of geophysical investigations for detection of massive ground ice (pingo ice). Journal of Geophysical Research, 111(E06S19), doi: 10.1029/2005JE002573.

Yu, Q.H., Cheng, G.D., and Wang, W.L. 2003. The progress of permafrost investigations with geophysical methods in China. In: Proceedings, Eighth International Conference on Permafrost, 2003: 1271-1276.

Zhang, T., J.A. Heginbottom, R.G. Barry, and J. Brown. 2000. Further statistics on the distribution of permafrost and ground ice in the Northern Hemisphere. Polar Geog. 24(2): 126-131.

Zhang, Y., Chen, W., and Riseborough, D.W. 2008. Transient projections of permafrost distribution in Canada during the 21st century under scenarios of climate change. Global and Planetary Change 60:3-4, pp. 433-456.

Zhang, T., Barry, R.G., Knowles, K., Heginbottom, J.A., and Brown, J. 2008. Statistics and characteristics of permafrost and ground ice distribution in the northern hemisphere. Polar Geography 31:1-2, pp. 47-68.